Filipe André Boiça Costa

Master of Science in Biomedical Engineering

Dissociative processes induced by electron impact with biologically relevant molecules

Thesis submitted in partial fulfilment of the

requirements for the degree of

Doctor of Philosophy in

Radiation Biology and Biophysics

Applied Atomic and Molecular Physics

Supervisor: Prof. Gustavo García Gómez-Tejedor, Full Professor
Consejo Superior de Investigaciones Científicas
Co-supervisor: Prof. Paulo Limão-Vieira, Full Professor
Universidade Nova de Lisboa

Examination Committee:
Chairperson: Prof. Orlando Manuel Neves Duarte Teodoro
Rapporteurs: Dr. Martina Christina Fuss
Prof. Márcio Henrique Franco Bettega
Members: Prof. Gustavo García Gómez-Tejedor
Prof. Pedro António de Brito Tavares

FACULDADE DE CIÊNCIAS E TECNOLOGIA
UNIVERSIDADE NOVA DE LISBOA

November, 2020

Dissociative processes induced by electron impact with biologically relevant molecules

"Tell me and I forget. Teach me and I remember. Involve me and I learn."

Benjamin Franklin

Acknowledgments

This work was supported by Radiation Biology and Biophysics Doctoral Training Programme (RaBBiT, PD/00193/2012); UIDB/04378/2020 (UCIBIO); CEFITEC (UIDB/00068/2020).

I am very thankful for the opportunity I had to do the PhD. I grew up so much during these 4 years, it is hard to put it into words. There are so many things I would like to say, and people to talk about, I just hope I do not forget something or someone important.

I started the PhD in Faculdade de Ciências e Tecnologias (FCT) of Universidade Nova de Lisboa (UNL). Then, I moved to Instituto de Fisica Fundamental of Consejo Superior de Investigaciones Cientifícas (CSIC) in Madrid. I even spent a short period at Max-Planck-Institut für Kernphysik (MPIK) in Heidelberg. All the institutions and personnel treated me very well, specially CSIC where I spent so much time, so I am very grateful to them.

Regarding the people I want to be thankful for, firstly, I would like to mention my parents. I owe them everything. They always allowed me to follow what I wanted, and gave me their support even when I failed, so I cannot be thankful enough to them. I always try to be as close to them as possible, as they do the same with me.

After them, I want to show my gratitude to Prof. Dr. Gustavo García. He gave me the opportunity to be part of his research group and to perform my work in his lab. He gave me the opportunity to visit other international groups and attend scientific meetings. He taught me so many good values and small things that go beyond the scientific world. We had so many conversations at lunch time about so many subjects. I will never forget him, and he will always have my upmost respect.

Then, I would like to thank Prof. Dr. Paulo Limão-Vieira, Prof. Dr. Pedro Tavares and Prof. Dra. Alice Pereira because they are the people who oversee the RaBBiT PhD Program and allowed me to enter this course. My special thanks go to Prof. Dr. Paulo Limão-Vieira because he was the person I got more in contact with, as he always answered me and tried to help. I want to acknowledge Prof. F. Blanco, Prof. M. Bettega and Prof. J. Gorfinkiel for providing their theoretical data in order to complement the cross section data bases used in this study for the electron transport simulations. I also want to mention Prof. Dr. Alexander Dorn, that embraced me in his laboratory at the Max-Planck-Institut für Kernphysik (MPIK) in Heidelberg, where we obtained important new measurements.

When I left Portugal and arrived in Spain, I went to find a group of colleagues in CSIC that will always play a part in my life. It started with Lilian Ellis-Gibbings, Ali Traoré, Alexey Verkhovtsev, Ana Lozano, Mónica Mendes and me, and then some left and Carlos Guerra and Lidia Álvarez entered. I feel I created a special bond with Ana, Mónica, Lidia and Carlos, because I spent a lot of time with them, and they always helped me with everything. I learned so much Spanish with them and they taught me so many good things. I still talk with Ana in a daily basis for example.

During my time in Spain, I had to find some activities besides the PhD, so I entered an Ultimate Frisbee team. There I met some of the most important people in my life, people I can always count on for everything. Without them, everything would be much more difficult. Their friendship and the good moments we spent together made my time in Madrid feel like home. Antonio David, Carme, Begoña, Juan, Yero and Monish, you are the best friends I have made in Madrid, I am always here for you too.

I also wanted to dedicate some words to my friends Micael, Leonardo, Ricardo, Gilberto, Fernando, Iolanda, Daniel and Diogo. You have been in my life for some years, but it feels like an eternity. We have shared some important and memorable moments, and your kindness, friendship and support always helped and guided me.

Finally, I want to thank Joana for her patience, for believing in me and for being always there for me no matter what. I know I am stubborn and a little bit crazy sometimes, but you always knew how to handle me. You are very important to me and I hope I can help you when you need.

Abstract

The work presented in this thesis is based on the study of electron collisions with molecules of biological interest. The primary focus is to perform electron scattering measurements with a linear transmission beam system that has been improved and tested to obtain accurate results. Along with this experimental system, other electron scattering measurements with different apparatuses are presented. Theoretical values obtained with three different calculation methods are also presented for some of the studied molecules. The scattering targets that have been the subject of this work were benzene, nitrobenzene and pyridine for different impact energy ranges. Note that, the two latter are representative case studies due to their dipole moment. The different experimental systems used in this study are described but, the linear transmission beam system receives particular emphasis, followed by the magnetic confinement electron beam apparatus and the reaction microscope. All the data obtained is then critically analysed and compared with other relevant results and they are finally, compiled to provide a complete reference data set to describe the electron scattering cross sections from the respective molecules, for the corresponding energy ranges. The results are carefully selected to obtain self-consistent electron collisional data bases which are recommended for some of the mentioned molecules in order to be used for modelling purposes. The influence of the dipole moment in the dynamics of electron interaction with molecules is also analysed, in particular for those biologically relevant. A modelling electron transport simulation for the molecule of pyridine in the energy range of 0-100 eV is also presented. Finally, some conclusions and considerations regarding the obtained data and the agreement with other existent data are summarised.

Keywords: electron collisions; electron scattering cross sections; electron transport in gases; molecular ionization.

Resumo

O trabalho apresentado nesta tese baseia-se num estudo de colisões de electrões com moléculas de interesse biológico. O objectivo pincipal é realizar medidas de dispersão de electrões com um sistema linear de transmissão de electrões que foi melhorado e testado de maneira a obter resultados fiáveis. Juntamente com este sistema experimental, outras medidas com diferentes sistemas experimentais e valores calculados são apresentados. Valores teóricos obtidos com três métodos de cálculo diferentes são também apresentados para algumas das moléculas estudadas. As moléculas de estudo focadas neste trabalho foram benzeno, nitrobenzeno e piridina para diferentes intervalos de energia. De notar que as duas últimas representam importantes casos de estudo devido aos seus momentos dipolares. Os diferentes sistemas experimentais usados para este estudo são descritos neste trabalho, mas o sistema linear de transmissão recebe maior ênfase, seguido do sistema de confinamento magnético de electrões e do microscópio de reacção. Todos os dados obtidos são então analisados de uma forma crítica e comparados com outros resultados relevantes, e são compilados de forma a dar uma referência completa capaz de descrever secções eficazes de dispersão de electrões para as respectivas moléculas e para os correspondentes intervalos de energia. Os resultados são cuidadosamente escolhidos para obter conjuntos de dados sobre colisões de electrões que podem ser recomendados para algumas das moléculas mencionadas, e ao mesmo tempo, podem ser também usados em modelos. A verificação da influência do momento dipolar na dinâmica da interacção de electrões com moléculas é também analisada, em particular nas moléculas de interesse biológico. Um modelo simulado de transporte de electrões para a molécula de piridina no intervalo de energia de 0-100 eV é também apresentado. Por fim, são apresentadas algumas conclusões e considerações em relação aos dados obtidos e à concordância com outros dados existentes.

Palavras-chave: colisões de electrões; secções eficazes de dispersão de electrões; transporte de electrões em gases; ionização molecular.

Contents

List of Figures

List of Tables

Acronyms and Symbols

AD	Analyser Detector
AR	Additivity Rule
CSIC	Consejo Superior de Investigaciones Científicas
DCS	Differential Cross Section
DDCS	Double Differential Cross Section
DEA	Dissociative Electron Attachment
DNA	Deoxyribonucleic Acid
EG	Electron Gun
EELS	Electron Energy Loss Spectrum
FWHM	Full Width at Half Maximum
GT	Gas Trap
HES	Hemispherical Electrostatic Spectrometer
HV	High Voltage
IAM	Independent Atom Model
IAM-SCAR+I	Independent Atom Model with Screening Additivity Rule plus Interference
IC	Interference Chamber
ICS	Integral Cross Section
IECS	Integral Elastic Cross Section
LEE	Low Energy Electron
LEPTS	Low Energy Particle Track Simulation
LTB	Linear Transmission Beam
LUMO	Lowest Unoccupied Molecular Orbital
MCEB	Magnetic Confinement Electron Beam
MCP	Multichannel Plate
MSCOP	Modified Spherical Complex Optical Potential
RNA	Ribonucleic Acid
RPA	Retarding Potential Analyser
SC	Scattering Chamber
SCOP	Spherical Complex Optical Potential
SMC	Schwinger Multichannel
TCS	Total Cross Section
TDCS	Triple Differential Cross Section
TICS	Total Ionization Cross Section
$\mathbf{V_0}$	Incident Energy

Chapter 1. Introduction

In the last few years, relevant studies have shown that for each MeV of ionising radiation thousands of secondary electrons are produced during collisions. Consequently, they interact with other molecules, creating tertiary electrons and so on. The overall result is a radiation cascade in which most of the secondary, tertiary, and further electrons end up having energies below 30 eV. When interacting with biological tissue, these electrons are the main source of energy deposition and radiation damage. These low energy electrons (LEE) play an important role in inducing damage along their track, as they represent one of the main causes of the indirect effect of radiation in the biological components [1][2][3][4]. Therefore, it is important that the different electron interaction parameters cover a wide energy range when studying their interaction with biologically relevant molecules Among these parameters are integral, differential and total cross sections, and energy loss spectra, which describe the different processes that occur when the primary beam interacts with the molecules. Figure 1.1 shows the simulation of single electron tracks in liquid water for electrons with incident energy of 10 keV, which are slowed down by successive interactions with matter. The total cross section (TCS) represents one of the most important parameters to obtain a consistent set of cross section data for modelling purposes. These models are based in event-by-event Monte Carlo simulation programs and need information over a broad energy range, which goes from the high incident energy of primary particles down to their final thermalisation in the medium. As input parameters, they use the cross sections associated with all the possible scattering processes that may occur in the considered energy range. These input parameters constitute a comprehensive and consistent data set, which requires more studies against molecular prototypes. Ultimately, these models will be able to describe the effect of radiation in terms of energy deposition and dissociative processes [5].

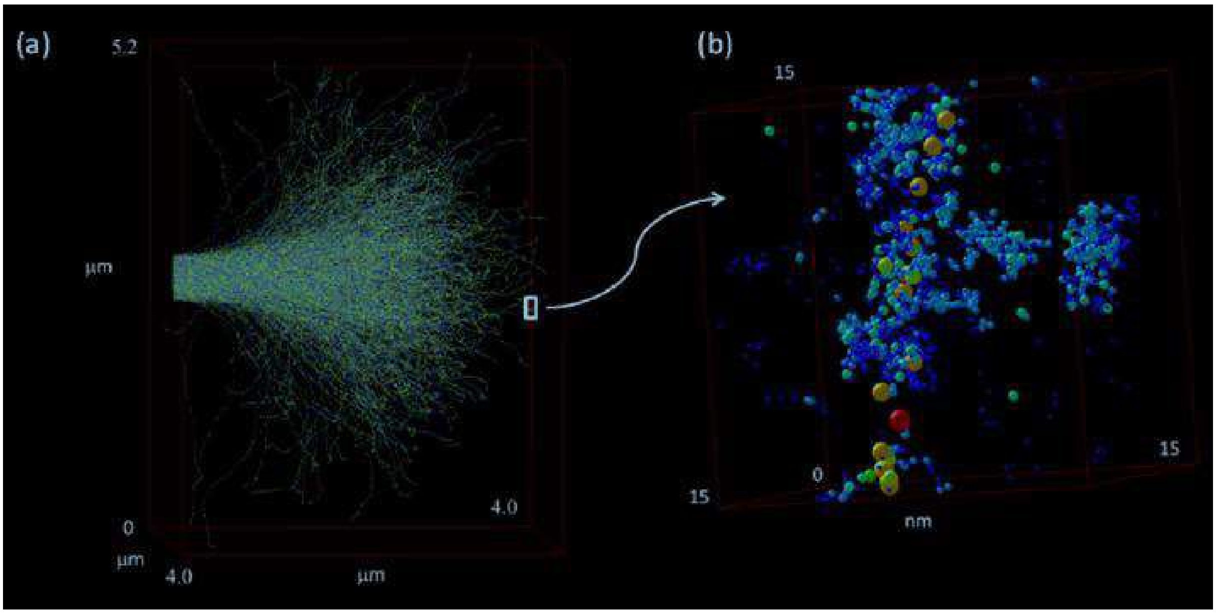

Figure 1.1. Single electron tracks simulation in liquid water. Electrons with 10 keV incident energies are slowed down by successive interactions with matter (e.g. elastic scattering ●, rotational excitation ●, vibrational excitation ●, electronic excitation ●, neutral dissociation ●, ionisation ●, and electron attachment ●). Taken from reference [6].

Studies also show that one third of the damage provoked by LEE in the genome is caused by direct effects, while two thirds are due to indirect effects. As a result, investigating the indirect mechanisms by LEE is essential for a comprehensive knowledge of the damage produced at the molecular level [7]. The need for accurate and complete electron interaction data applies not only to DNA and RNA molecules, but to different molecular constituents of biological tissues, including water, nucleotides, amino acids or entire peptides, fatty acid chains, carbohydrates, among others. The amount of information that electron interactions have with all the molecular species mentioned above is very demanding, which possibly requires a progressive approach to compile all the information. This type of approach should occur not only because of the extent of molecules with biological interest, but also because many potentially interesting biomolecules are especially demanding both for experimentalists and theorists due to their size and/or properties. Some molecules still might not be accessible for studies with current state-of-the-art methods, which is why simpler and reference molecules may be used first as an approximation.

The work presented in this thesis is centred in three different molecules; benzene, nitrobenzene and pyridine. All of these molecules are organic aromatic compounds that are part of and/or serve as precursors to biomolecules. Their structure influences how they react, for instance during polymerization or even decomposition. It is also embedded in the structure of the molecules the information that determines the role of the biomolecules in living systems. Benzene, commonly regarded as the prototype ring molecule, has been already profoundly investigated in terms of TCS.

Despite the fundamental and applied interest in the molecule of nitrobenzene, not many studies have measured or calculated its electron scattering cross sections over a wide energy range. Both benzene and nitrobenzene have similar structures, but nitrobenzene has a functional group (NO_2) that gives the molecule a high dipole moment. This property strongly affects the scattering dynamics, and for this reason, it is important to have benchmarking data for both of these prototype molecules, and establish a comprehensive comparison between them. Our group has also paid considerable attention to the study of electron interactions with pyridine (see Refs. [8][9][10] and references therein). Pyridine is an azaarene, it is considered a derivative of benzene and a prototypical molecule for DNA bases, and consequently electron scattering data concerning this molecule are relevant for modelling electron damage in biomolecular systems [11]. Most of these modelling procedures [11] are based on Monte Carlo codes, which require accurate and full [12] electron scattering cross sections in order to simulate single electron tracks into biological media. As already mentioned, low energy secondary electrons [13] play an important role in creating modelling procedures. For charged particle primary beams (electrons, positrons or ions) these secondary electrons are abundantly generated with energies below 100 eV, and therefore electron scattering cross section data in the energy range of 0-100 eV are specially needed in these types of simulations.

Considering the aforementioned introduction, the aim of this work is to contribute information about electron molecule scattering data about three important molecular species, benzene, nitrobenzene and pyridine, which are directly related with biologically relevant molecules. To achieve this, there was a preparation and configuration of a previous experimental apparatus which can be used for conducting scattering cross section measurements, followed by data acquisition and calculations. At the end, all the data compiled is analysed and compared to other previously available data, regarding the compatibility and completeness. The final objective is to have a complete set of data that can be considered as a benchmark, and at the same time, be used for modelling purposes. All the work presented is based on recent publications from our group. The molecule of benzene can be found in “Experimental and theoretical analysis for total electron scattering cross sections of benzene” [5], where all the literature plus the data produced from our group related with the scattering dynamics of the molecule of benzene is presented. The molecule of nitrobenzene is in “Electron scattering cross sections from nitrobenzene in the energy range 0.4-1000 eV: the role of dipole interactions in measurements and calculations” [14], where all the data produced from our group related with the scattering dynamics of the molecule of nitrobenzene is compiled. As for pyridine, it is studied in “A complete cross section data set for electron scattering by pyridine: modelling electron transport in the energy range 0-100 eV” [15], where electron scattering cross sections for pyridine are critically compiled and complemented with new measurements of electron energy loss spectra and double differential ionization cross sections.

The first chapter of this thesis gives a detailed description of three different experimental apparatuses and the theoretical methods used in the measurements conducted in this work, with particular focus on the linear transfer beam experiment, whose configuration and operation is among the main objectives of the present thesis. Afterwards, in the second chapter, the corresponding experimental and theoretical results are presented and discussed. This includes electron energy loss spectra and total electron scattering cross sections of benzene, nitrobenzene and pyridine. This chapter also presents integral cross sections, double and triple differential cross sections, angular distributions and energy distributions. Chapter three summarizes and discusses the role of the dipole moment in the scattering dynamics and offers a comparison between the molecules of benzene and nitrobenzene. In this chapter, there is also a simulation with the molecule of pyridine for incident energies of 15 eV and 90 eV. In the fourth and final chapter, conclusions are drawn from the present work, as well as perspectives for future approaches.

Chapter 2. Experimental setup

The focus of this chapter is the description and characterization of three experimental systems used to perform the experiments throughout the course of this work. The first section is dedicated to a remodelled linear transmission beam system used for measuring electron energy loss distributions and electron scattering cross section measurements. A comprehensive and detailed description about all the main components for collisions between electrons and different molecular targets can be found. The second section has a brief description of a magnetic confinement electron beam system used for electron scattering cross section measurements at low energies, within a strong magnetic field. Both subchapters are related to the work performed in Laboratorio de Interaccion Radiación-Materia, CSIC, Madrid under supervision of Prof. Gustavo García. It is important to highlight that most of the elements from the experiments were designed and assembled in the laboratory to suit the experimental purposes. Following the previous two, there is a section with a reaction microscope capable of detecting triple coincidence events, used to measure double and triple differential cross sections. This subchapter is related to the work performed in Max Planck Institute for Nuclear Physics (MPIK) in Heidelberg, Germany, under supervision of Prof. Alexander Dorn. In addition to the experiments, three different theoretical methods are briefly described, as they represent an important tool to complement the obtained data and the simulations. The three calculation methods mentioned are the independent atom model with the screening-corrected additivity rule plus interference (IAM-SCAR+I), the Schwinger Multichannel (SMC) method implemented with pseudopotentials and the R-matrix procedure.

2.1. Linear transmission beam (LTB) experiment

This experiment was performed at the Radiation-Matter Interaction Laboratory at Instituto de Fisica Fundamental in CSIC in Madrid. Most of the work presented in this thesis was performed with this experimental system, which includes the measurements of total electron scattering cross section for high energies and electron energy loss studies. This section is dedicated to a general overview of the apparatus, alongside with a description of the different components and specifics of the experiment, the resolution in energy and the experimental uncertainties.

2.1.1. General overview

The system is based on a transmission beam experiment described elsewhere by Traore Dubuis et al [1,2]. Some modifications were made to adapt the system to the requirements of the present measurements. The system has an electron spectrometer that reduces the energy uncertainty and allows to study the scattering dynamics of electrons. In Figure 2.1, a schematic diagram of the experimental system is represented. The apparatus consists of four main regions: an electron gun (EG), the scattering chamber (SC), a hemispherical analyser, and finally, an electron detection region. The whole system is shielded by mu-metal, a nickel-iron magnetic alloy with very high permeability, to reduce the effects of the external magnetic fields. The emerging beam has an approximate uncertainty of 600 meV and it is accelerated and focused into the scattering chamber by collimators and deflecting plates. After the electrons leave the scattering chamber, they enter a lens tube, where they are again focused into a hemispherical analyser. The analyser has a pass energy that is controlled by the user, and the electrons are detected in a two-stage microchannel plate (MCP) operating in single counting mode. The analyser counting and data analysis are controlled in a remote way using a home-made LabView program (National Instrument) together with a computer. Among all the aspects surrounding this experiment, the angular acceptance of the hemispherical spectrometer is one of the most relevant features.

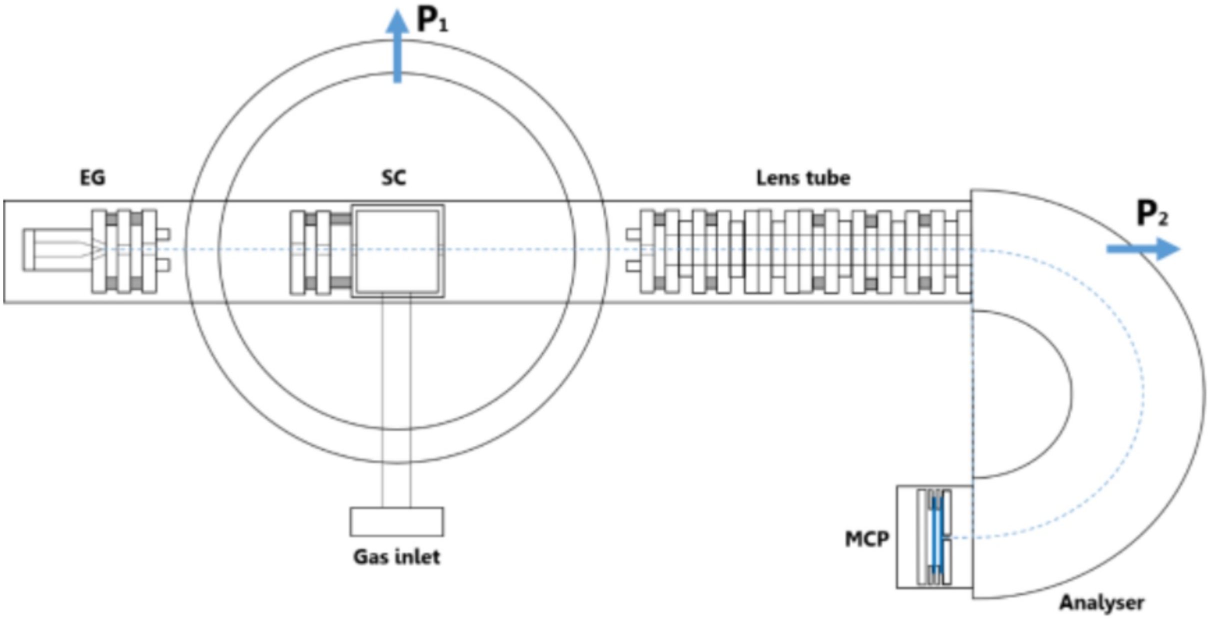

Figure 2.1. Diagram and current configuration of the linear transmission-beam system. EG corresponds to the electron gun, SC to the scattering chamber and the gas inlet to the valve system. The lens tube is composed of several lenses that guide the beam toward the hemispherical analyser. P_1 and P_2 correspond to two different turbo pumps and the MCP (micro channel plates) is where the transmitted electrons are ultimately detected.

2.1.2. Electron gun

The electron gun region can be divided in four major sections: the filament, the extractor, the focus and the deflecting plates. The extractor has a conical central aperture, through which the filament tip enters. The focus, together with the deflecting plates, align the beam as it leaves the extractor. All these elements have a central aperture of 2 mm in diameter. All sections from the electron gun are separated by "Macor®" insulators.

The electron beam is generated by a negatively biased hairpin tungsten filament, which is connected to two power supplies. One of the power supplies (Isotech IPS1810, UK) is connected to both ends of the filament, which will cause the filament to heat, and through thermionic emission, the heat created induces the release of electrons from the tip of the filament. The other power supply (Bertan 205B, USA) is connected to the negative terminal of the filament through the negative HV output, and it will act as the accelerating unit, accelerating the ejected electrons from the filament. The extractor is electrically biased in the same circuit as the filament, being connected to the positive terminal of the power supply. This allows a smooth electron extraction, with a potential difference of approximately 2 V above the voltage applied to the filament by the accelerating power supply unit. The deflecting plates X1 and Y1 each have a variable power supply that goes from -150 to +150 V. After being carefully checked and tested, the focus was kept physically grounded for the measurements made. As a result, an electron beam of 2 mm in diameter is generated with typical beam currents in the range of μA and an average energy spread of about 600 meV. A schematic diagram of the electron gun and the electrical connections is shown in Figure 2.2.

The previous and initial configuration of the system had the electron gun positioned before the first analyser. With this configuration, the experiment was working with two hemispherical analysers, each of them capable of reducing the overall intensity of the beam by a factor of 100. The current of electrons obtained with this configuration in the collision chamber region was too low, so the overall configuration of the system needed some improvements. The first approach was to remove the first hemispherical analyser (monochromator), with the aim of increasing the current of electrons reaching the SC, and consequently the MCP.

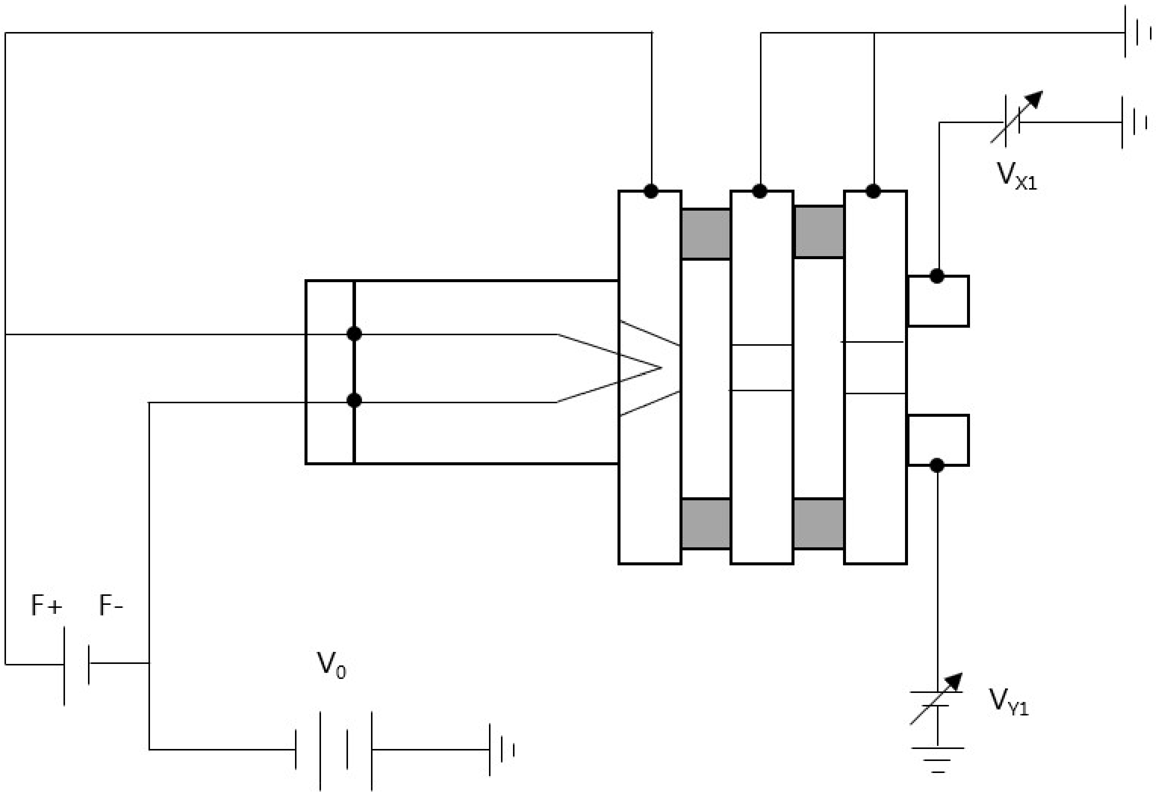

Figure 2.2. Schematic diagram of the electron gun. F+ and F- correspond to the positive and negative terminals of the filament respectively, V_0 is the accelerating potential and V_{X1} and V_{Y1} are the potentials of the deflecting plates. As can be seen in the scheme, the remaining elements of the electron gun are all grounded.

Following the removal of the monochromator, the electron gun was brought to the entrance of the SC, which provided the improvements needed but also presented some limitations. On one hand, the whole structure of the electron gun was bending the position of the SC. When this occurred, the trajectory and the intensity of the electrons was severely affected, as they could not find the entrance into the analyser. On another hand, the gas pressure inside the SC was affecting the emission of the filament. Occasionally, the filament needed more current to stabilize, or in some cases, the trajectory of the beam at the entrance of the SC was affected by some clothing effect. In the case of molecules with a high level of stickiness, these later effects got increased.

After taking into consideration all these challenges, the solution found was to change the position of the electron gun. This new location had to be close enough to the SC to lose as less current as possible, and at the same time, far enough so that it would not suffer any secondary effects from the gas. The solution found was to assemble the electron gun at the top of a flange, which would prevent the previous problems, and at the same time it would help with the alignment. Another small change made in the electron gun region was to remove the repeller and to place the focus after the extractor. This focus has the possibility to be connected to any external power supply, but as already mentioned before, it was always connected to ground. Finally, some deflecting plates were added to the electron gun region, to guide the beam more accurately into the SC.

2.1.3. Scattering chamber

The scattering chamber (SC) is a 50x50x50 mm^3 duralumin cube. The entrance and exit apertures have a 2 mm diameter, as they are distanced by 5 cm (L). At the entrance of the SC, two 1.5 mm collimators ensure that the electron beam diameter at this entrance is less than the collimator diameter so preventing possible gas focusing effects. The SC is perpendicularly held to the gas inlet flange through a 32 mm diameter polytetrafluoroethylene (PTFE) tube connected to an MKS-Baratron (627B) absolute capacitance manometer, maintaining a steady gas flow during the measurements. The SC suffered slight changes, as it was added both collimators to the entrance to act as focus. In Figure 2.3, a diagram of the scattering chamber can be observed. With this configuration, the SC is not grounded; rather, it is connected to a biasing ±1000 V power supply (V_{SC}), which allows to control the collision energy without changing the initial energy that comes from the electron gun. The kinetic energy (E) inside the SC, which corresponds to the impact energy, is then defined by $E = V_{SC} - V_0$.

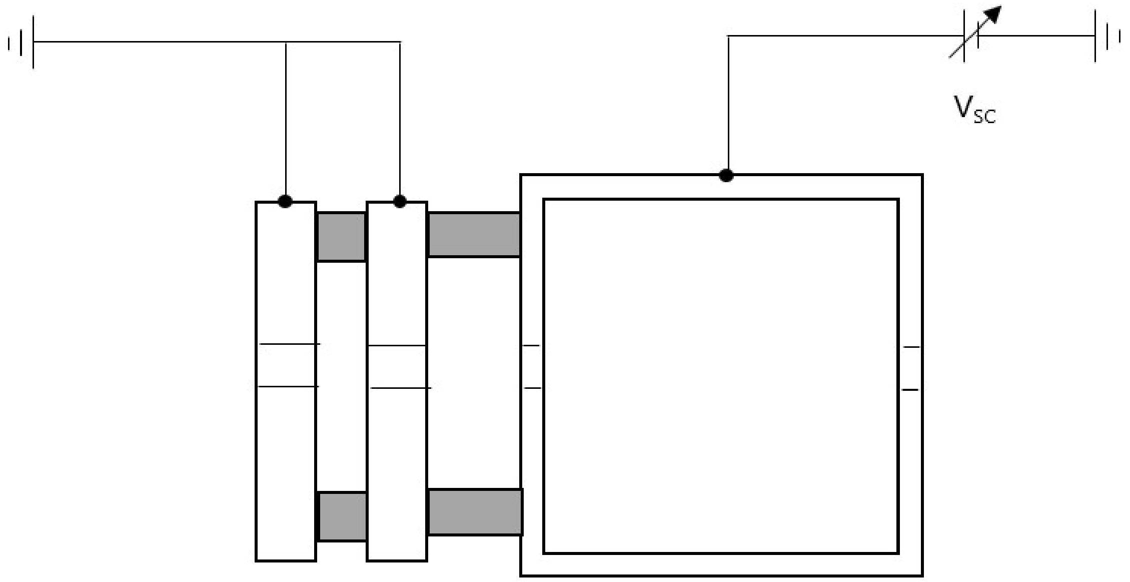

Figure 2.3. Schematic diagram of the scattering chamber. Both collimators at the entrance of the scattering chamber are grounded, and the scattering chamber is connected to an external power supply, that can accelerate the incoming electrons.

2.1.4. Lens tube

At the entrance of the analyser there is a focusing system, formed by a lens tube, used to guide the transmitted beam into the analyser region. A pair of deflecting plates X2 and Y2, each controlled by a variable power supply that goes from -150 to +150 V, is situated at the entrance of the lens tube. The rest of the structure was connected to ground since there was no need to apply an additional voltage in that area to focus the beam. In Figure 2.4, there is a schematic diagram of the lens tube.

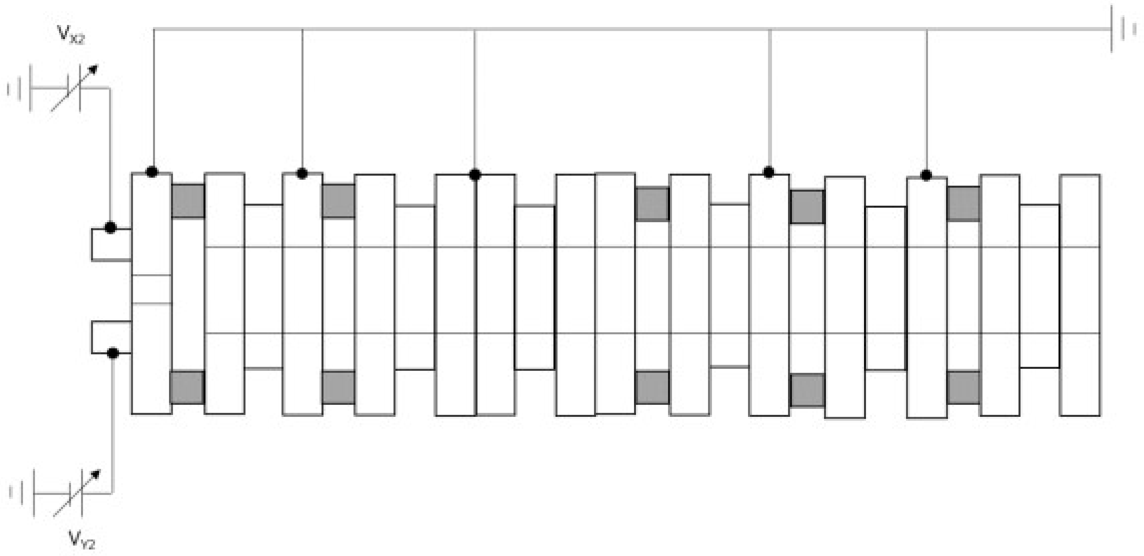

Figure 2.4. Schematic diagram of the lens tube. V_{X2} and V_{Y2} correspond to the deflecting plates at the entrance of the lens tube, positioned right after the scattering chamber. They are connected to a variable power supply, as the remaining elements of the lens tube are all connected to ground.

2.1.5. Analyser

To analyse the electrons as function of their energy, the system has a hemispherical electrostatic spectrometer (HES) equipped with an MCP. This analyser has an electrical shielding, already mentioned above, that prevents most of the effects from external fields. In Figure 2.5, a schematic diagram of the hemispherical analyser can be oberserved.

The HES consists of two concentric duralumin hemispheres, with a mean radius of 10 cm, frequently referred as inner (interior) and outer (exterior) hemispheres. The inner hemisphere is biased positively with respect to the outer hemisphere, so that electrons entering the analyser are forced to follow a circular path by an electrostatic field. Regarding the dependence between the electron’s energy passing through the monochromator with the electrostatic potential applied across the hemispheres, the following theoretical formula was used:

$$E = \Delta V / \left(\frac{R_0}{R_i} - \frac{R_i}{R_0}\right) \qquad (1)$$

where R_i and R_o are the radius of the inner and outer hemispheres, respectively, and ΔV is the difference in voltage applied to the inner and outer hemispheres. In this experiment, R_o = 128 mm and R_i = 72 mm. Using the radius of the hemispheres in the formula mentioned previously, E can be defined as $E = 1.2\Delta V$. Therefore, this spectrometer is characterized by a geometrical factor $k = 1.2$.

In order to scan the energy range of interest, the hemispheres are connected to a negative (retarding) high-voltage supply (Bertan series 362, USA) through four 12 V batteries which maintain a potential difference between the outer and inner hemispheres.

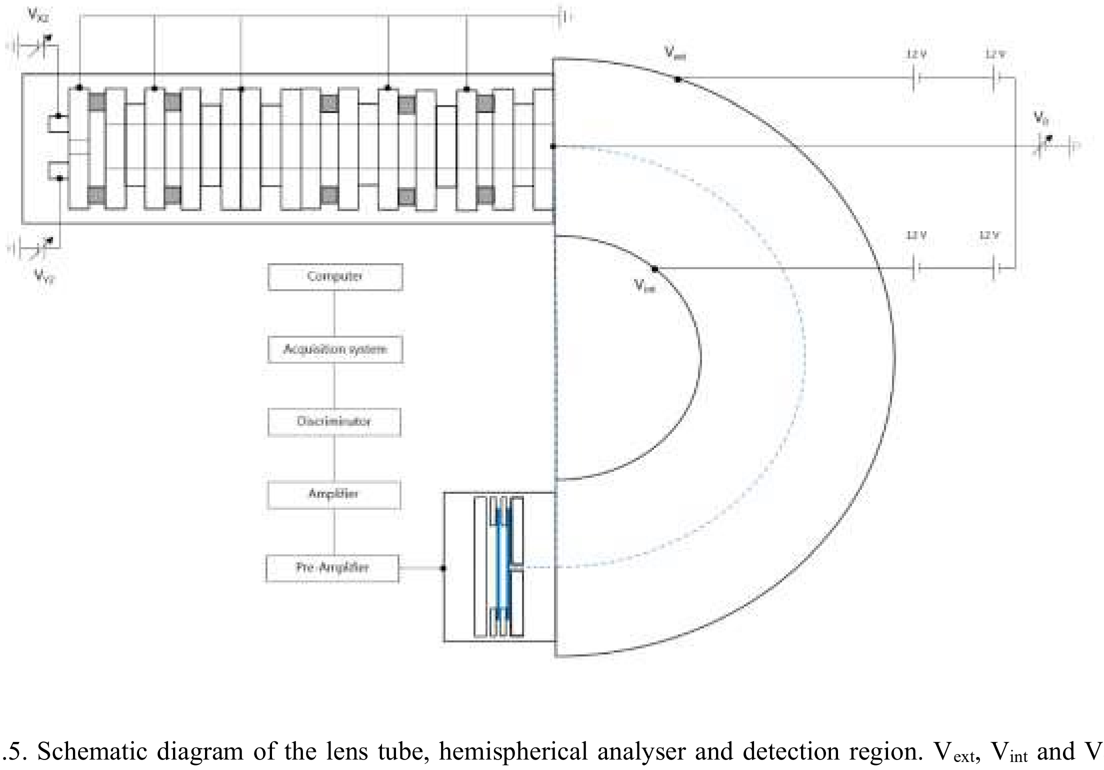

Figure 2.5. Schematic diagram of the lens tube, hemispherical analyser and detection region. V_{ext}, V_{int} and V_0 correspond to the potential applied at the outer hemisphere, at the inner hemisphere and at the medium hemisphere, respectively. After the electrons leave the lens tube, they enter a circular trajectory until they reach the MCP, and afterwards the electronics.

2.1.6. Detector

The electrons are detected by means of an MCP operating in single-pulse counting mode, with a biasing voltage of approximately 2 keV (Bertan series 230, USA). The electron current is collected by a custom-built preamplifier which provides positive voltage pulses (of the order of around 50 mV). These pulses are transferred to an amplifier (model 2020, Canberra, USA) and subsequently to a discriminator (constant fraction discriminator 584, Ortec, USA) which eliminates most of the electronic noise. The eventual resulting pulses are rectangular signals of 5 V amplitude which are collected by a data acquisition system connected to a PC, where a customized LabView software programme counts and stores them for subsequent analysis. In Figure 2.5, all the electronics related with the detection are included, as they are connected to the analyser.

2.1.7. Pumping system

The system is differentially pumped by two turbomolecular pumps, one for the analyser (Varian 210 l/s) and another for the collision chamber (AGILENT 510 l/s). This configuration allows the system to reach a pressure with an order of magnitude of 10^{-8} Torr. At the same time, it also keeps the pressure on the analyser region below 10^{-7} Torr during the measurements without interfering with the pressure values used in scattering chamber, which can be around 10 mTorr. The primary vacuum conditions of the two regions are provided by two two-stage rotary pumps with pumping speeds of 1.8 l/s, and 0.92 l/s.

2.1.8. Energy and angular resolution

Alongside with the many features provided by this system, the angular acceptance of the hemispherical analyser of the transmitted electrons is very important to mention. At the entrance of the spectrometer, there is a 1.5 mm aperture distanced 40 cm from the centre of the SC. According with these values, the value obtained for the solid angle is in order of magnitude of 10^{-5} sr, which leads to a practical acceptance angle of around 0.25°. The best resolution can be found by looking at the full width at half-maximum (FWHM) at the elastic peak, which has an average value of approximately 600 meV. The resolution may differ from this value because it depends not only on the optimization of the filament, but also on the incident energy and target used. In Figure 2.6, it is possible to visualize the resolution of the measurements taken for nitrobenzene for electrons with 200 eV of incident energy. Typically, spectra were recorded up to an energy loss of about 100 eV for all incident energies, i.e. the spectra contain information from electrons that lost from 0 until 100 eV of their initial energy.

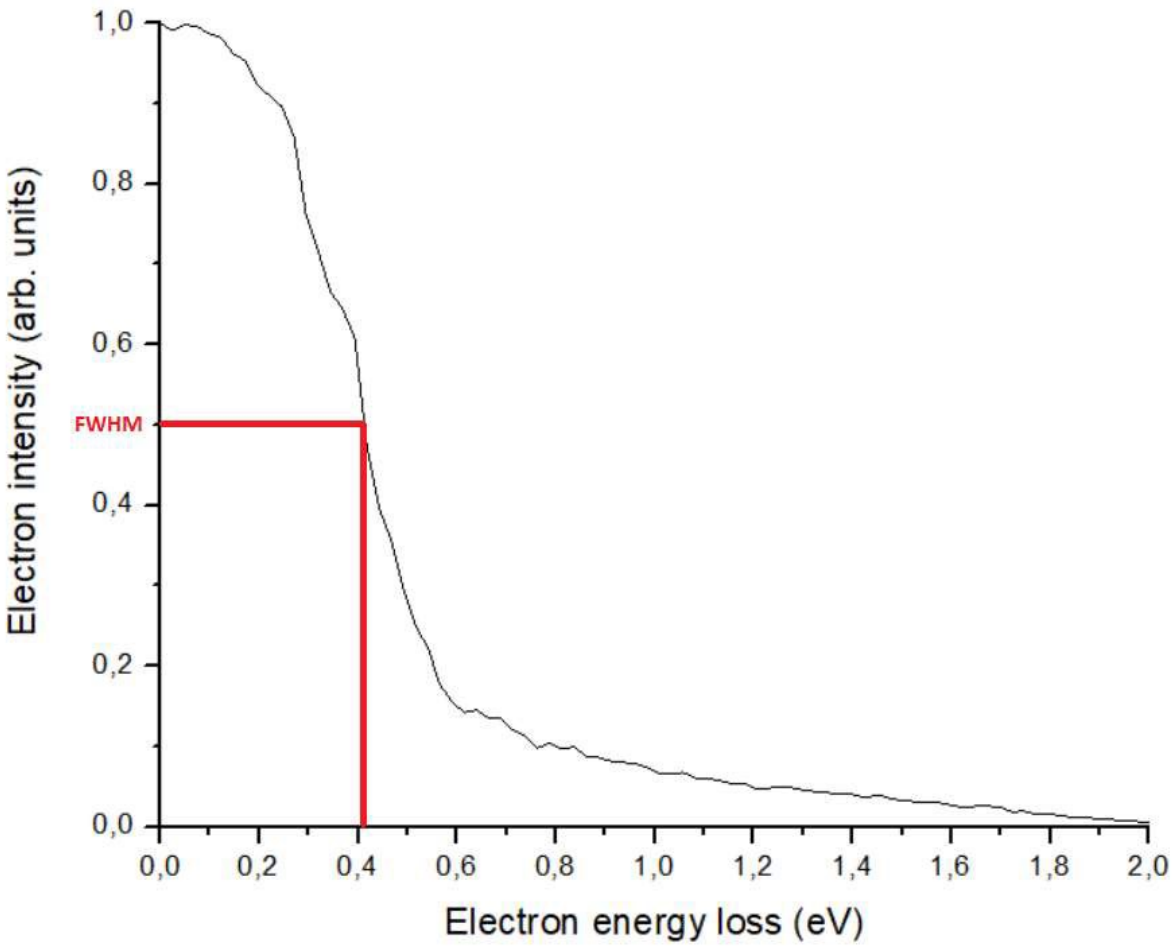

Figure 2.6. Elastic peak for an electron energy loss spectrum of nitrobenzene for incident energy of 200 eV. The resolution of the measurements in this case was lower than 600 meV.

2.1.9. Measurement protocol

All the data obtained from the detector is collected by a data acquisition system (National Instruments USB-6259, USA) connected to a computer, where a customized LabView software program (National instruments, USA) records the EEL spectra and the attenuation of the primary beam as a function of the gas pressure in the SC. Using these data, the LabView program provides the attenuation plots, the analysis fitting procedure, and the corresponding TCS values resulting from the fitted attenuation plots. The data acquisition methodology includes the following protocols:

1. Every sample was supplied by Sigma-Aldrich with a quoted purity of 99%, without any additional purification procedure performed afterwards. Nevertheless, the liquid samples were always degassed by repeated freeze-pump-thaw cycles prior to use to reduce any impurities.

2. The beam was optimized, which means the lowest current possible and the best trajectory possible, as the intensity is high enough and stable to make measurements, without surpassing saturation.
3. With the purpose of minimizing any possible multiple scattering effects, a convenient range of target gas pressures, during the attenuation measurements, had to be determined. For this work, the optimal pressure region found was from 1.0 to 7.0 mTorr.
4. For each incident energy, at least three scans were recorded to achieve a statistical reproducibility ≤ 5%.

The total electron scattering cross sections are obtained with the software program mentioned above, that has implemented the Beer-Lambert attenuation law:

$$I = I_0 . e^{-nL\sigma_T} \qquad (2)$$

where I_0 is the intensity of the primary electron beam, I is the transmitted intensity in the forward direction, n is the molecular density of the target and σ_T is the total electron scattering cross section. L represents the interaction region length which is assumed as the geometrical length of the scattering chamber. Therefore, the total scattering cross section can be derived from:

$$\ln\left(\frac{I}{I_0}\right) = -Ln\sigma_T = -\frac{\alpha L \sigma_T}{kT} P \qquad (3)$$

where it is assumed an ideal gas behaviour of the target (P and T are the pressure and temperature measurements corresponding to the n molecular density). L represents the geometrical length mentioned above and a correction factor (α) accounts for possible systematic errors arising from the measured P and L values. T is derived from $T = \sqrt{T_c T_m}$, where T_c and T_m are the temperatures of the scattering chamber measured with a thermocouple and the Baratron gauge operating temperature, respectively.

For each incident energy, at least 10 points of pressure were considered for each attenuation plot. These values were taken during the increase of the pressure, but also during the decrease, with the objective of verifying the perfect correlation between the intensity of the attenuated beam and the pressure. In Figure 2.7 there is a plot with the typical attenuation curves for impact electron energies of 100, 200 and 700 eV, together with their exponential fit curves. From the resulting slopes of the attenuation curves, we can obtain the experimental total scattering cross section.

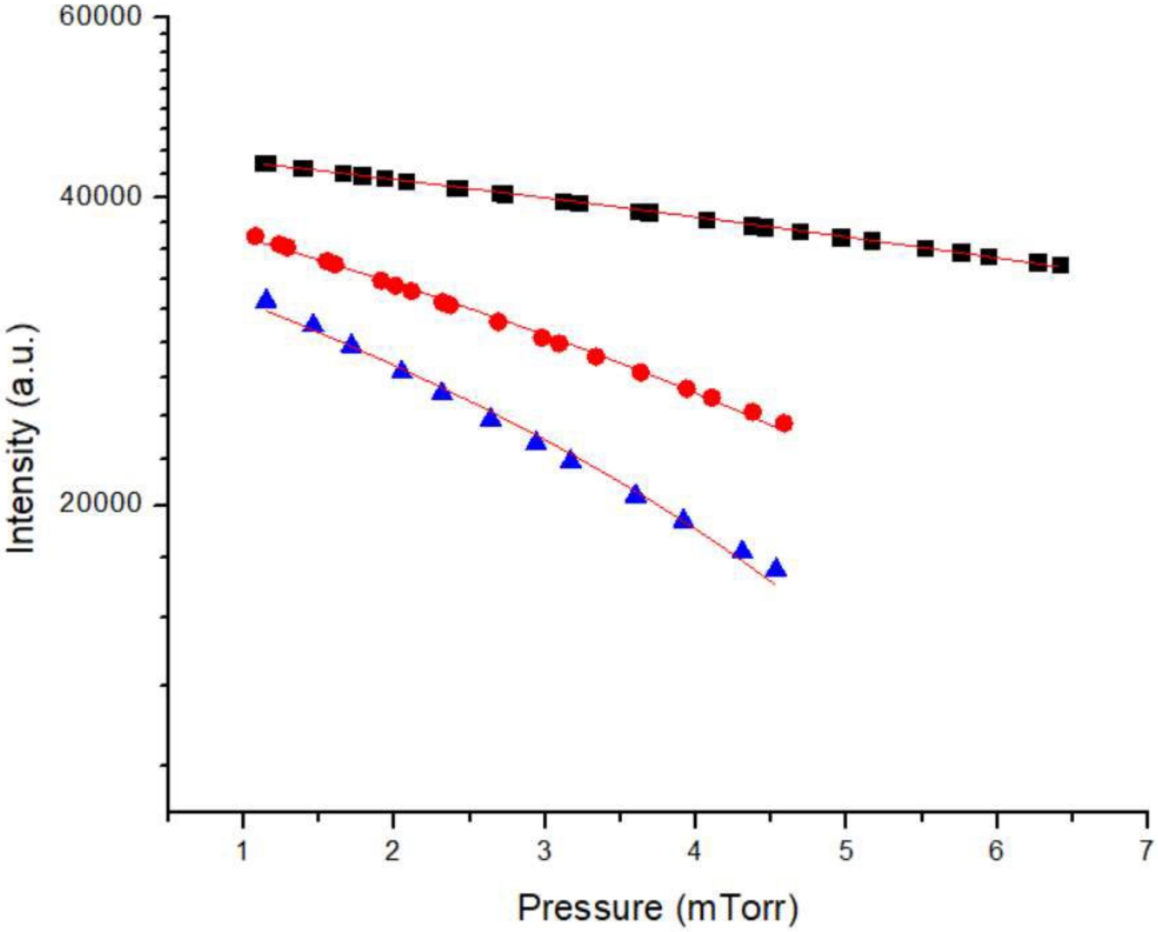

Figure 2.7. Representative attenuation curves for nitrogen with their corresponding exponential fit functions. ■ correspond to an incident energy of 700 eV, ● 200 eV and the ▲ 100 eV.

2.1.10. Calibration and optimization

Before taking new measurements, it is mandatory to monitor the quality of a well-known sample by recording electron energy loss spectra to perform a qualitative analysis of the target. Besides the energy loss study, measuring its total cross section is also essential, as it represents an important step that also validates the well-functioning of the system. In Figure 2.8 there is an energy loss spectrum of the molecule of water for 1000 eV incident energy and approximately 5 mTorr pressure. The graph provides us unique identification about the molecule to be studied. In this particular case as an example, it possible to see an inelastic peak in 7.5 eV, which is very characteristic of water, corresponding to an electronic excitation.

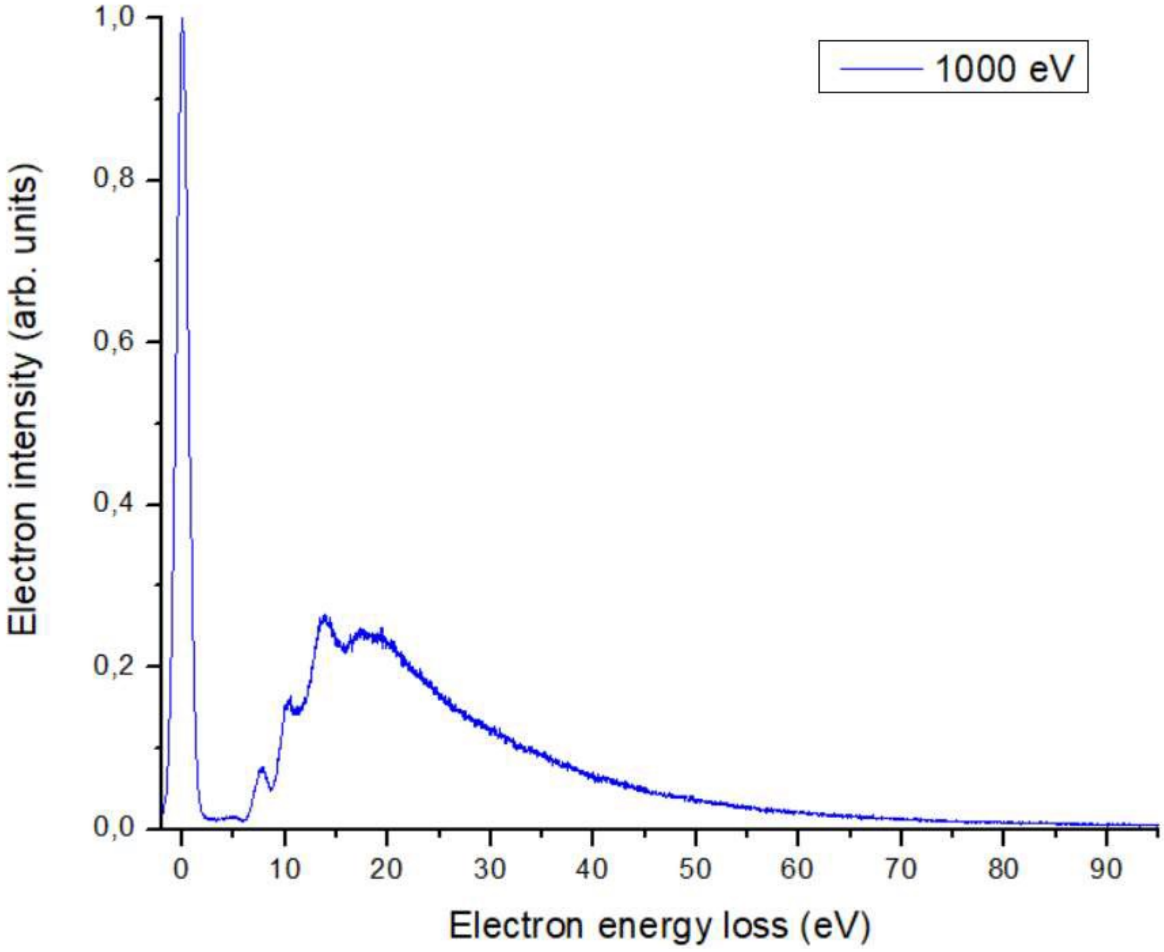

Figure 2.8. Averaged EELS measured in water for incident energy of 1000 eV.

To validate the obtained data of total cross section, it was necessary to compare the experimental data with existing reference values. The reference values picked were the recommended values by Itikawa [17]. By looking at the graphic in Figure 2.9, it is possible to see a very good agreement between both sets of data. Note that the error bars for the values presented are within the 5% error.

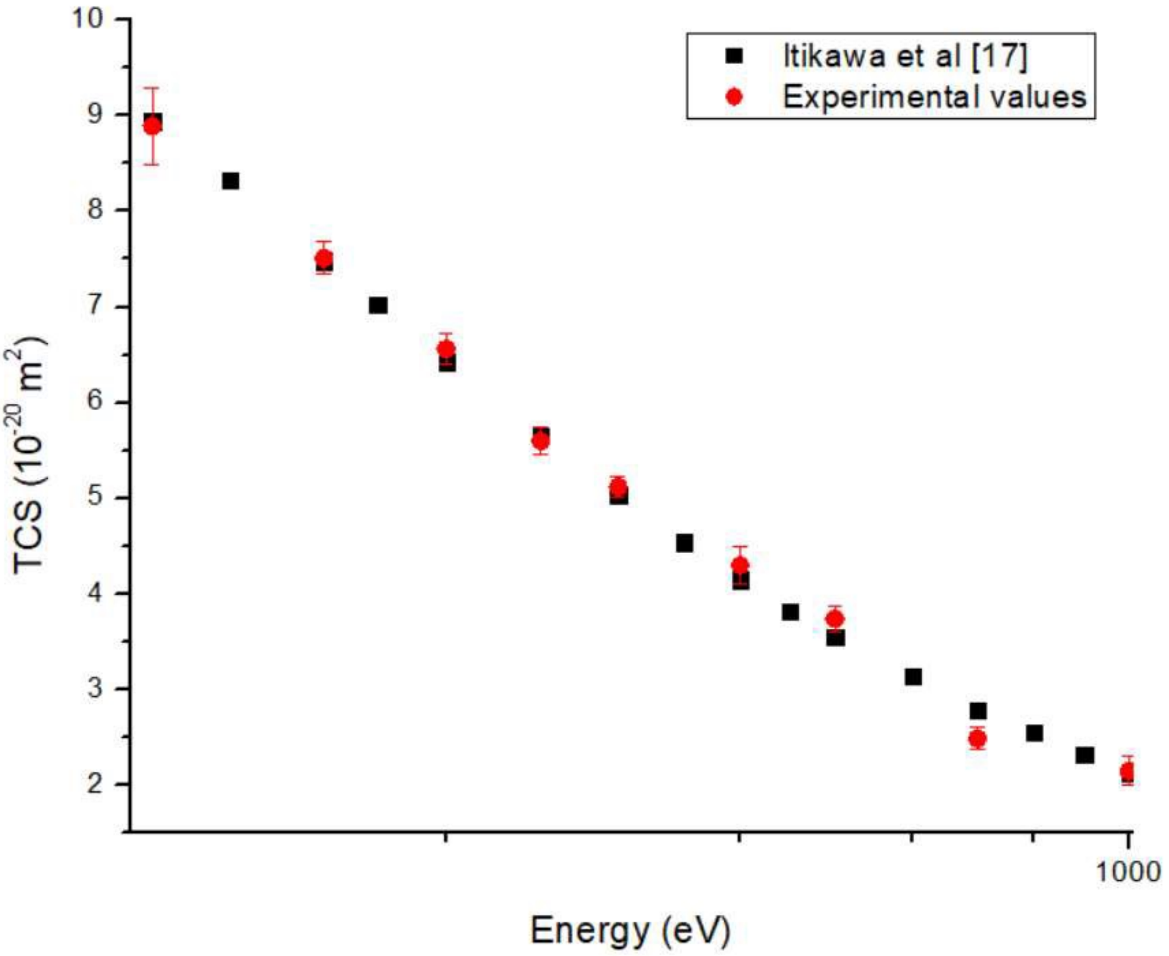

Figure 2.9. Comparison between the total cross section values of nitrogen obtained with this LTB experiment (●) and the values recommended by Itikawa (■) for the energy range of 100-1000 eV [17].

2.1.11. Experimental uncertainties

Regarding the measurements of total cross section, it is important to consider that the measurement of the pressure, temperature and other parameters also contribute with sources of error. The accuracy of the pressure measurements is assumed to be better than 1%. The temperature was measured in the collision chamber, and it is assumed to be at room temperature with an uncertainty of 1%. The experimental reproducibility of the results lies between 1.5% and 10%. Combining the above-mentioned random uncertainty sources, the total uncertainty limits of the present experimental TCSs for the incident energy range considered with the LTB system (100–1000 eV) are estimated to be within ±5%. This percentage encompasses sources of errors such as temperature variation, uncertainty in the curve fitting process and filament current.

The geometry of the experiment presents another source of systematic errors. It lies in the assumption that the actual absorption length (l) is coincident with the geometrical length of the scattering chamber

(L) and with possible pressure gradients between the electron interaction region and the Baratron gauge position which may be originated by the differential pumping system. In order to proper evaluate the influence of these systematic error sources, measurements should be repeated with different scattering geometries and the pressure should be measured even closer to the scattering chamber. The rigid configuration of the present experimental setup did not allow these to be implemented, but the effect of these factors must be proportional. These considerations create the need to introduce a correction factor (α) which accounts for possible systematic errors arising from the measured P and L values. To check the accuracy of the adjustments and approximations assumed in this experiment, it was needed to measure the electron scattering TCS for a well-known target, for instance nitrogen. In Figure 2.9, it is possible to see the values of TCS obtained with this apparatus for electrons with energy from 100-1000 eV for nitrogen.

2.2. Magnetically confined electron beam (MCEB) experiment

This experimental system is another important apparatus of the laboratory of Madrid. Some of the measurements mentioned in this thesis were made with this system, for instance, the measurements at low energies. A more detailed description of the system can be found in the work of Lozano et al. [18].

A schematic diagram of the whole apparatus is given in Figure 2.10. The system is divided in five regions: electron gun (EG), gas trap (GT), interface chamber (IC), scattering chamber (SC) and analyser-detector (AD). The primary electron beam, generated by thermionic emission by a tungsten filament in the EG region, is cooled and confined in a magnetic nitrogen GT, which reduces the initial energy spread of 700 meV down to 100-200 meV. Pulsed voltages applied to the trap electrodes in the IC region produce a pulsed electron beam with well-defined energy and narrow energy spread to enter the SC region. The SC consists of a gas cell, through which the pulsed electron beam passes and collides with a sample with a controlled pressure. Electrons emerging from the SC are analysed in energy by a retarding potential analyser (RPA) and finally detected by a double microchannel plate (MCP) electron multiplier operating in single counting mode. As it occurred for the LTB system mentioned before, the TCS is obtained from the transmitted intensity, which follows the well-known Beer-Lambert attenuation law for ideal gases. Measurement conditions, data acquisition, and data analysis are monitored and controlled by a custom designed LabView (National Instruments) program.

This experimental setup allows to perform electron beam transmission measurements providing reliable total cross section data for gaseous molecular targets. The magnetic field confinement of the electron beam ensures scattering measurements at low incident energies, where resonances may dominate. For each incident electron energy, attenuation measurements are repeated at least 5 times to ensure that the remaining statistical uncertainties can be kept below 5%. Other random uncertainties are due to temperature measurement and the numerical fitting procedure. By combining these uncertainties, a total uncertainty limit of 5% has been determined. Important systematic errors arise from the acceptance (missing) angles of the analyser-detector system, and the determination of the actual interaction region length. Nevertheless, the magnitude of the systematic errors induced by the missing angles can be properly evaluated, as well as for the interaction region length, which can be estimated by a comparison with benchmark data, for example nitrogen. In cases that incident energies are below the electronic excitation threshold of the target molecule, differential elastic cross sections can be derived from the integrated transmission spectra provided by the RPA when the target pressure in the SC is low enough to ensure single scattering conditions.

The main limitation of this system arises from the missing angles derived from the energy resolution limit. For an elastic collision, the angular resolution ($\Delta\theta$) represents the smallest scattering angle for which the detector can distinguish between scattered and unscattered electrons. Electrons elastically scattered within Δθ and 180-Δθ angles are considered by the detector as unscattered, and therefore, the total cross sections measured with the attenuation procedure tend to be lower than the real cross sections. A similar situation is found for the rotational excitation processes. Rotational excitation energies are very low, typically a few meV or tenths of meV, which are clearly lower than ΔE, so the RPA sensitivity is not able to resolve them. Note that dipole interactions are strongly peaked in the forward direction and consequently the Δθ limitation is even more critical for rotational excitation than for elastic scattering processes.

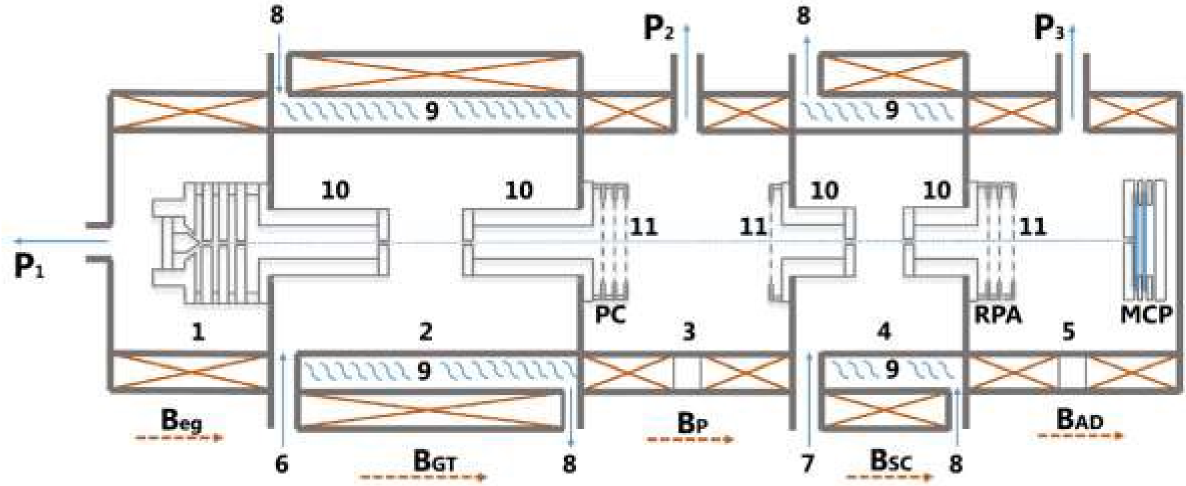

Figure 2.10. Schematic diagram of the magnetically confined electron beam system: (1) electron gun, (2) gas trap, (3) pulse-controller, (4) scattering chamber, (5) analyser-detector, (6) nitrogen inlet, (7) gas target inlet, (8) cooling water inlet/outlet, (9) water jacket, (10) scattering cell and scattering chamber focusing electrodes, (11) various transmission grids, (P_1, P_2, P_3) turbomolecular pumps, (RPA) retarding potential analyser, (MCP) dual micro-channel-plate assembly, (B_{eg}, B_{GT}, B_P, B_{SC}, B_{AD}) magnetic fields in the electron gun, gas trap, pulse-controller/interface chamber, scattering chamber and detector area, respectively.

2.3. Reaction microscope experiment

Another part of the work showed in this thesis was made in collaboration with the Max Planck Institute for Nuclear Physics (MPIK) in Heidelberg, Germany. The measurements of double and triple differential cross section were performed using a reaction microscope, an apparatus that uses a method of electron impact single ionisation commonly known as triple coincidence. More details about this system can be found in Ulrich et al [19], Dorn et al [20] and Wang et al. [21].

The reaction microscope is an apparatus used to make complete studies of electron-atom or electron-molecule collisions. Thus, it is possible to extract full information from both direction and energy of the resulting particles. A schematic diagram of the experimental setup is shown in Figure 2.11. The electron beam produced has a perfectly defined kinetic energy and it crosses the beam target inside the collision chamber, after the molecular target has been previously cooled off. After crossing with the jet projectile, the electrons will get to the detector in front of the electron gun which has a central hole that serves as projectile beam dump. Through applying both magnetic and electrical fields, the resultant fragments of the collision are detected in two time- and position-sensitive detectors, placed opposite to each other.

The electron gun consists of a cathode emitter of electrons, an anode with an orifice through which the beam of electrons can pass, and at least one focusing and control electrode. The cathode is biased to a negative voltage with respect to the interaction region, to allow any adjustments to the projectile energy. Assuming this, the total kinetic energy of the projectile electron beam can be defined as the potential difference between interaction region and the cathode. This allows the experimental setup to obtain projectile energies such as 25 eV or higher values of few keV. Moreover, there are two sets of electrodes, one situated above and the other below the collision region, parallel to each other, creating a uniform electric field capable of extracting the resulting collision particles. The two Helmholtz coils of diameter of 2 m produce a uniform magnetic field parallel to the z-axis of the spectrometer, confining the radial movement of the electrons and forcing them on cyclotron trajectories. Therefore, the purpose of both fields consists in guiding the charged final-state particles.

It is a very efficient technique since in theory it presents no restrictions concerning the scattering geometries, detection angles or energies during measures. The gathered data, that includes the time-of-flight for each particle and detection position for each collision, is then used to calculate and analyse the momentum of all resulting fragments. Let e_1 be the scattered electron and e_2 the ejected electron, using this apparatus it is possible to detect at the same time the two resulting electrons of the collision (e_1 and e_2) and one fragment ion. This method of electron impact single ionization is commonly known as triple coincidence or (e, 2e + ion) method. This is a powerful technique, which can also perform experiments on clusters, dissociation of molecules and more.

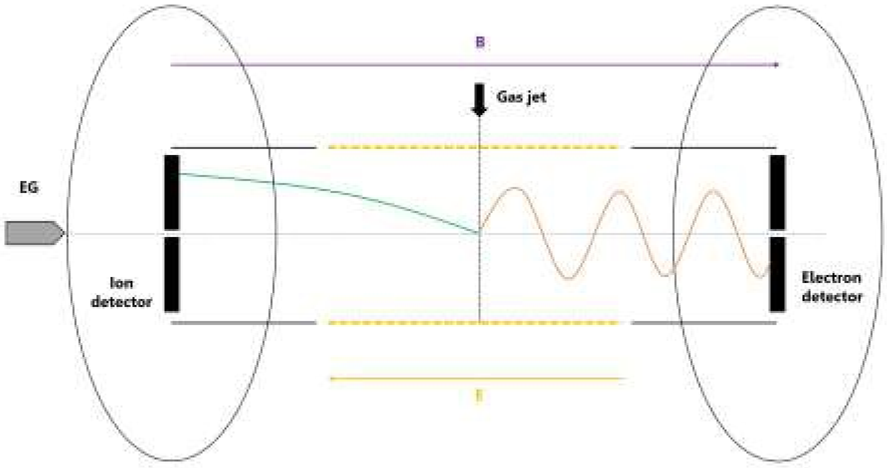

Figure 2.11. Schematic diagram of the reaction microscope used to analyse the angular and energy resolved double and triple differential cross sections.

2.4. Theoretical methods

Three different methods were used to recalculate and adapt the available theoretical data depending on the considered energy range. For the lower energies, the Schwinger multichannel (SMC) method implemented with pseudopotentials and the R-matrix procedure were used. For higher energies, the independent atom model with screening corrected additivity rule (IAM-SCAR) and interference term method was used. These three methods have been extensively used, and details on those calculation methods can be found in previous publications from Barbosa and Bettega [22][23], Gorfinkiel et al. [24] and Blanco and García [25].

Briefly, the SMC is a variational method to solve the scattering amplitude which considers the static and exchange interactions and also allows the multichannel coupling. In this application this allows for two different levels of approach to include polarization effects (SEP1 and SEP2) [26].Within this representation shape resonances can be identified from the integral elastic cross section profile. The IAM-SCAR+I method is a well-established calculation procedure which is based on an independent atom representation, but considers the molecular geometry to account for the overlapping of the atomic cross sections and additionally considers multiple scattering interference effects [30-32]. The R-matrix method allows to produce ab initio cross-sections for near-threshold ionization, as well as electronic excitation. It is based on the use of some states that represent a discretized continuum, that if chosen carefully, give a proper description of the continuum states of the target at short range.

In order to include dipole interactions, within the SMC and R-matrix schemes, the so-called “Born closure” procedure has been used, while dipole rotational excitations within the framework of the First Born Approximation have been calculated to complement the IAM-SCAR results (see Ref. [8] and references therein). The limitations of the Born approximation to properly account for dipole interactions in electron scattering cross section calculations have been pointed out by Fabrikant [29], and discussed in a recent publication [14].

Although these calculations have been performed by other members of the research group and external collaborators, the contribution of this study consisted of a critical analysis of the respective results in order to finally include them into the self-consistent data bases that we used for the present electron transport simulation.

Chapter 3. Measurements and results

The results presented in this chapter were obtained through three different types of experiments, each conducted using a dedicated apparatus and yielding specific output data. The low-energy measurements allow to detect different possible processes that mostly occur below the ionisation threshold. The high-energy measurements yielded energy loss distribution functions, which find their main application as input data for simulation models, such as Low Energy Particle Track Simulation (LEPTS). Total scattering cross sections are presented for three target molecules: benzene, nitrobenzene and pyridine. Double and triple differential scattering cross sections and integral cross sections, both elastic and inelastic, are also presented in this chapter. Benzene is already a molecule extensively studied, so the presented data is a careful look at the existent literature, and it helps with the comparison with nitrobenzene. As for nitrobenzene, there was an evident lack of other experimental total cross section determination available in the published literature, making the present measurements an important contribution to the electron-molecule scattering data pool. In the case of pyridine, the existent data is complemented, with double differential cross sections as an example, so it is possible to have a complete set of data that allows to obtain a simulation for different incident energies.

3.1. Molecules studied and respective electron energy loss spectra

3.1.1. Benzene

Benzene (C_6H_6) is a colourless, highly flammable, and volatile liquid aromatic hydrocarbon. It is considered one the simplest existent hydrocarbons, commonly known as the prototype aromatic system. It is an important nonpolar molecule with an extremely large dipole polarizability. In Figure 3.1, the 2D structure of the molecule of benzene is illustrated. It participates in several synthetic processes employed by both the pharmaceutical and petrochemical industries, displaying conjugative, delocalization, and resonance effects [30]. Benzene is a known human carcinogen, and the exposure to this substance causes neurological symptoms and affects the bone marrow causing aplastic anaemia, excessive bleeding, and damage to the immune system [31]. Despite all these negative effects, benzene serves as precursor of many biomolecules, as it plays an important role on the synthesis of different compounds.

Figure 3.1. Benzene molecule (C_6H_6).

In Figure 3.2, the average energy loss spectra obtained for an energy of 700 eV is presented. Approximately 15 single electron energy loss spectra were taken, and the gas pressure in the interaction chamber was kept between 5–10 mTorr. Despite some saturation over the area of the elastic peak, there are two excitation peaks, in 2.8 and 4.9 eV, resolved by our experiment that can be well separated from the broad ionization region. According to NIST, the ionization energy for benzene is situated at 9.2 eV [32], which proves that the resulting spectra is according to the reference values.

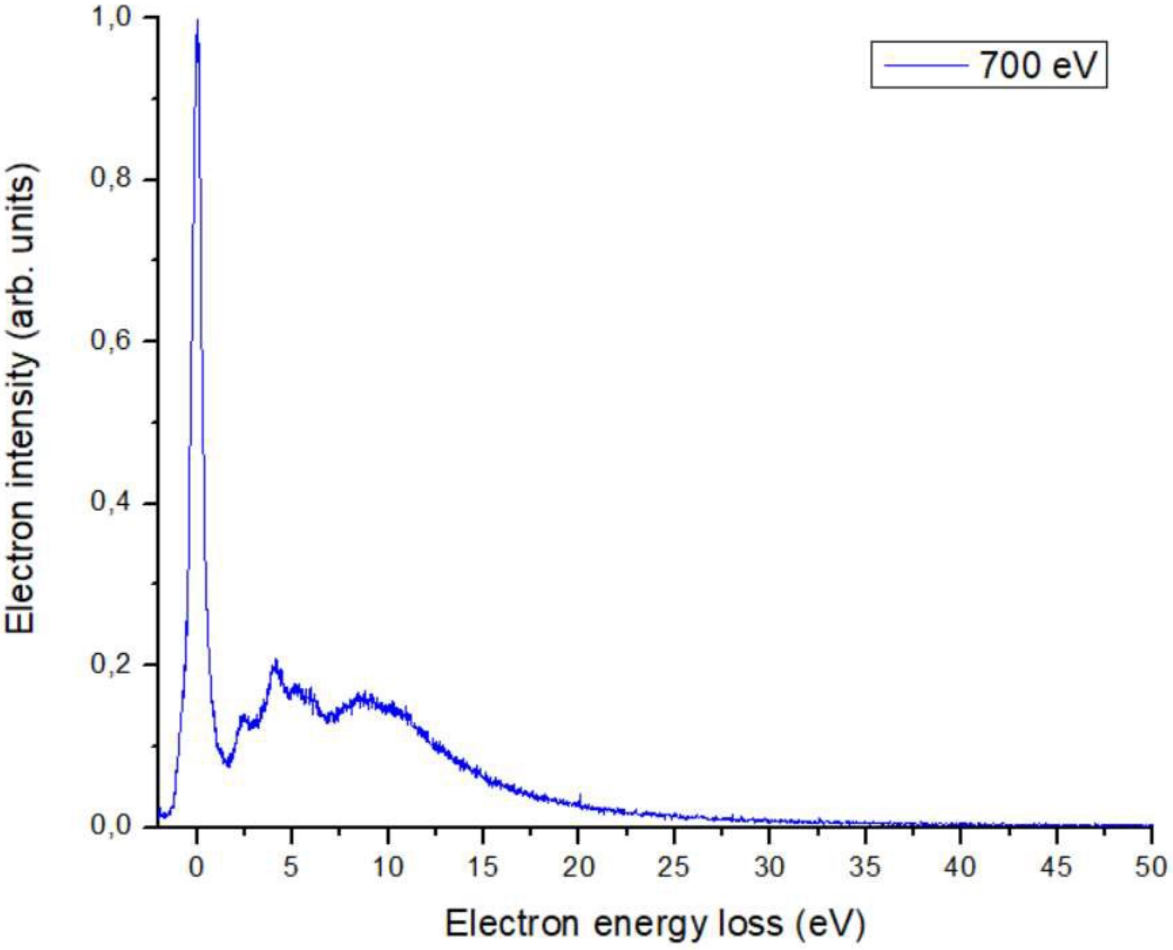

Figure 3.2. Averaged EELS measured in benzene for incident energy of 700 eV.

3.1.2. Nitrobenzene

Nitrobenzene ($C_6H_5NO_2$) is a water-insoluble pale-yellow oil with an almond-like odour. In Figure 3.3, it is presented the 2D structure of the molecule of nitrobenzene. Early experiments on nitrobenzene derivatives were devoted to analysing their potential use as radiosensitizers. Their high electron affinity related to the nitro group justified their efficiency to sensitize hypoxic cells to X-ray radiation[33]·[34]. Most of nitrobenzene is consumed in the production of aniline, which is a precursor to rubber chemicals, pesticides, dyes, explosives, and pharmaceuticals. Nitrobenzene is a polar molecule with a permanent dipole moment (μ=4.22D) and is produced on a large scale from benzene as a precursor to aniline[35]. Hence an important number of studies were related to the generation of NO_2^- radicals via electron attachment to nitrobenzene molecules [36][37][38][39][40][41].

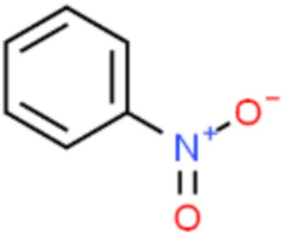

Figure 3.3. Nitrobenzene molecule ($C_6H_5NO_2$).

In Figure 3.4 it is presented the average energy loss spectra obtained for an energy of 200 eV. Approximately 20 single electron energy loss spectra were taken, and in the same way as for benzene, the gas pressure in the interaction chamber was kept between 5–10 mTorr. In nitrobenzene it is not visible any saturation over the area of the elastic peak. Although, the intensity of the inelastic region compared with the elastic peak is quite lower. There are two visible excitation peaks in 5.2 and 7.1 eV. According to NIST, the ionization energy for nitrobenzene is situated at 9.9 eV [42], which by looking at the figure, it is approximately where the slope reaches it maximum value after excitations, showing good agreement with the reference values.

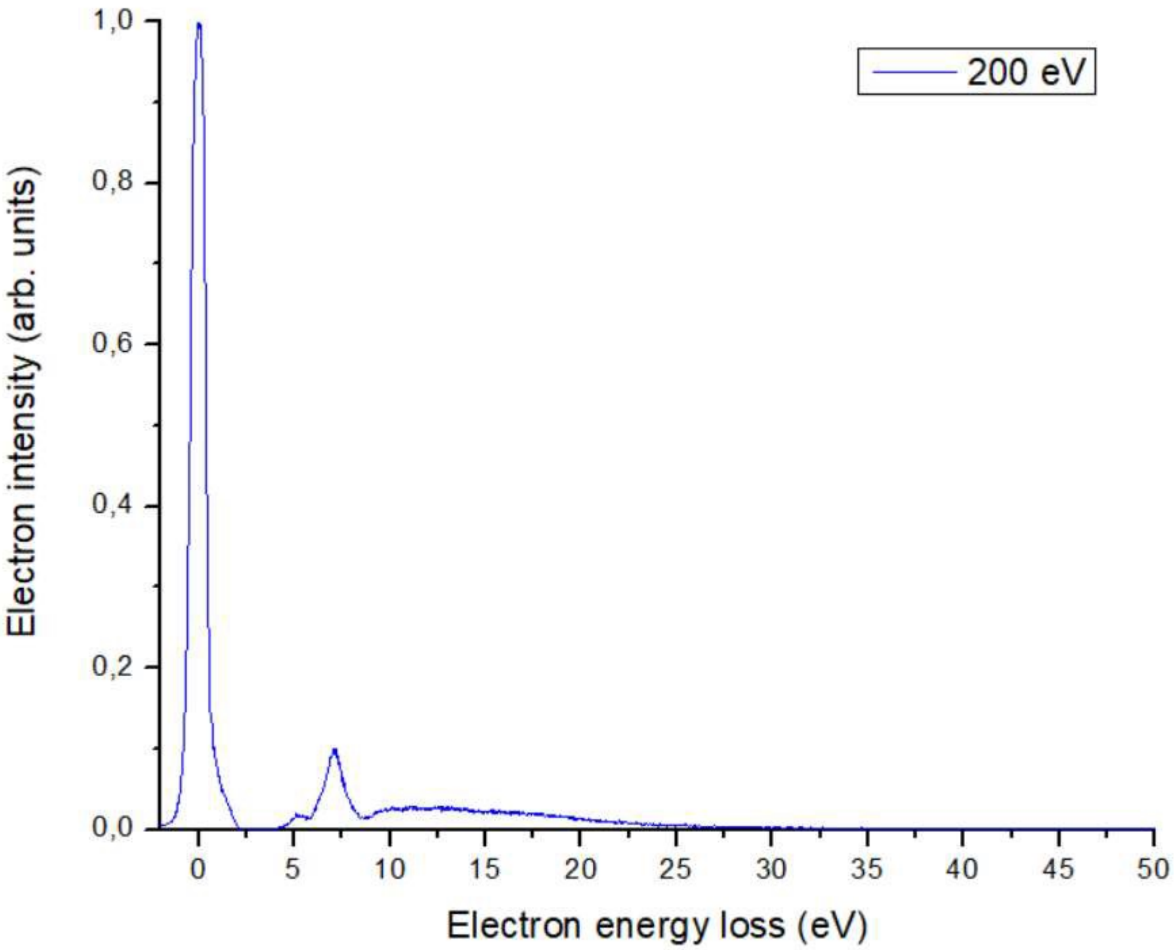

Figure 3.4. Averaged EELS measured in nitrobenzene for incident energy of 200 eV.

3.1.3. Pyridine

Pyridine (C_5H_5N) is an azaarene and is part of the class pyridines as their precursor. It comprises a benzene core in which one C-H group is replaced by a nitrogen atom. Pyridine has a permanent dipole moment of 2.2D, it is the simplest azine and at the same time an environmental contaminant [43]. Pyridine is very similar to the molecule pyrimidine, which is a diazine, with two C-H groups being replaced by nitrogen atoms at positions 1 and 3 of the benzene ring. Biomolecules, such as the nucleobases thymine (DNA), cytosine (RNA and DNA), and uracil (RNA), are created from pyrimidine, showing the importance of studying these basic structures and similar compounds [44]. In Figure 3.5, it is presented the chemical structure of pyridine.

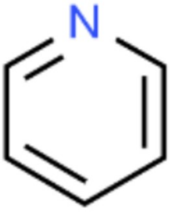

Figure 3.5. Pyridine molecule (C_5H_5N).

As it happens for the two previous molecules, the energy loss spectra have been recorded for different incident electron energies and scattering angle intervals within the range 0 and 20 degrees by deflecting the beam at the exit of the gas cell. As expected, for impact energies above 20 eV, the obtained energy loss spectra showed similar electron intensity distributions. A typical averaged (over the scattered electron angles) spectrum for an incident electron energy of 100 eV and for energy losses within 0 and 100 eV is shown in Figure 3.6.

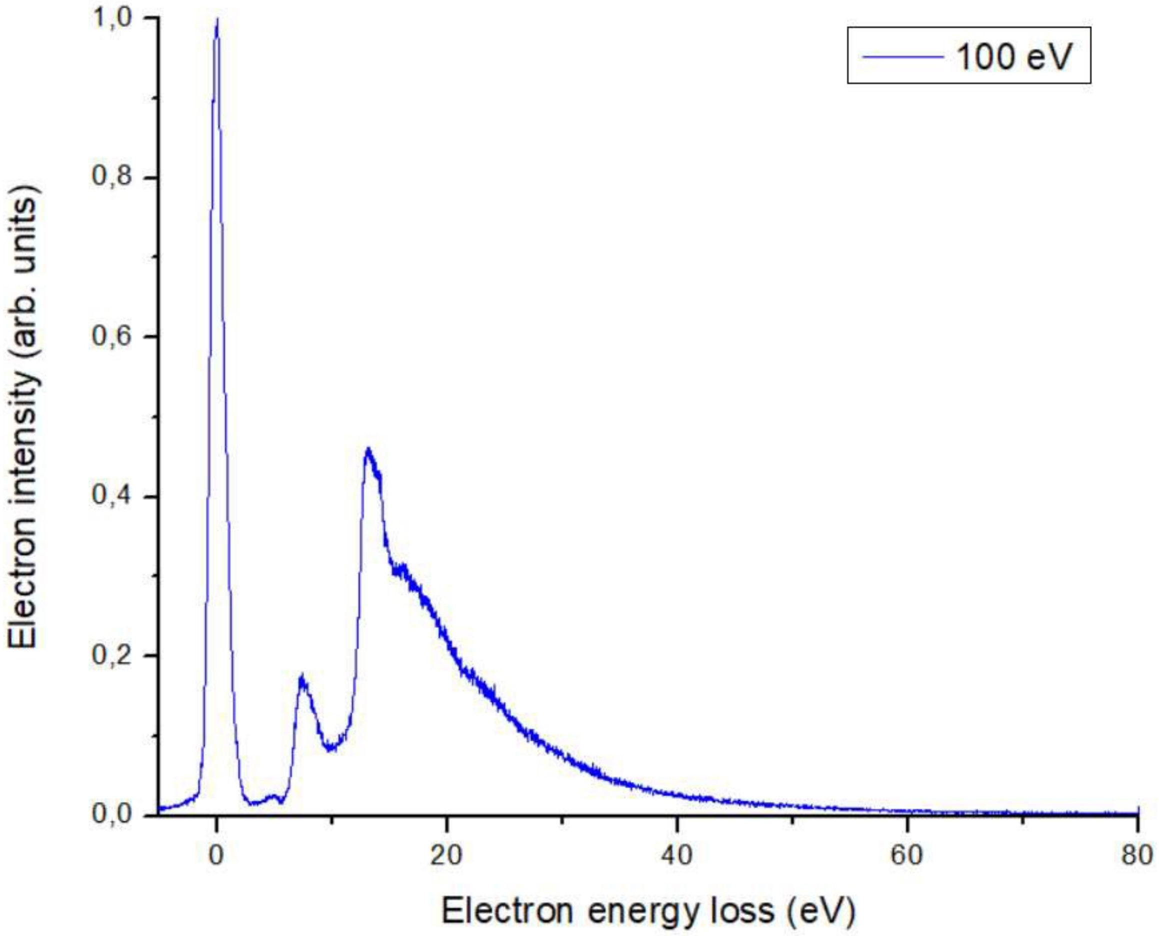

Figure 3.6. Averaged EELS measured in pyridine for incident energy of 100 eV.

3.2. Total electron scattering cross sections

3.2.1. Benzene

The original measurements of TCS at low energies (0.5–25 eV) for electron–benzene collisions, using a circular Ramsauer apparatus, were published in 1931 by Holst and Holtsmark [45]. In 1988, Sueoka [46] employed a linear-transmission-beam technique to obtain TCS values from 1 to 400 eV electron impact energies. Subsequently, Możejko et al. [47] applied a similar technique, but utilized an electron monochromator to improve the energy resolution at lower energies (0.6–250 eV) and a modified Ramsauer apparatus to extend the energy range from 90 to 3500 eV. They thus obtained TCS values from 0.6 to 3500 eV, the components of which being found to be in good agreement within the overlapping energies. With even better energy resolution, as provided by a photoelectron beam generated by synchrotron radiation, Gulley et al. [48] extended the available TCS measurements down to 0.035 eV. A critical discussion on the bona fides of these early experiments can be found in the review of Karwasz et al. [49]. More recently, both Makochekanwa et al. [50] and Kimura et al. [51] revisited Sueoka's measurements using an improved experimental arrangement.

From the theoretical point of view, Gianturco and Lucchese [52] used a model potential method to calculate integral elastic cross sections, and one-electron resonances in benzene for impact electron energies from 0.001 to 30 eV. Note that within a fixed nuclei representation, and below the electronic excitation threshold (around 4 eV), these data are equivalent to the total electron scattering cross sections, as vibrational excitation is effectively ignored. Bettega et al. [53] employed the Schwinger multichannel (SMC) method to compute elastic integral and differential cross sections for the scattering of electrons by benzene in the static-exchange and static-exchange plus polarization approximations and discussed its resonance spectra. Within the independent atom model (IAM) and using different versions of the additivity rule (AR), Jiang et al. [54], for impact energies between 30 and 3000 eV, and Sun et al. [55], in the 10–2000 eV energy range, calculated the electron-benzene TCS. Singh et al. [56] also included results of TCS calculations for electrons scattering off benzene from 10 to 5000 eV impact energies in their benzene derivatives analysis by using a modified spherical complex optical potential (MSCOP) method. Recently, Barbosa and Bettega [26] employed the Schwinger Multichannel (SMC) method implemented with pseudopotentials to carry out systematic elastic cross section calculations including a complete resonance analysis to identify any temporary anion formation and the presence of a virtual state and a Ramsauer-Townsend minimum. Finally, Prajapati et al. [57] computed the electron scattering TCS for benzene by using two different methods. The first was a R-matrix procedure provided by the Quantemol-N software [57] package for the lower energies (0,01–20 eV), while the second applied the SCOP formalism from the ionization threshold up to 5000 eV.

The present experimental TCS values for benzene, in the incident energy range 1-300 eV and as measured with the MCEB system, are shown in Table 3.1 together with their uncertainty, energy and angular resolution limits. The experimental results and their uncertainty limits for impact energies between 100 and 1000 eV, as obtained with the LTB apparatus, are shown in Table 3.2. Note that both sets of experimental results agree, to within the uncertainty limits, in the overlapping energy range (100-300 eV). On the other hand, the present theoretical data obtained with the IAM-SCAR+I method, as well as the data calculated with the SMC method, are shown in Table 3.3 and plotted in Figure 3.7.

Table 3.1. Experimental total electron scattering cross section data in benzene for low to medium energies, from the MCEB system, with their uncertainty energy (ΔE) and angular (ΔΘ) resolution limits.

Energy (eV)	σ_T (10^{-20} m^2)	Statistical uncertainty (%)	Absolute total uncertainty (±)	ΔE (eV)	Δθ (deg)
1.0	30.2	2.6	0.8	0.2	26.6
1.2	32.2	1.6	0.5	0.17	22.1
1.4	35.0	3.4	1.4	0.2	22.2
1.6	32.5	3.7	1.2	0.2	20.7
1.8	32.9	1.5	0.5	0.2	19.5
2.0	32.4	2.2	0.7	0.2	18.4
2.2	31.5	3.8	1.2	0.2	17.5
2.4	30.2	4.6	1.4	0.2	16.8
2.6	31.6	3.8	1.2	0.2	16.1
2.8	33.8	3.0	1.0	0.2	15.5
3.0	35.7	3.6	1.3	0.2	15.0
3.2	36.9	2.7	1.0	0.2	14.5
3.4	38.0	4.2	1.6	0.21	14.4
3.6	38.4	2.1	0.8	0.2	13.6
3.8	38.7	2.8	1.1	0.21	13.6
4.0	39.7	3.5	1.4	0.2	12.9
4.2	41.9	3.3	1.4	0.2	12.6
4.4	43.4	1.3	0.6	0.2	12.3
4.6	46.4	2.8	1.3	0.2	12.0
4.8	43.8	2.3	1.0	0.2	11.8
5.0	45.5	2.6	1.2	0.2	11.5
5.2	44.4	2.3	1.0	0.22	11.9
5.4	45.3	3.5	1.6	0.22	11.6
5.7	48.2	3.1	1.5	0.2	10.8
6.0	45.4	3.7	1.7	0.22	11.0
6.2	46.3	1.3	0.6	0.2	10.3
6.5	46.5	4.3	2.0	0.2	10.1
7.0	46.4	3.9	1.8	0.2	9.7
7.3	48.8	2.7	1.3	0.21	9.8
7.5	50.4	4.4	2.2	0.2	9.4
7.7	52.3	3.1	1.6	0.2	9.3
8.0	52.9	1.9	1.0	0.21	9.3
8.5	54.3	1.7	0.9	0.2	8.8
8.7	56.6	2.8	1.6	0.2	8.7
9.0	59.7	3.9	2.3	0.2	8.6
9.5	60.8	2.3	1.4	0.2	8.3

Energy (eV)	σ_T (10^{-20} m^2)	Statistical uncertainty (%)	Absolute total uncertainty (±)	ΔE (eV)	Δθ (deg)
10	58.7	2.7	1.6	0.2	8.1
11	58.8	1.2	0.7	0.2	7.7
11.5	57.6	1.6	0.9	0.2	7.6
12	55.8	0.9	0.5	0.2	7.4
13	54.9	2.0	1.1	0.2	7.1
14	53.7	3.4	1.8	0.2	6.9
15	53.2	2.3	1.2	0.19	6.5
16	52.7	1.5	0.8	0.2	6.4
16.5	51.3	1.2	0.6	0.2	6.3
17	49.5	3.4	1.7	0.2	6.2
17.5	51.2	1.2	0.6	0.2	6.1
18	52.9	3.2	1.7	0.19	5.9
18.5	51.8	1.9	1.0	0.2	6.0
19	51.0	3.5	1.8	0.19	5.7
20	49.7	4.0	2.0	0.18	5.4
22	48.4	2.0	1.0	0.19	5.3
25	47.9	1.0	0.5	0.19	5.0
30	46.6	0.6	0.3	0.2	4.7
35	46.1	1.1	0.5	0.22	4.5
40	44.1	2.7	1.2	0.22	4.3
45	43.0	3.3	1.4	0.22	4.0
50	40.7	2.2	0.9	0.25	4.1
60	38.8	0.5	0.2	0.26	3.8
70	36.8	3.5	1.3	0.26	3.5
80	34.9	2.0	0.7	0.25	3.2
90	34.0	2.9	1.0	0.25	3.0
100	32.6	1.5	0.5	0.3	3.1
120	30.9	1.0	0.3	0.3	2.9
150	28.6	0.7	0.2	0.3	2.6
200	26.6	3.4	0.9	0.3	2.2
250	23.9	2.1	0.5	0.3	2.0
300	21.4	3.3	0.7	0.3	1.8

Table 3.2. Experimental total electron scattering cross section data in benzene for medium to high energies, from the LTB system, with their error estimates.

Energy (eV)	σ_T (10^{-20} m^2)	Absolute total uncertainty (±)
100	36.53	1.69
120	34.85	0.36
150	29.48	0.35
200	26.63	0.81
250	23.87	0.88
300	21.76	0.35
400	19.07	0.68
500	16.29	0.39
600	14.67	0.72
700	13.67	0.43
800	12.69	0.23
900	11.63	0.25
1000	11.10	0.14

Table 3.3. Integral elastic cross sections (10^{-20} m^2) as calculated with the SMC method, and total electron scattering cross sections (10^{-20} m^2) as derived from the IAM-SCAR+I procedure for benzene.

Energy (eV)	SMCPP Elastic integral cross section (10^{-20} m^2)		IAM-SCAR+I Total cross section (10^{-20} m^2)
	SEP1	SEP2	
0.1	101.1	101.1	
0.2	44.65	44.66	
0.3	24.67	24.62	
0.4	15.81	15.64	
0.5	11.52	11.20	
0.6	9.554	9.063	
0.7	8.937	8.274	
0.8	9.169	8.339	
0.9	9.956	8.869	
1.0	11.10	9.960	107.8
1.2	14.32		
1.3	18.7		
1.4	71.24		
1.5	22.21	17.86	87.92
1.6	20.66	22.89	
1.7	21.50	44.90	
1.8	22.65	63.16	
1.9	23.94	37.95	
2	25.25	30.07	
2.1	26.53	28.43	78.68
2.2	27.75	28.38	
2.3	28.91	28.86	
2.4		29.52	
2.5	30.96	30.25	
3	34.81	33.61	
3.5	37.70	36.47	71.40
4	39.43	38.33	
4.3	41.33	40.35	67.20
4.5	43.35	42.46	
4.8	49.53	48.78	
4.9	51.23	50.53	
5	50.97	5032	
5.3	46.85	46.46	63.56
5.5	46.34	45.95	
5.8	46.84	46.59	
6	49.98	49.83	
6.5	48.77	48.85	
7	50.13	50.39	
7.5	53.41	53.84	59.92
8	51.83	52.38	
8.5	52.42	53.06	
9	51.19	51.90	
9.5	52.51	53.28	
10	52.55	53.37	57.12
12	50.66	51.44	
14	49.92	50.02	
15	49.87	48.75	54.88
20			53.76

Energy (eV)	SMCPP Elastic integral cross section (10^{-20} m^2)		IAM-SCAR+I Total cross section (10^{-20} m^2)
	SEP1	SEP2	
30			52.08
40			49.56
50			46.76
70			42.56
100			37.8
150			32.48
200			28.28
300			23.1
400			19.54
500			17.05
700			13.61
1000			10.53
2000			6.05
3000			4.26
5000			2.68
10000			1.38

Looking at the presented data, below 10 eV the IAM-SCAR+I approach is not accurate, and only qualitative information can be expected from it for such low energies (see Figure 3.7). The SMC calculation gives the integral elastic cross sections, but below 7 eV, where electronic excitations are not significant, it can be considered that they are approximately equivalent to the TCS (i.e. assuming vibrational excitation is small [58]). As shown in Figure 3.7, for incident energies within 7-10 eV, there is a fair concordance between the results given by the two calculation methods. This allows, with only a minor upward scaling of the SMC (SEP2) result, to combine them to derive a complete set of calculated TCSs over the whole energy range (0.1-10000 eV). As the merged data (labelled in Figure 3.8 as SMC-SCAR) are based on both calculations in their respective energy ranges of validity, an uncertainty limit of ± 10% can be estimated. This figure is based on results from previous comparisons between calculated and experimental data for similar targets including pyridine [4,5] and *p*-benzoquinone [60]. Comparing with other available calculations (see Figure 3.7), apart from the resonances that will be discussed later, Gianturco and Lucchese [52] give integral elastic cross sections lower in magnitude than ours, for the energies where they are roughly equivalent to the TCSs, with a maximum discrepancy of about 20% at around 5 eV. As expected, the additivity rule (AR) method used by Jiang et al. [54], even with some energy dependent correction, fails below 100 eV where they overestimate the total cross section values. Since this method does not consider interference terms [28], it tends to give TCS values lower than our SMC-SCAR hybrid for higher energies (> 100 eV), being about 50% lower in magnitude than ours at 3000 eV. Sun et al. [55] proposed a modified additivity rule method, aiming to improve its reliability for the lower energies. Sun's results [55] are almost coincident with those from Jiang et al. [54] for energies above 100 eV, but they correct Jiang's data [54] below 100 eV now giving TCS values in good agreement with those of the present calculation down to 10 eV. The so-called MSCOP method of Singh et al. [56] provided TCS values for impact energies between

10 and 5000 eV. Basically, it is a single centre optical potential method, applied to different groups within the molecule, to finally generate a cross section by adding the corresponding results for each group [56]. TCSs calculated by Singh et al. [56] are higher than ours by about 50-60% between 10 and 100 eV, but tend to converge to ours for increasing energies. Lastly, Prajapati et al. [57] used a similar SCOP method in combination with an R-matrix calculation [61] based on the commercial Quantemol-N [62] software package. Their results for the lower energies (corresponding to the Quantemol-N code) are in clear disagreement with those from our SMCPP method (see Figure 3.7). However, their SCOP results agree reasonably well with our IAM-SCAR+I values from 20 to 1000 eV, although their energy dependence [57] for increasing energies tends to diverge from ours.

In order to compare our results with those from previous measurements, the present experimental and theoretical TCS results, in particular our hybrid theoretical TCS result, are plotted in Figure 3.8 together with those experimental values available in the literature for incident energies ranging from 1 to 1000 eV. Early measurements from Sueoka [46] show a reasonable agreement (to within ~10%) for the lower energies, from 1 to 7 eV. Above this energy, however, his TCS values are systematically lower than the present data by about 25%. This discrepancy may be attributed, at least in part, to the poorer energy resolution of the TOF analyser used in Ref. [46]. Mozejko et al. [47] present two sets of TCS data: results from Gdansk for incident energies between 0.6 and 250 eV and measurements from Trento for 90-3500 eV impact energies. Comparing our data with those for the lower energies, it was found good agreement, to within the stated uncertainty limits, from 1 to 25 eV. Above 25 eV their values tend to be lower in magnitude than ours, reaching maximum discrepancies of about 30% at around 200 eV. The energy resolution of the Gdansk apparatus is good enough to avoid contamination from most inelastic channels, but this is not probably the case in respect to their angular resolution. The contribution of electrons elastically scattered into the acceptance angle (0.7 msr) of their detector [47] is not discussed in Ref. [47], but it could lower their observed TCS values by about 15-20% at 200 eV. As discussed in previous publications [63] (see Ref. [63] and references therein), this systematic error is really quite significant for a Ramsauer-type apparatus such as that used in Trento [47]. Comparing the higher energy results from Trento with those of the present LTB system (with $<10^{-5}$ sr angular acceptance), the former is about 42% lower in value than ours at 1000 eV. High resolution measurements using photoelectron (from synchrotron radiation) beams were carried out by Gulley et al. [48], for impact energies below 2 eV. Their results, being generally higher in magnitude than the present ones, nonetheless agree with ours to within 15% even for the position and magnitude of the local peak maximum at around 1.4 eV. However, they found two other maxima at energies of around 1.17 and 1.29 eV that are not present in our results. Makochekanwa et al. [50] and Kimura et al. [51] repeated the earlier measurements from Sueoka [46] in order to improve their accuracy, and as shown in Figure 3.8, those new results are in very good agreement with the present experimental data from 1 to 200 eV. Above this energy, nevertheless, their results tend to be lower than ours reaching a maximum discrepancy of about 17% at 1000 eV. This discrepancy seems to be related to the different angular resolutions of the respective experimental configurations and will be discussed later.

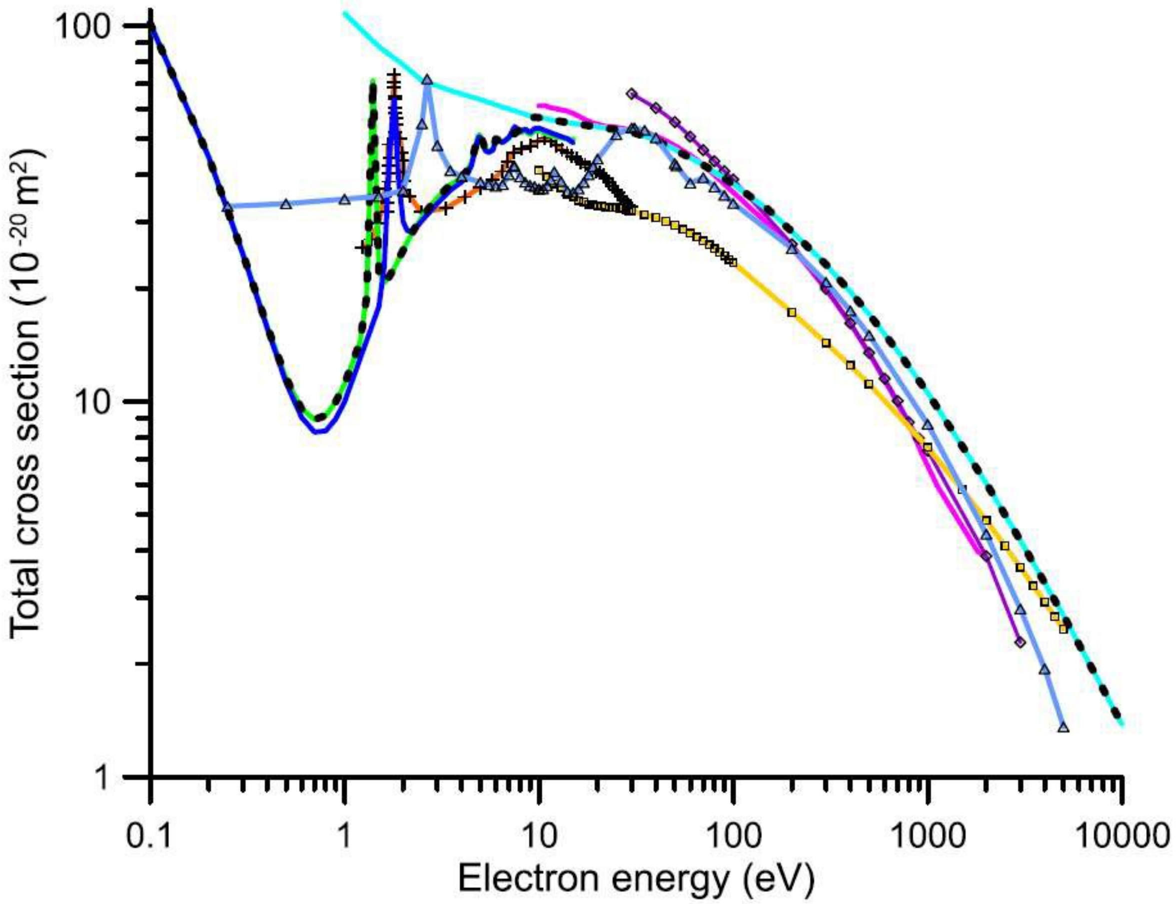

Figure 3.7. Present TCS and elastic ICS calculations together with other theoretical values available in the literature: SMC with SEP2 (—); SMC with SEP1 (—); IAM-SCAR+I (—); SMC-SCAR merged (---); Gianturco and Lucchese [52] (—); Jiang et al. [54] (—); Singh et al. [56] (—); Prajapati et al. [57] (—); Sun et al. [55] (—).

An interesting practical aspect in comparing experimental and theoretical TCS values is the possibility of identifying electron scattering resonances which have been theoretically predicted. The two approaches used to describe the polarization (SEP1, SEP2) in our SMC method lead to a different representation (energy position and width) of the resonances (see Ref. [26] for details). In the energy range 1-10 eV it was possible to identify increments on the present measured total cross section around specific energy values (which was associated with the resonances). It was found a first local maximum at 1.4±0.2 eV which coincides with the energy of the $^2E_{2u}$ electronic state of the benzene anion [43,44], and can be attributed to electron attachment to the π^* virtual molecular orbital [48]. This position is in excellent agreement with our SMC-SEP2 calculation, which placed a π^* shape resonance at 1.4 eV, having a width of 0.05 eV. Note that this structure was also found by Mozejko et al. [47] and

Makochekanwa et al. [50] associated with the $^2E_{2u}$ resonance. Gulley et al. [48] actually found three peaks in their TCS measurements. One was located at 1.4 eV but the other two were at 1.29 and 1.17 eV, respectively. There is no other experimental evidence for these two lower energy peaks, but it should be observed that the energy resolution of Gulley's experiment (~3.5 meV) allowed them to distinguish the vibronic components of this electronic resonance whilst the other results give averaged cross sections over their respective energy resolutions (200 meV in the present case). Hence, there is no conflict between our observations and that of Gulley et al. [48]. Electron transmission experiments from Sanche and Schulz [66], Nenner and Schulz [67] and Burrow et al. [68] did resolve the vibronic structure of this resonance, finding the first peak at 1.14, 1.14 and 1.12 eV, respectively. Calculations from Gianturco and Lucchese [52] placed this resonance at 1.82 eV, in concordance with the 1.8 eV position derived from our SMCPP-SEP1 results. The SMC calculations of Bettega et al. [53] located this resonance at 2.3 eV. The recent calculation of Prajapati et al. [57], using the R-matrix method with the Quantemol-N code, found the first peak of the TCS at 2.67 eV in clear disagreement with all previous theoretical and experimental studies. This might reflect their using a radius, typically 10 a_0 in R-matrix applications, that is too small to accurately account for the anionic structure. Going to higher energies, it can be distinguished a shoulder on the TCS energy dependence at around 3.4 eV, which is coincident with the local maximum found by Holst and Holtsmark [45] at 3.5 eV. The origin of this peak is not clear, but it should be noted that similar structures were visible in the benzene derivatives [10] pyridine and pyrimidine which were attributed to the vibrational excitation of the ground state (see Ref. [10] and references therein).

The next maximum identified is located at 4.6 ± 0.2 eV, confirming our calculated resonance for which both the SEP1 and SEP2 methods predict a position in the peak at 4.9 eV with a width of 0.56 eV. This peak can be interpreted as a π^* resonance ($^2B_{2g}$ symmetry) which is a mixture of a shape and a core excited resonance due to the presence of triplet excited states near the shape resonance energy [69]. Li et al. [70] computed, for the vertical excitation energy of the 1^1B_{2u} state, a value of 5.06 eV, which is in excellent agreement with the energy loss spectra recorded by Doering [71]. Electron transmission experiments also found this resonance to be at 4.82 eV [68] and 5.1 eV [66]. Due to the energy resolution limitations in the other available experiments, this resonance presents as a shoulder on the energy dependence of the TCS between 4.5 and 5 eV [17,18,21]. This feature is not noted in the calculations of Gianturco and Lucchese [52] and Prajapati et al. [57], but they rather found resonances at 7.44 and 7.41 eV, respectively. Bettega et al. [53] reported this resonance at 8.3 eV. Azria and Schulz [72] suggested that this resonance could not only decay in the ground state ^1A_g but also in the $^3B_{1u}$, $^3E_{1u}$, and $^1B_{1u}$ excited states. Allan [73] reported that the $^2B_{2g}$ resonance has a relatively large importance in the excitation of the $^3B_{1u}$, $^3E_{1u}$ states, which confirms the interaction of a $^2B_{2g}$ shape-resonance with a $^2B_{2g}$ core-excited resonance. In addition, at 5.7 ± 0.2 eV it is possible to distinguish a weak local maximum in our TCS values, which may correspond to the "Feshbach" resonance at 5.87 eV proposed by Allan [73] and associated to the 3s (a_{1g}) Rydberg state. Between 6.5 and 8 eV our experimental cross section increases more rapidly in magnitude, as a result of a superposition of electronic excited states [43,49–51]. The absolute maximum value of the present TCS measurements, (60.8 ± 1.4) x 10^{-20} m^2, is reached at 9.5 eV, forming a broad structure around it. As the first ionization threshold in benzene is 9.2 eV [74], and considering the high density of accessible states around this energy, our results do not have a good enough energy resolution in order to analyse the composition of such a broad structure. However, similar broad maxima within 8-10 eV can be found in most representative experimental and theoretical studies [18,21,23]. Allan [64] justified this broad maximum as being due to a $^2E_{1u}$ shape resonance produced by incident electron attachment to the σ* (e_{1u}) orbital. Note that Prajapati et al. [57] calculated the absolute maximum of the TCS at 30 eV, in disagreement with all the previous studies. Nonetheless note that our experimental TCSs do show a shoulder at around 30 eV, that may be coincident with the maximum in the sum over all the electronic-state excitation integral cross sections [30].

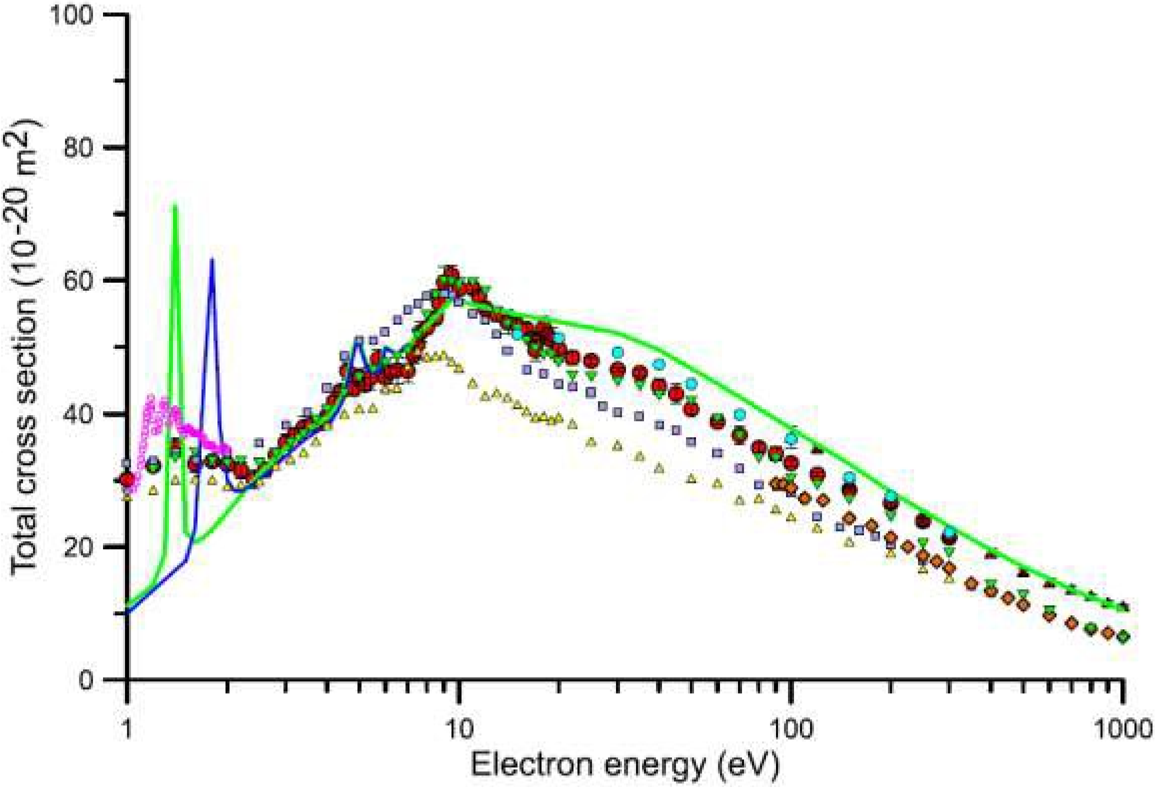

Figure 3.8. Available experimental and present theoretical total cross sections for electron scattering from benzene: present experimental data with MCEB (●); present experimental data with LTB (▲); calculation SMC-SCAR (SEP2) (▬); calculation SMC (SEP1) (▬); Sueoka et al. [46] (▲); Mozejko et al. [47] (■),Zecca et al. [47] (♦); Makochekanwa et al. [50] (▼); Gulley et al. [48] (○); IAM-SCAR+I-Δθ (●).

Concerning the higher energies and looking at Figures 3.7 and 3.8, there are some quite serious discrepancies between the energy dependencies given by the different measurements and calculations. However, this energy dependence is crucial for modelling radiation damage [11]. Monte Carlo track simulations [11] start from high energy (typically in the MeV range) electrons, which subsequently slow down in the medium by successive collision processes until their final thermalization [75]. Collisional data for energies above 10 keV are customarily taken from atomic electron scattering cross section libraries (e.g. the LLNL Evaluated Electron Data Library [76]), which are based on the first Born approximation [13,55,56]. To ensure consistency between the low-intermediate (0-10^3 eV) and high-energy (>10^4 eV) domains, the energy dependence of the TCS should smoothly overlap in the range (10^3 - 10^4 eV). The high-energy dependence of the total cross section can easily be derived by assuming that at such high energies the molecules behave as a sum of atoms, with the energy dependence of the atomic total cross section (σ_T) being given by the Born formula [55,56]:

$$\sigma_t = \frac{A}{E} + \frac{B}{E} \ln E + \cdots \qquad (4)$$

where E represents the incident electron energy and A and B are constants related to the oscillator strength distribution of the target [55,56]. Only first order terms are represented in Eq. (4), so it can be considered as the asymptotic energy dependence of the total cross section derived from the Born approximation. The first term in the above series represents the contribution of elastic scattering, while the second accounts for the inelastic processes (electronic excitation and ionization). Note that in a logarithmic plot both terms give straight lines whose slopes are -1 and -0.87, respectively (see Figure 3.9). In order to compare this energy dependence with that of the available TCS values, it was plotted where possible in Figure 21 the theoretical and experimental data shown in Figures 3.7 and 3.8, for energies above 500 eV, but normalizing to a value of 10 their respective results at 500 eV. As can be seen in Figure 3.9, the previous calculations do not give asymptotic energy dependencies in agreement with the Born approximation. Assuming that Eq. (4) reasonably represents the energy dependence of the total cross section for electron energies above 1000 eV, it was found that the results from both Jiang et al. [54] and Prajapati et al. [57] lead to slopes higher than -1. This is in clear contradiction with the E^{-1} energy dependence of the Born elastic cross section. In contrast, results from Singh et al. [56] give a slope lower than -0.87 and thus underestimate the $E^{-0.87}$ energy dependence of the Born inelastic cross sections. However, as shown in Figure 3.9, the corresponding slope from our IAM-SCAR+I method for energies above 1000 eV, is -0.92 thereby giving an $E^{-0.92}$ energy dependence for the TCS which is in good agreement with that predicted by the Born approximation. Therefore, it is possible to fit our calculated TCSs from 1000 to 10000 to the expression given by Eq. (4) obtaining:

$$\sigma_T(10^{-20}\mathrm{m}^2) = \frac{4392}{E(\mathrm{eV})} + \frac{1035}{E(\mathrm{eV})} \ln E(\mathrm{eV}) + \cdots \qquad (5)$$

This expression therefore allows us to extrapolate the TCS values for energies above 10 keV. Note that for very high energies, say above 100 keV, relativistic electron mass-velocity relationships should be included in Eq. (5) for a proper extrapolation.

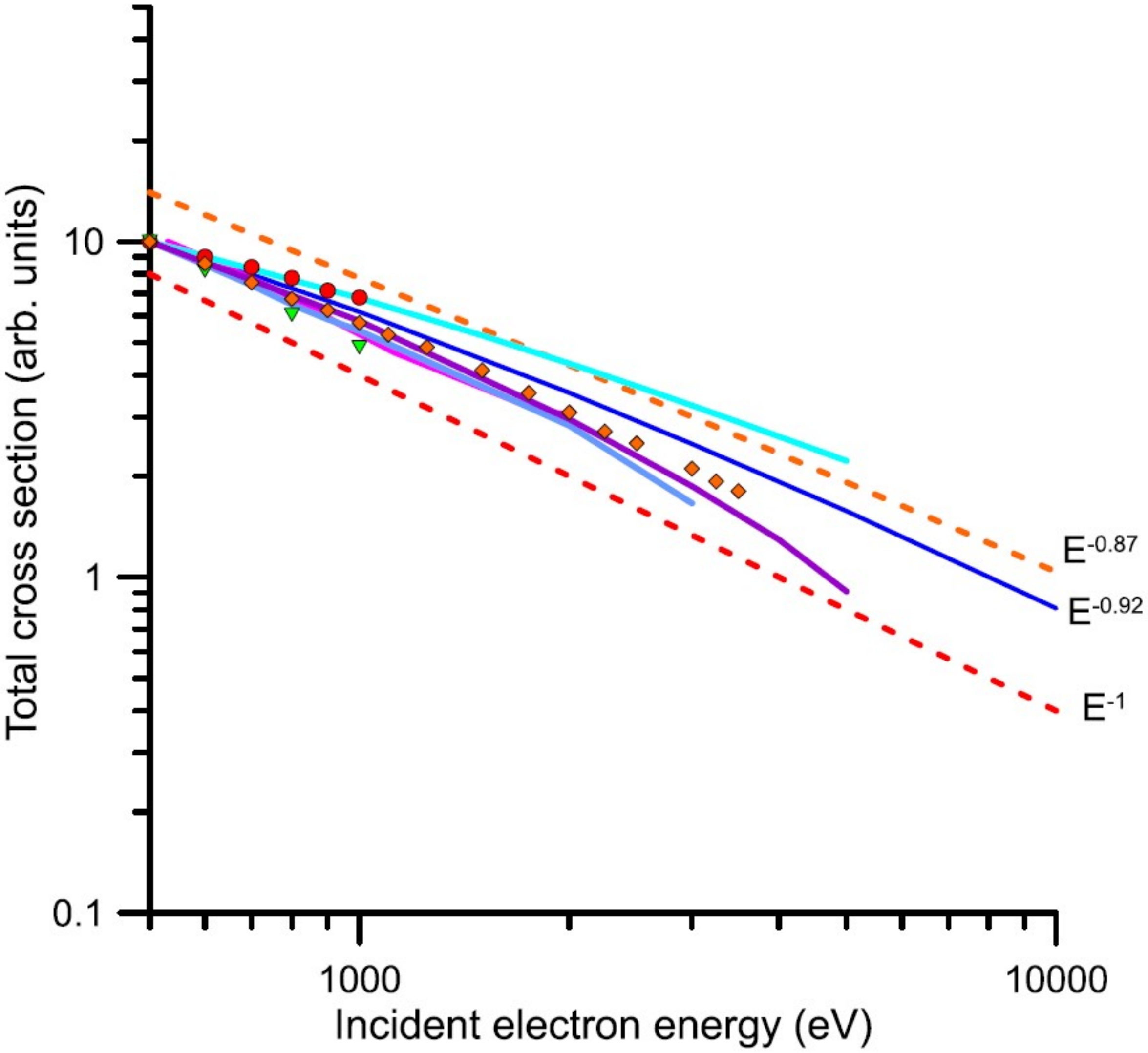

Figure 3.9. Energy dependencies of the present and previous experimental and theoretical TCSs for energies above 500 eV; Elastic-Born (---); Inelastic-Born (---); IAM-SCAR+I (▬); Sun et al. [55] (▬); Jiang et al. [54] (▬); Singh et al. [56] (▬); Prajapati et al. [57] (▬); present experimental data (●); Makochekanwa et al. [50] (▼); Zecca et al. [47] (♦).

3.2.2. Nitrobenzene

Nitrobenzene is a polar molecule with a permanent dipole moment ($\mu = 4.22\ D$) [80] that is large enough to support dipole-bound states. This property motivated some early low energy electron scattering experiments [81][82][83] from nitrobenzene, in order to check the validity of the popular rotational excitation approaches which are customarily used in modelling some of the aforementioned applications. Long-range effects in electron scattering by polar molecules calculations and their implications in experiment to theory comparison have been recently reviewed by I. Fabrikant [29]. Different theoretical and experimental spectroscopic studies have also been published along the years, in order to characterise its ultraviolet emission spectrum [84][85], electronic structure and spectra [86][87][88][89][90], vibrational spectra [91], electron energy loss measurements [92][93], electron transmission measurements [94], photoabsorption spectra [95] and angular resolved photoelectron emission [96][97]. All the previous work shed light on the valence electronic structure of this important molecule. From the theoretical point of view, electron scattering from nitrobenzene molecules has been recently investigated by Maioli and Bettega [98] using the Swinger multichannel (SMC) method with pseudopotentials. They calculated differential and integral elastic as well as momentum transfer cross sections for electron impact energies ranging from 0 to 10 eV.

The results of total electron scattering cross sections (in Å^2) for nitrobenzene with impact energies ranging from 0.4 to 250 eV, as measured with the MCEB system, are shown in Table 3.4. The results of our IAM-SCAR+I and Born-Dipole calculations (integral elastic, rotational excitation, summed electronic excitation and ionisation cross sections) for impact energies ranging from 1 to 1000 eV are shown in Table 3.5. As already mentioned, from previous comparisons with experimental data for other similar molecules [99][100][10][101][60][5], it is possible to establish an overall uncertainty of ~10% for the IAM-SCAR+I integral cross sections. The exception to that general claim is for ionisation, for which uncertainties around the ionisation threshold could be of the order of 20-25% [102][103]. Below 10 eV our IAM-SCAR+I method does not in general apply, and so those results are shown in Table 3.5 just for completeness. The total electron scattering cross sections measured with the LTB apparatus in the impact energy range 100-1000 eV are shown in Table 3.6 with their respective experimental uncertainty limits. These results are also plotted in Figure 3.11, together with those measured with the MCEB apparatus and the present IAM-SCAR+I calculation data (not including rotational excitations).

Table 3.4. Experimental total electron scattering cross section data for nitrobenzene in the energy range of 0.4-250 eV, together with their corresponding uncertainties and energy (ΔE) and angular (Δθ) resolution limits.

E (eV)	TCS (10^{-20} m^2)	Relative uncertainty (%)	Absolute uncertainty (± 10^{-20} m^2)	Δθ (deg)	ΔE (eV)
0.4	58.8	1.7	1.01	40.7	0.17
0.5	57.1	3.0	1.71	35.0	0.18
0.6	55.7	2.7	1.50	33.2	0.18
0.7	54.9	3.0	1.62	31.0	0.19
0.8	54.2	4.9	2.66	29.2	0.19
1.0	63.0	2.4	1.52	24.4	0.17
1.2	61.3	1.8	1.11	21.4	0.16
1.4	59.1	1.0	0.62	21.6	0.19
1.5	59.6	1.0	0.6	21.7	0.20
1.6	55.9	3.1	1.71	21.8	0.22

E (eV)	TCS (10^{-20} m^2)	Relative uncertainty (%)	Absolute uncertainty (± 10^{-20} m^2)	$\Delta\theta$ (deg)	ΔE (eV)
1.8	59.3	2.6	1.54	17.9	0.17
2.0	60.1	1.8	1.08	18.0	0.19
2.2	58.9	2.2	1.32	16.1	0.17
2.4	59.3	2.1	1.27	17.6	0.22
2.6	60.4	1.6	0.99	15.3	0.18
2.8	61.7	2.1	1.27	15.1	0.19
3.0	61.4	1.6	1.01	14.2	0.18
3.2	61.2	1.9	1.15	12.9	0.16
3.4	62.1	2.5	1.56	12.9	0.17
3.6	63.8	2.4	1.54	12.9	0.18
3.8	64.5	3.0	1.92	12.9	0.19
4.0	65.5	2.5	1.64	12.9	0.20
4.2	64.9	1.3	0.83	12.6	0.20
4.4	64.4	2.1	1.38	12.3	0.20
4.6	63.6	2.6	1.65	11.4	0.18
4.8	64.9	3.0	1.93	11.2	0.18
5.0	65.8	2.8	1.83	11.2	0.19
5.2	65.6	2.9	1.89	11.6	0.21
5.4	65.3	1.5	0.97	11.6	0.22
5.6	65.4	2.6	1.70	11.7	0.23
5.8	66.7	2.3	1.55	11.0	0.21
6.0	68.9	3.2	2.18	11.0	0.22
6.2	71.1	2.5	1.78	11.3	0.24
6.4	72.8	1.0	0.76	10.7	0.22
6.6	71.6	1.3	0.92	10.8	0.23
6.8	73.1	3.4	2.52	9.6	0.19
7.0	71.7	2.0	1.41	10.0	0.21
7.3	72.9	3.8	2.79	10.2	0.23
7.5	71.3	4.7	3.36	9.6	0.21
7.7	69.3	1.3	0.93	10.0	0.23
8.0	72.1	1.6	1.13	9.1	0.2
8.5	71.3	3.3	2.32	9.5	0.23
8.7	73.8	3.8	2.83	8.9	0.21
9.0	75.5	1.6	1.18	9.0	0.22
9.5	73.7	1.3	0.99	8.6	0.21
10	74.3	2.2	1.66	8.3	0.21
10.5	72.7	2.3	1.69	8.7	0.24
11.0	71.2	1.7	1.22	7.7	0.2
11.5	69.8	1.7	1.20	8.3	0.24
12.0	67.8	4.5	3.06	8.0	0.23
12.5	68.2	2.7	1.84	7.4	0.21
13.0	69.4	3.4	2.33	7.1	0.2
13.5	68.7	3.3	2.24	7.0	0.2

E (eV)	TCS (10^{-20} m^2)	Relative uncertainty (%)	Absolute uncertainty (± 10^{-20} m^2)	Δθ (deg)	ΔE (eV)
14.0	66.9	2.4	1.62	6.9	0.2
15.0	66	3.4	2.21	6.6	0.2
15.5	65.4	3.3	2.13	7.0	0.23
16.0	64.1	3.5	2.27	6.7	0.22
17.0	63	2.9	1.81	6.8	0.24
18.0	63.9	2.7	1.72	6.6	0.24
19.0	65.2	3.6	2.37	5.9	0.2
20.0	64.4	2.2	1.44	5.9	0.21
22.0	64	2.5	1.61	5.9	0.23
25.0	63.4	3.0	1.89	5.5	0.23
30.0	62	1.7	1.07	4.7	0.2
35.0	61	1.2	0.74	4.7	0.24
40.0	59.5	3.6	2.17	4.2	0.21
45.0	58.2	2.9	1.68	3.9	0.21
50.0	56.6	4.5	2.55	3.8	0.22
60.0	54.7	2.8	1.52	3.5	0.23
70.0	52.6	2.5	1.32	3.4	0.25
80.0	51.1	3.1	1.57	2.9	0.21
90.0	48.8	3.4	1.68	2.6	0.19
100	46.8	2.0	0.92	2.7	0.23
120	44.9	2.9	1.29	2.9	0.31
150	40.8	3.5	1.45	2.7	0.33
200	35.5	2.2	0.79	2.3	0.32
250	29.5	2.2	0.66	2.3	0.42

Table 3.5. Elastic, ionisation and summed excitation integral electron scattering cross sections, calculated within the IAM-SCAR+I method, and the rotational excitation cross sections derived from the Born approximation (all in Å^2 units) for scattering from nitrobenzene.

E(eV)	Elastic	Ionisation	Excitation	Rotational
1.0	116			775
1.5	96.9			540
2.0	87.6			417
3.0	79.8			291
4.0	75.6			224
5.0	72.2			183
7.0	68.9			135
10.0	66.6		0.1	97.7
15.0	61.3	0.5	3.3	67.5
20.0	55.2	3.6	5.9	52.1
30.0	47.6	10.4	6.0	35.8
40.0	42.8	13.4	5.1	27.5
50.0	39.5	14.5	4.6	22.4
70.0	34.4	15.1	4.1	16.4
100	30.0	14.6	3.7	11.8
150	25.0	13.1	3.3	8.1

E(eV)	Elastic	Ionisation	Excitation	Rotational
200	21.8	11.8	3.1	6.2
300	17.7	9.7	2.7	4.3
400	15.0	8.3	2.4	3.2
500	13.1	7.3	2.2	2.6
700	10.5	5.9	1.8	1.9
1000	8.2	4.5	1.5	1.4

Table 3.6. Experimental total electron scattering cross section data (in Å^2 units) for nitrobenzene in the energy range 100-1000 eV, together with their corresponding uncertainties and energy (ΔE) and angular ($\Delta\theta$) resolution limits.

E (eV)	TCS (10^{-20} m^2)	Relative uncertainty (%)	Absolute uncertainty (± 10^{-20} m^2)	$\Delta\theta$ (deg)	ΔE (eV)
100	50.6	7.0	3.5	0.16	0.5
120	44.3	7.0	3.1	0.16	0.5
150	38.0	7.0	2.7	0.16	0.5
200	33.2	7.0	2.3	0.16	0.5
250	31.7	7.0	2.2	0.16	0.5
300	28.2	7.0	2.0	0.16	0.5
400	23.2	7.0	1.6	0.16	0.5
500	20.2	7.0	1.4	0.16	0.5
600	18.7	7.0	1.3	0.16	0.5
700	16.4	7.0	1.1	0.16	0.5
800	15.1	7.0	1.1	0.16	0.5
900	13.2	7.5	1.0	0.16	0.5
1000	12.0	8.3	1.0	0.16	0.5

The present uncertainty limits have been derived by a root mean square quadratic combination of all the random uncertainty sources described in the MCEB experimental system (see ref. [18] for a comprehensive analysis of these uncertainty sources). As shown in Table 3.4, these limits range from 1 to 5%, depending on the incident energy. Possible systematic errors are described later with a fuller discussion for them being found in ref. [18]. It was also checked that the actual absorption length (L) corresponds to the geometrical length of the scattering chamber, by measuring the well-known electron scattering TCS for molecular nitrogen at selected energies, finding excellent agreement with the benchmark values available in the literature (see ref. [18] for details). The electron intensity count rate was always less than 10^3 s^{-1} (i.e. less than a 10^{-16} A electron current). Under these conditions no dependence of the measured TCS on the electron current was found, so ensuring that possible space charge effects are negligible in this experiment. In order to ensure that multiple scattering processes are absent under our working conditions, attenuation measurements were performed at relatively low nitrobenzene gas pressures (from 0 to less than 2 mTorr, depending on the incident energy). The incident energy was calibrated against the well-known resonance energy corresponding to the first peak in the N_2 TCS, which is largely due to the $\upsilon = 0 - 1$ vibrational excitation of N_2 [104]. As shown in ref. [18], the energy resolution of the incident electron beam (ΔE), derived from the transmitted electron profiles on the RPA, is typically within 100-200 meV. However, by biasing the RPA to the higher energies, to reduce the transmitted intensity by 25% of that for the incident electron intensity, an effective energy resolution better than 100 meV was customarily achieved [18]. Additionally, and as explained in ref. [18], due to the axial magnetic field conditions of the present MCEB experiment, the energy resolution and the incident energy (E) are linked to the angular resolution (Δθ) as follows:

$$\Delta\theta^{\circ} = arccos\sqrt{1 - \Delta E/E} \qquad (6)$$

Note that electrons elastically scattered within $\Delta\theta^{\circ}$ and $180^{\circ} - \Delta\theta^{\circ}$ are, for the MCP detector, indistinguishable from the unscattered electrons, and constitute the main systematic error source of the present measurements [18][105]. This effect always tends to lower the measured cross sections from their "true" value, but their magnitude can be estimated by integrating the calculated differential cross section (DCS) from 0° to $\Delta\theta^{\circ}$ and from $180^{\circ} - \Delta\theta^{\circ}$ to 180°. In the case of nitrobenzene, due to its permanent dipole moment, rotational excitations also contribute to this effect. In fact, this contribution is a common cause of confusion when comparing experimental with theoretical data and even between experimental results taken with different energy and angular resolutions. To illustrate this effect, our calculated differential elastic and rotational cross sections, are plotted together in Figure 3.10. As this figure shows, the angular distribution for rotational excitation is mainly concentrated around the forward direction, being 7 orders of magnitude higher than the elastic cross section at 0°. The acceptance angle of our MCEB apparatus, at 10 eV, is represented in this figure by a dashed line. By integrating the calculated elastic and rotational excitation DCS over the "missing angles", it was estimated that the contribution of elastic scattering to this effect is only 5.1 % of the measured TCS. On the other hand, the contribution of rotational excitation is of the same order of magnitude as the measured TCS value.

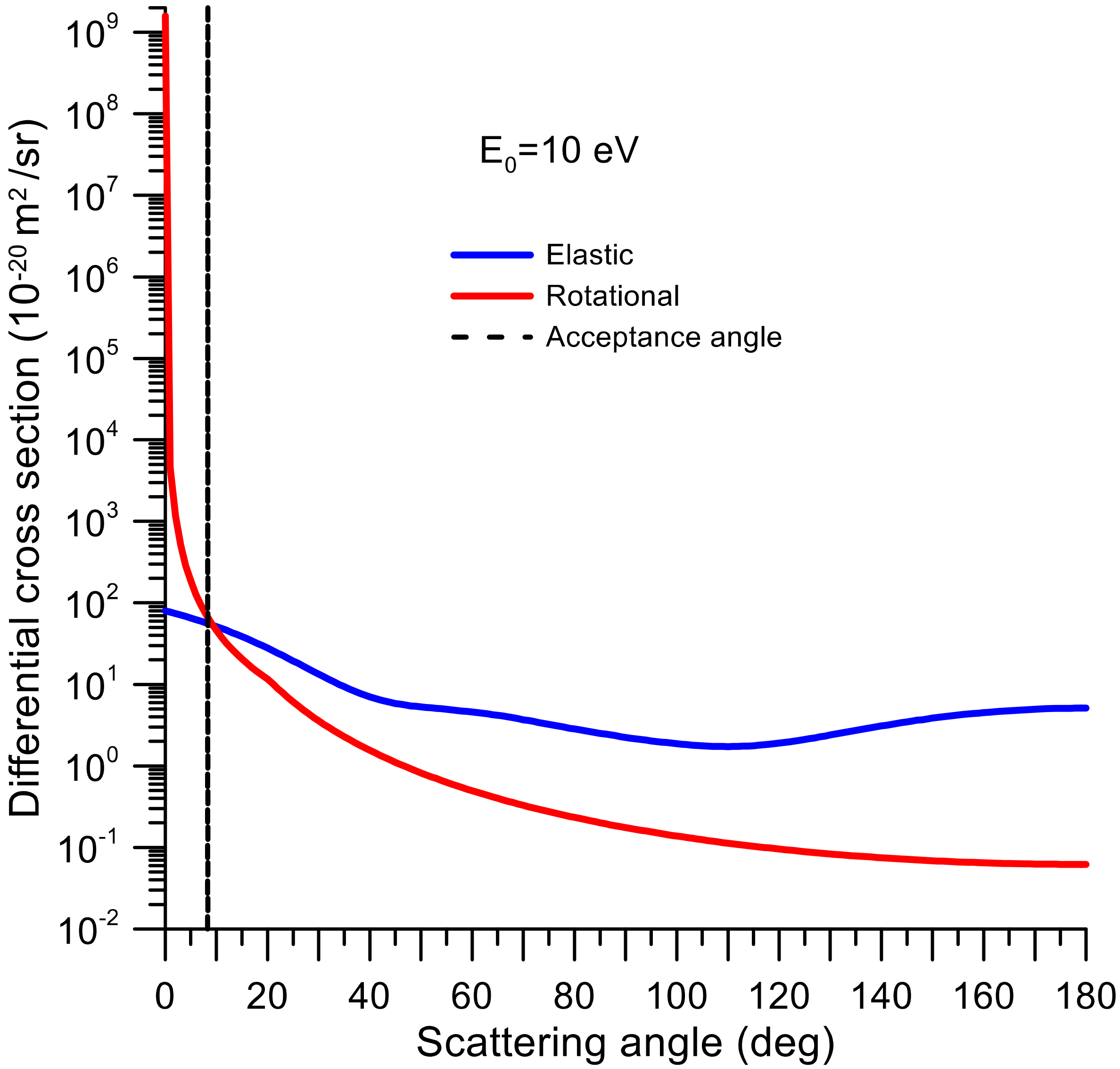

Figure 3.10. Differential cross sections (10^{-20} m^2/sr) for elastic scattering and rotational excitation in nitrobenzene at 10 eV incident electron energy.

The present IAM-SCAR+I integral elastic (IECS), summed electronic excitation (EECS), total ionisation (TICS) and the total (elastic + summed electronic excitation + ionisation) cross sections (TCS) are also plotted in Figure 3.11 for impact energies from 10 to 1000 eV. Note that these TCS values do not include the rotational excitation cross section independently calculated within the Born approximation. As mentioned earlier, this scattering channel is very important for strongly polar molecules, such as nitrobenzene, and its role in cross section measurements and calculations will be discussed forward. From a first inspection of Figure 3.11, it is possible to see that there is excellent agreement between the present experimental TCS data and our IAM-SCAR+I calculation above about 15 eV. However, as already noted, the effect of the elastic scattering into the detection angle and the rotational excitations out of this angle require a deeper analysis before comparing TCS data (as will be discussed later). Below 15 eV, down to 5 eV, the calculated TCS data (not shown) tend to be lower in magnitude than our experimental values reaching discrepancies of about 20 % at around 8 eV. This clearly indicates that our IAM-SCAR+I calculation is underestimating the strength of the electronic excitation cross sections from 5 to 15 eV. The TCSs measured by Lunt et al. [81][82] show a completely different behaviour than all the available theoretical and our experimental data. The possible impact of the dipole moment on these measurements will be addressed, but the significant discrepancy in the TCSs around 8-10 eV suggests that their absolute values may be affected by some yet unspecified systematic error.

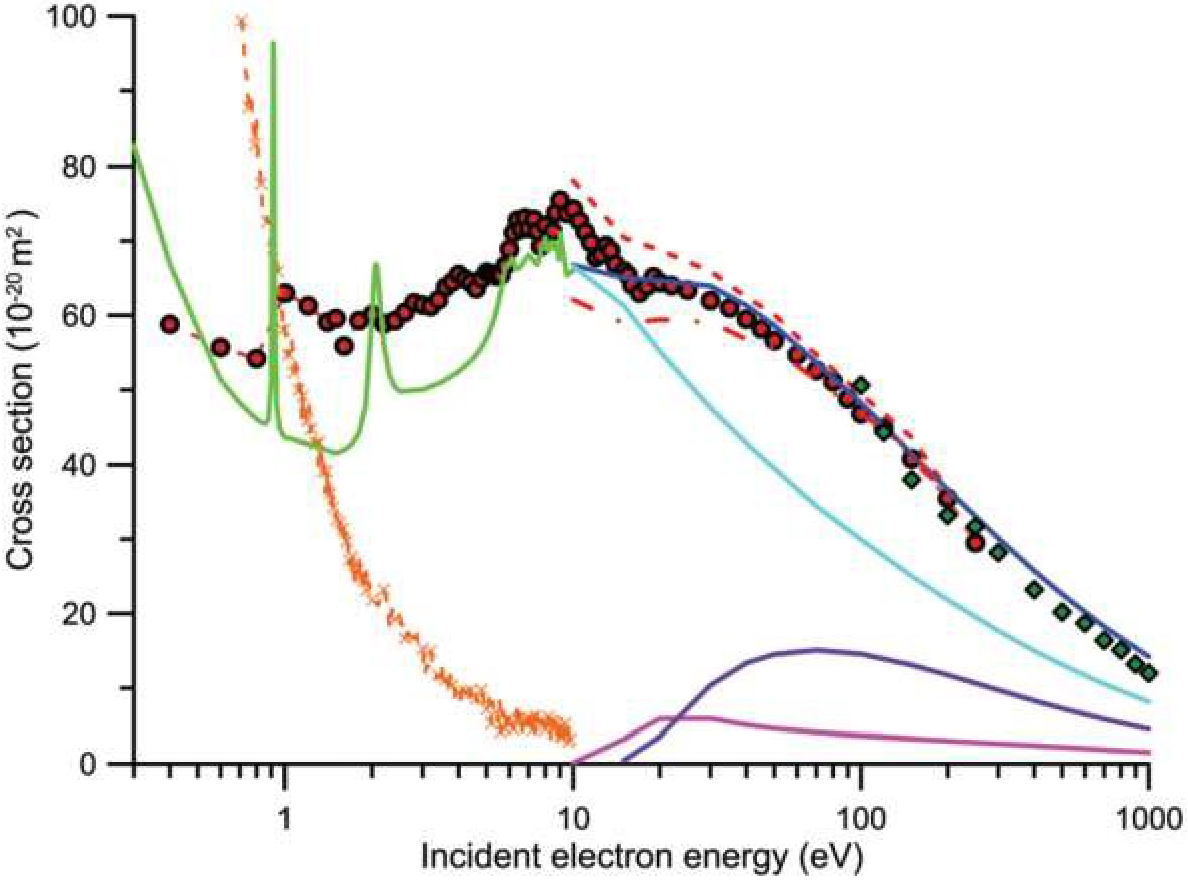

Figure 3.11. Integral and total electron scattering cross sections for nitrobenzene. Present measurements with the MCEB (●) and LTB (♦) experimental systems, respectively, are shown. Experimental data from Lunt et al. [81][82] (-×-) are also given. Present IAM-SCAR+I calculations: TCS not including rotational excitations (▬), integral elastic (▬), summed electronic excitation (▬) and ionisation (▬) cross sections are further plotted, as are the IECS from Maioli and Bettega [106] (▬). Corrections to the TCS: experimental results plus the contribution of elastic scattering within the “missing” angles (---), experimental values plus elastic scattering in the “missing” angles minus the rotational excitation contribution outside the effective detection angle (-●-).

Concerning the IECSs, the SMC data from Ref. [98] are also plotted in Figure 3.11 for comparison. Here, it is considered their SEP [98] calculation without their dipole Born correction (see Ref. [98] for details). Further note that this Born correction is equivalent to our aforementioned Dipole-Born rotational excitation cross section which corresponds to processes not detectable under the present experimental conditions and hence should not be included in this comparison. At 10 eV where both calculations apply the agreement between them is excellent. This in principle might suggest that by combining results from both methods, as far as elastic scattering is concerned, it could be possible to accurately cover the whole energy range considered here, from 0.4 to 1000 eV. However, below 4 eV where the IECS, apart from possible resonances, due to temporary electron attachment then decaying into vibrational modes of nitrobenzene and significantly increasing the usual magnitude of those vibrational ICS or leading to an enhanced dissociative electron attachment cross section, should be roughly equivalent to the TCS, the data calculated in ref. [98] are usually lower than the present experimental values reaching a maximum discrepancy, about 30 %, at around 1.5 eV. The origin of this discrepancy is not clear, but a possible reason based again on the effect of the dipole interaction and the forward elastic scattering will be presented during this discussion.

Another important aspect of low energy electron scattering is the possible presence of resonances, due to the temporary electron attachment to either the ground state (shape resonances) or excited states (core-excited or Feshbach resonances), of the nitrobenzene molecule. In addition, for highly polar molecules ($\mu > \sim 2D$) an electron can be bound by their dipolar electric field leading to a dipole-bound resonance [107]. Adams et al. [108], using a photoelectron imaging spectroscopy technique, observed the dipole-bound state of the nitromethane anion with a binding energy ~12 meV. This feature was distinguished from the vibrational structure of the valence state by the anisotropy induced by the dipole electric field. More recently, accurate photoelectron spectra of benzonitrile have been analysed by Gulania et al. [109] with a high-level electronic structure calculation of its anionic states. This investigation reveals the presence of a dipole-bound state, that provides the main mechanism to capture an incoming electron but leads to the formation of valence anions via non-adiabatic relaxation (see Ref. [109] and references therein). Interconnections between valence states of anions and dipole-bound states have also been identified in the opposite direction (bifurcation of the excited state wavepacket leading to the formation of a non-valence state) for a common anionic chromophore [110], and the stability of such orbitals in the presence of perturbing molecules has also been studied by the same group [111]. Very recently, Anstöter et al. [112] showed that the observed emission peaks from the vibrational structure of the nitrobenzene anion can be correlated with an autodetachment mechanism via dipole-bound state formation. In all these cases, dipole-bound states are formed at very low energy, below the lower energy limit of the present experimental study (0.4 eV). Modelli and Venuti [39] combined electron transmission spectroscopy (ETS) measurements with ab initio calculations to analyse the electron attachment to nitrobenzene in the energy range 0–6 eV. By comparing the experimental results with the calculation of the vertical electron affinity (0.37 eV) they concluded that the first anion state of nitrobenzene is stable and therefore not observed in ETS. This conclusion is supported by the complementary parent anion detection using mass spectrometry (see Ref. [39] for details) showing an intense peak at 0 eV and a much weaker signal at 0.4 eV. In concordance with this result. Maioli and Bettega calculation showed the formation of the anionic bound state ($\pi_{bound}{}^{*}(b_1)$) at 0.39 eV using the configuration space of the B_1 symmetry. In the energy range considered here, the first resonance found by Modelli et al. [39], in their electron transmission spectra, was placed at 0.55 eV and was associated with the non-interacting ring $\pi^{*}(a_2)$ component of the benzene $\pi^{*}(e_{2u})$ lowest unoccupied molecular orbital (LUMO), inductively stabilised by the electron-withdrawing nitro group. They related this resonance with the formation of the parent anion, but probably due to the energy resolution limitations of the present measurements (0.2 eV) it was not observed such narrow feature in the TCS. Note that the SEP calculation of Maioli and Bettega [98] placed this resonance at 0.92 eV. Pelc et al. [41] observed the formation of the parent anion at 0 eV, but it should be admitted that the energy resolution of the present study (~ ± 0.2 eV) is not good enough to provide any additional information about this parent anion formation. Our first feature in the measured TCS is observed at around 1.0-1.5 eV. This broad peak is compatible with those observed in the mass spectra of Modelli et al. [39] (0.7, 1.25 eV), Pelc. et al. [41] (0.7, 1.4 eV), Compton et al. [36] (1.3 eV), Jäger and Henglein [38] (1.5 eV) and is connected with the formation of the NO_2^- anion. It is assigned to the $\pi^{*}(b_1)$ resonance. The SEP calculation [98] found this resonance at 2.07 eV, confirming the usual shift to higher energies presented by this calculation with respect to experimental results (see Ref. [98] for a comparative discussion between theoretical and experimental resonances in nitrobenzene and their correlation with those of benzene on the basis of their respective molecular orbitals). Between 2.2 and 3.3 eV an increase in the TCS at around 2.8 eV is distinguishable. Although the origin of this feature is not clear, it is worth mentioning that similar structures at those energies were experimentally observed for benzene [5] and pyridine [10][113] being related to the vibrational excitation of the ground state [10][5]. The next feature clearly shown by our TCS is a local maximum at 4.0±0.2 eV, which can be related to those found in Refs. [39] and [41] at 3.8 eV. Modelli et al. [39] assigned this peak to a core excited resonance, that according to the mass spectra from ref. [41] may lead to the formation of the NO_2^- negative fragment. This feature was also observed by Lunt et al. [81][82] at around 3.75 eV, and was associated by them with the dissociative electron attachment channel. The resonance at 4.69 eV, found by Modelli et al. [39], is assigned to the highest-lying empty $\pi^{*}(b_1)$ state of nitrobenzene with a net effect of stabilisation. However, the mass spectra from Pelc et al. [41] and Jäger and Henglein [38] show a prominent signal at 4.8 and 5 eV, respectively, which are assigned to the formation of the O^- anion. The local maximum in the TCS observed at 5.0±0.2 eV confirms these observations. Our experimental data show additional broad structures at around 6.8 and 9 eV, which can be attributed to highly excited states just below the threshold ionisation energy (9.9 eV) [114].

Regarding the results obtained with the LTB system, due to the good angular resolution of the LTB apparatus (fixed acceptance angle of 0.16 deg.), the contribution of elastic scattering to the "missing" angle effect, as estimated with our calculated elastic DCS, is less than 1% for the entire energy range (100-1000 eV). Due to the significant dipole moment of nitrobenzene, some contribution to this effect from rotational excitation may, however, be expected. By using our calculated rotational excitation DCS, integrated over the acceptance angle of the detector (0-0.16°), it was estimated a contribution to the TCS between 10.7% to 6.2% for energies from 100 to 1000 eV, respectively. As already discussed, this is a systematic error that should be added to the experimental results, when comparing with theoretical calculations including Dipole-Born corrections. If a comparison is to be made between different experimental results, the theoretical DCS should then be integrated over their respective angular acceptances to obtain comparable data. Under the conditions of the LTB apparatus, the contribution of rotational excitation from the acceptance angle, which should be subtracted from the measured TCS if no rotational excitation is being considered in the comparison to the IAM-SCAR+I TCS, is less than 1% and therefore negligible, in comparison with the other uncertainty sources.

Finally it can be observed that the present LTB measurements are in very good agreement (see Figure 3.11), within the combined uncertainty limits, with both the MCEB experimental data and our IAM-SCAR+I calculations to within the overlapping energy ranges.

3.2.3. Pyridine

Two recent TCS measurements for pyridine have been published [10][113] using two different techniques, namely with and without magnetic confinement. The corresponding results are shown in Figure 3.12. Above 10 eV there is very good agreement between these experimental data and also with and our IAM-SCAR calculation [8]. However, below 10 eV the TCS data from Ref. [113] tends to be higher in magnitude, certainly well outside the stated uncertainties on each measurement, than ours. This apparent discrepancy is due to the different angular resolution used in each experiment. As discussed in Ref. [115], the angular resolution of our magnetically confined apparatus is linked to its energy resolution, which becomes poorer for lower energies, so causing the measurement to underestimate the actual TCS value. On the other hand the angular resolution used in the transmission-beam experiment of Ref. [113] is a fixed value, given by the geometrical acceptance angle of the detector (~5 degrees). In these circumstances, the systematic correction due to elastically scattered electrons into these “missing” angles ($\Delta\sigma_{el}$) is negligible for the experimental data of Ref. [116] but not for those of Ref. [10]. Nevertheless, the latter can be corrected for by calculating the contribution of elastic scattering into the acceptance angle of the detector by using our IAM-SCAR [8] calculated elastic DCSs. As can be seen in Figure 3.12, the experimental data of Ref [10], corrected by accounting for the elastic scattering into the missing angle contribution (TCS [10] + $\Delta\sigma_{el}$), now agrees very well with those of Ref. [113] from 5 to 100 eV. Below 5 eV, however, the results from Ref. [113] again tend to be higher in magnitude than those from Ref. [10] once corrected for the "missing angle" effect. As stated above, the angular resolution used in Ref. [113] is good enough to discriminate against the contribution of electrons elastically scattered into the "missing angles", but not totally for that of the rotational excitations. Pyridine has a significant permanent dipole moment (2.2 D [117]), thus rotational excitation cross sections, which are strongly peaked in the forward scattering direction (see Figure 3 from Ref. [10]), are dominant at the lower impact energies. As explained in Ref. [8], differential and integral rotational excitation cross sections can be reasonably easily calculated in the framework of the Born approximation. If it is included the contribution of scattered electrons into the "missing angles" after the rotational excitation processes, in the correction of the experimental TCS from Ref. [10], it is obtained the blue dot-dashed line also shown in Figure 3.12.

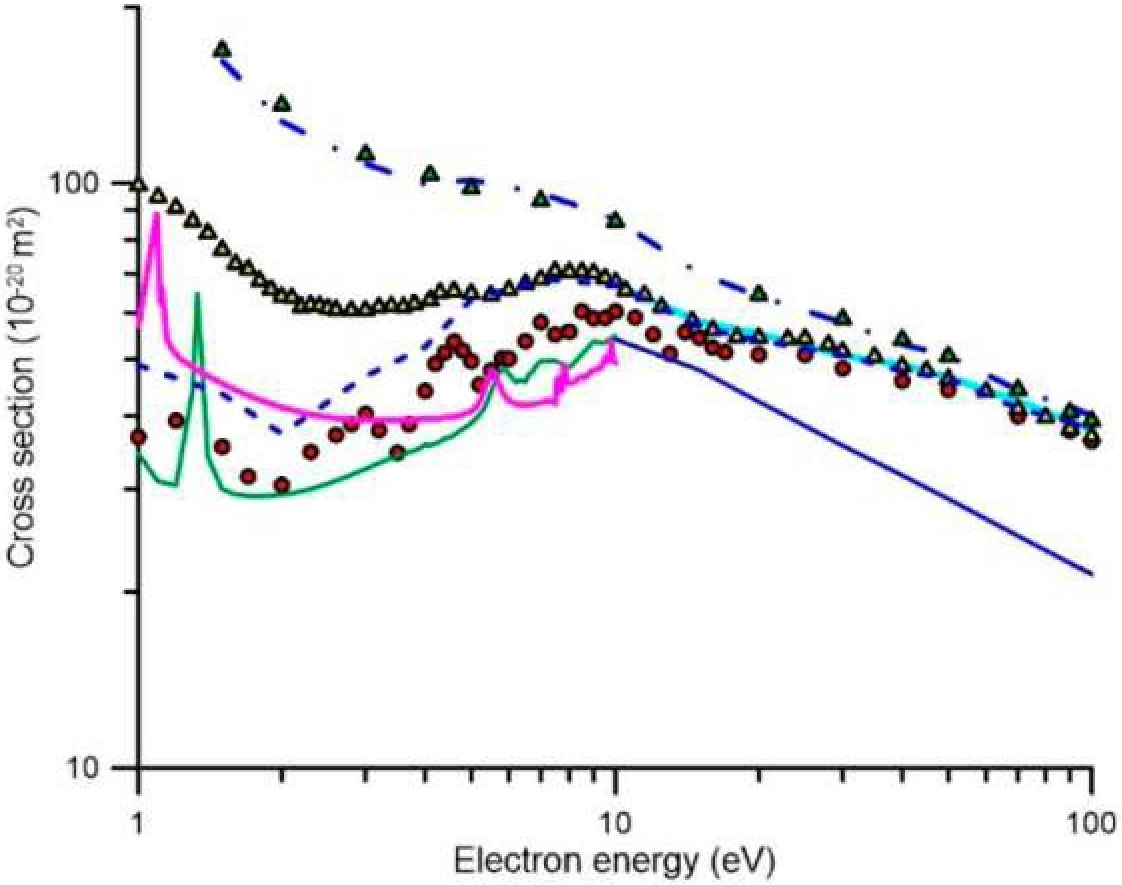

Figure 3.12. Total electron scattering and integral elastic cross sections for electron collisions with pyridine: present experimental data [10] (●); experimental data from Ref. [113] (▲); experimental data from Ref. [113] including the correction for rotational excitations into the acceptance angle of the detector ("missing angles") (▲); integral elastic cross section calculated with the SMC method (━); integral elastic cross section calculated with the R-matrix method (━); integral elastic cross section calculated with the IAM-SCAR method (━); our experimental data [10] including the correction for electron elastically scattered into the "missing angles" as calculated with the IAM-SCAR differential elastic cross sections (---); our experimental data [10] including both the corrections for elastic and rotational excitation scattered electrons into the "missing angles" (-•-•-).

As may be seen in Figure 3.12, these latest corrected values show the same shape as that of the experimental data from Ref. [113] but tend to be higher in magnitude for the lower energies. This result suggests that in spite of the relatively good angular resolution used in the experiment of Ref. [113], it is not sufficient to fully resolve the electrons rotationally scattered in the forward direction. Note that these electrons are also not energetically resolved, given the average excitation energy for rotational processes in pyridine is about 1 meV at 300 K. In order to test this suggestion, it was added to the experimental data of Ref. [113] the contribution of the rotational excitations within the 5° acceptance angle of their detector. The result of this correction is also shown in Figure 3.12, as filled green triangles, where the now excellent agreement with the elastically and rotationally corrected data from Ref. [10] can be seen and considered as a confirmation for the consistency of the theoretical and experimental data involved in this analysis. As pointed out by Fabrikant [29], rotational excitation is a common source of uncertainty both for theoretical and experimental TCS determinations. A discussion about the inherent difficulties in comparing theoretical and experimental data for polar molecules, can also be found in Ref. [14]. Taking into account all these considerations, the conclusion is that accurate reference values for the total electron scattering cross sections (not including rotational excitations) are the experimental data from Ref. [10] once corrected for the elastic scattering contribution to the “missing angles” (i.e. for the acceptance angle of the detector at each incident electron energy). These values, as noted earlier, are supported by the most recent experimental data of Ref. [113] for energies above 5 eV and the IAM-SCAR calculation [8] for energies above 10 eV. Considering the level of agreement between these results, it can be determined a total uncertainty limit for the TCS of about 10% for energies above 5 eV. Below 5 eV, due to uncertainties introduced by the rotational excitations, it should be incremented this limit up to 20%.

3.3. Double differential ionization cross sections

3.3.1. Benzene

In Table 3.7, it is presented the absolute values of DDCS for electron scattering with benzene at impact energy of 90 eV for three different transferred electron energies (ΔE), 30, 40 and 50 eV. For these incident energies two different conditions were analysed, i.e. two different extraction potentials were applied during the measurements, which results in more data collected and a wide angular range covered. Furthermore, the range covered for each transferred energy has been from 7° to 99° for ΔE=30eV, 4° to 102° for ΔE=40eV and 7° to 117° for ΔE=50eV. Important to note that despite the effort to record as many angles as possible, some intermediate angular ranges are missing. Nevertheless, the results obtained bring us a general overview of the scattering problem.

Table 3.7. Absolute DDCS and its corresponding errors (in units of 10^{-22} m^2 sr^{-1}) for elastic electron scattering with benzene at impact energy of 90 eV for three different transferred electron energies.

	30 eV		40 eV		50 eV	
Angle (deg)	DDCS	δ_{DDCS}	DDCS	δ_{DDCS}	DDCS	δ_{DDCS}
4			11,91	0,35		
7	21,93	0,23	6,14	0,11	3,55	0,08
10	16,47	0,16	5,13	0,09	2,78	0,06
13	11,88	0,12	3,86	0,07	1,88	0,05
16	8,14	0,09	2,62	0,05	1,12	0,04
19	5,34	0,07	2,00	0,05	0,95	0,03
22	3,83	0,06	1,61	0,04	0,79	0,03
25	2,94	0,05	1,31	0,03	0,70	0,02
28			1,10	0,03	0,62	0,02
31			1,07	0,02	0,54	0,02
34					0,46	0,02
37					0,42	0,02
40					0,36	0,01
43			0,55	0,02	0,34	0,01
46			0,47	0,02	0,35	0,01
49			0,35	0,02		
52	0,46	0,03	0,40	0,02		
55	0,33	0,02			0,39	0,02
58			0,48	0,03	0,29	0,01
75					0,39	0,02
78			0,54	0,02		
81			0,68	0,04	0,34	0,02
96	0,23	0,03	0,39	0,02	0,26	0,01
99	0,22	0,02				
102			0,36	0,02	0,22	0,01
117					0,29	0,02

The behaviour of DDCS as a function of the transferred energy can be observed in Figure 3.13, where the data are plotted. As observed, below 50° the value of DDCS increases rapidly for lower transferred energies while smoother for higher transferred energies. Instead, around 50°, the DDCS for the three energies transferred converge and above 50° an isotropic behaviour is found. Therefore, the electron is more likely scattered in the forward direction for angles above 50° independently of the transferred energy.

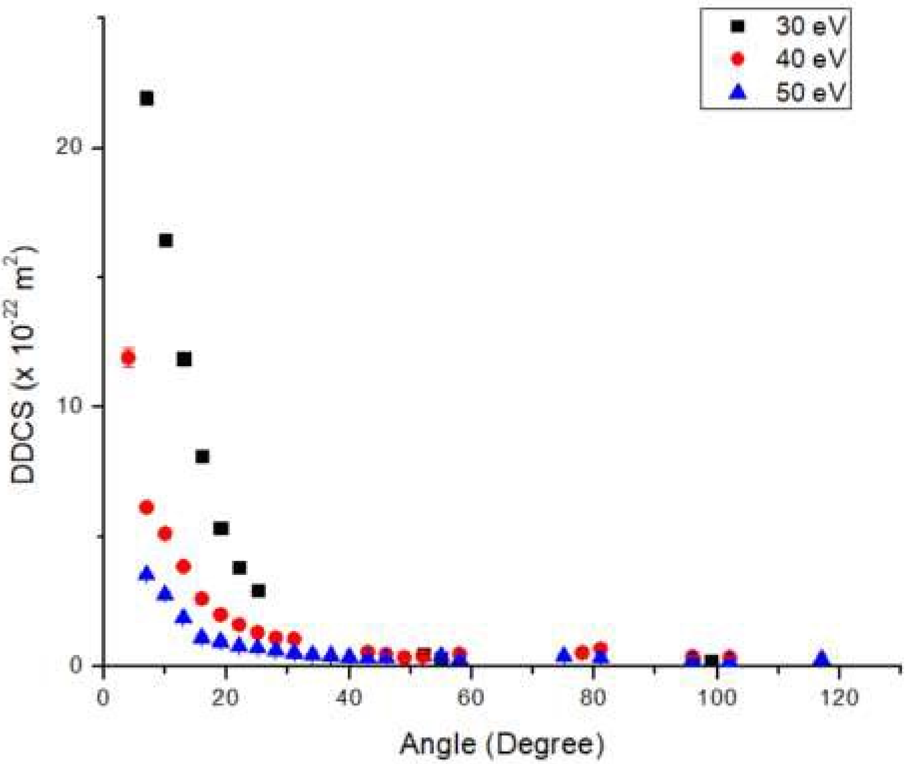

Figure 3.13. Absolute values of DDCS for impact energy of 90 eV with three different transferred energies: 30 eV (■), 40 eV (●) and 50 eV (▲).

3.3.2. Pyridine

The DCS to ionize pyridine has been measured, with a reaction microscope, for 90 eV electron impact energy and different energy loss values, namely 50, 40 and 30 eV. This important experimental apparatus has also been recently used to investigate the behaviour of different biomolecules [20][21]. Fundamentally, it allows for measurements in coincidence, to provide information about the angular and energy distribution of all the particles involved in the reaction (scattered electron, secondary ejected electron and recoil ion), as well as the fragmentation induced to the target species. However, for the modelling procedure presented later, the focus will only be on the angular and energy distribution of the scattered electrons and the production of the most representative ions. Specifically, this angular distribution was measured for the fixed values (30, 40 and 50 eV) of the energy transferred from the incident electron to the target molecule, and for the most probable ionization channels at the present incident energy (90 eV) which were found to be for parent ion generation ($C_5H_5N^+$) and the H-loss fragment ion production ($C_5H_4N^+$). The results of these particular measurements are shown in Figures 3.14 and 3.15, with their statistical uncertainty limits also being shown.

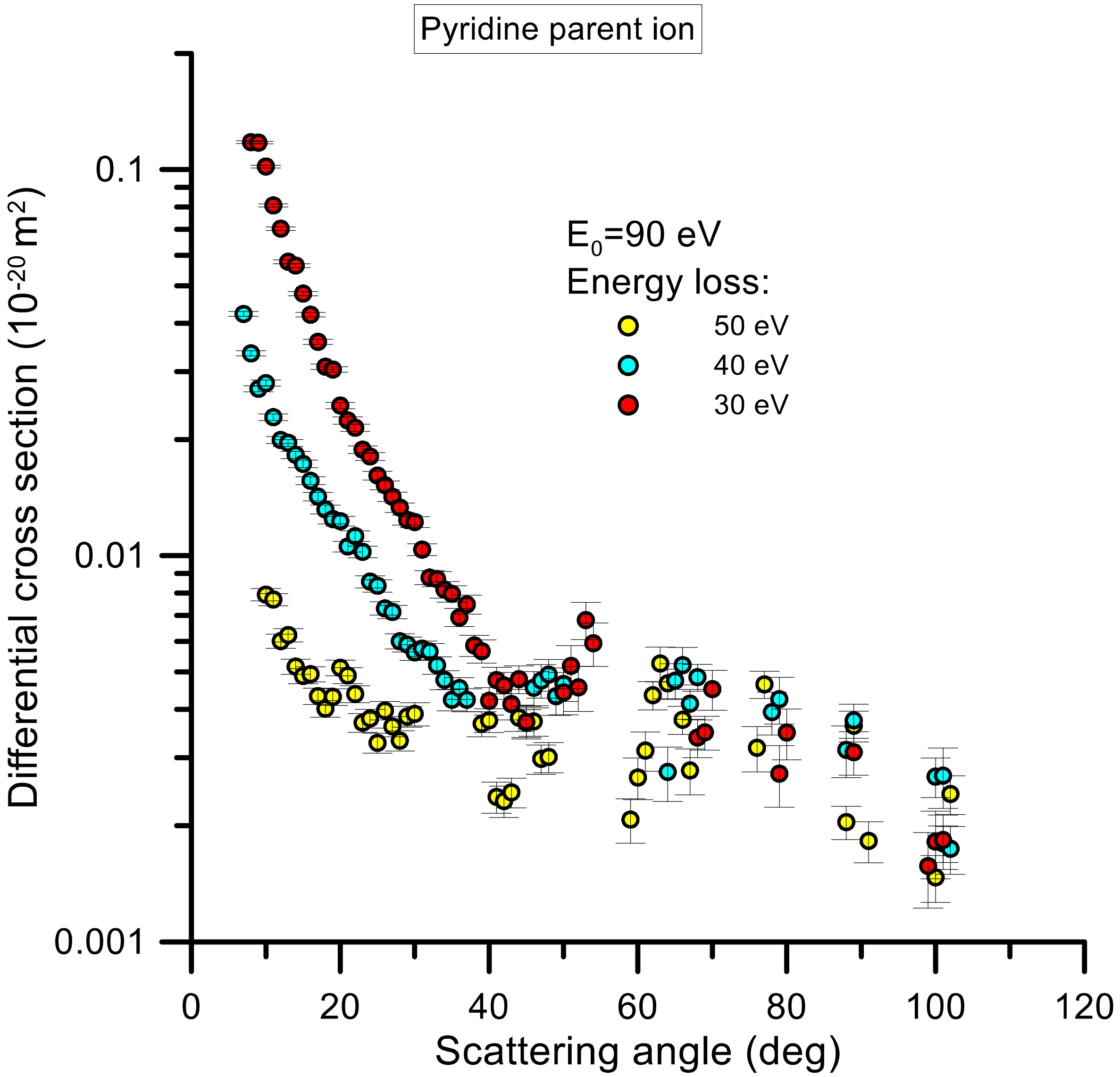

Figure 3.14. Double differential cross section for the production of the pyridine parent ion ($C_5H_5N^+$) under 90 eV electron impact ionization where the scattered electron has different energy loss values (30, 40 and 50 eV).

The absolute scale assigned to the measured double differential cross sections (DDCS) has been derived from the normalisation of the observed ionization relative to that of He atoms, where the He ionization theoretical values were calculated by Ren et al. [118] by means of the Convergent Close Coupling method. For a light atom like He the good accuracy of this method allows one to use the calculated scattering cross sections as reference values to scale the scattering data from other species. Due to the required determination of the relative target densities of He and pyridine which was done using the total ion yields and total ionization cross sections, it was conservatively considered a 20% uncertainty associated with those absolute values. Note that this uncertainty does not actually affect upon the main goal of this study, where the relative angular distribution as a function of the energy loss will be used to check the inelastic probability distribution functions normally employed in our modelling of electron transport [116].

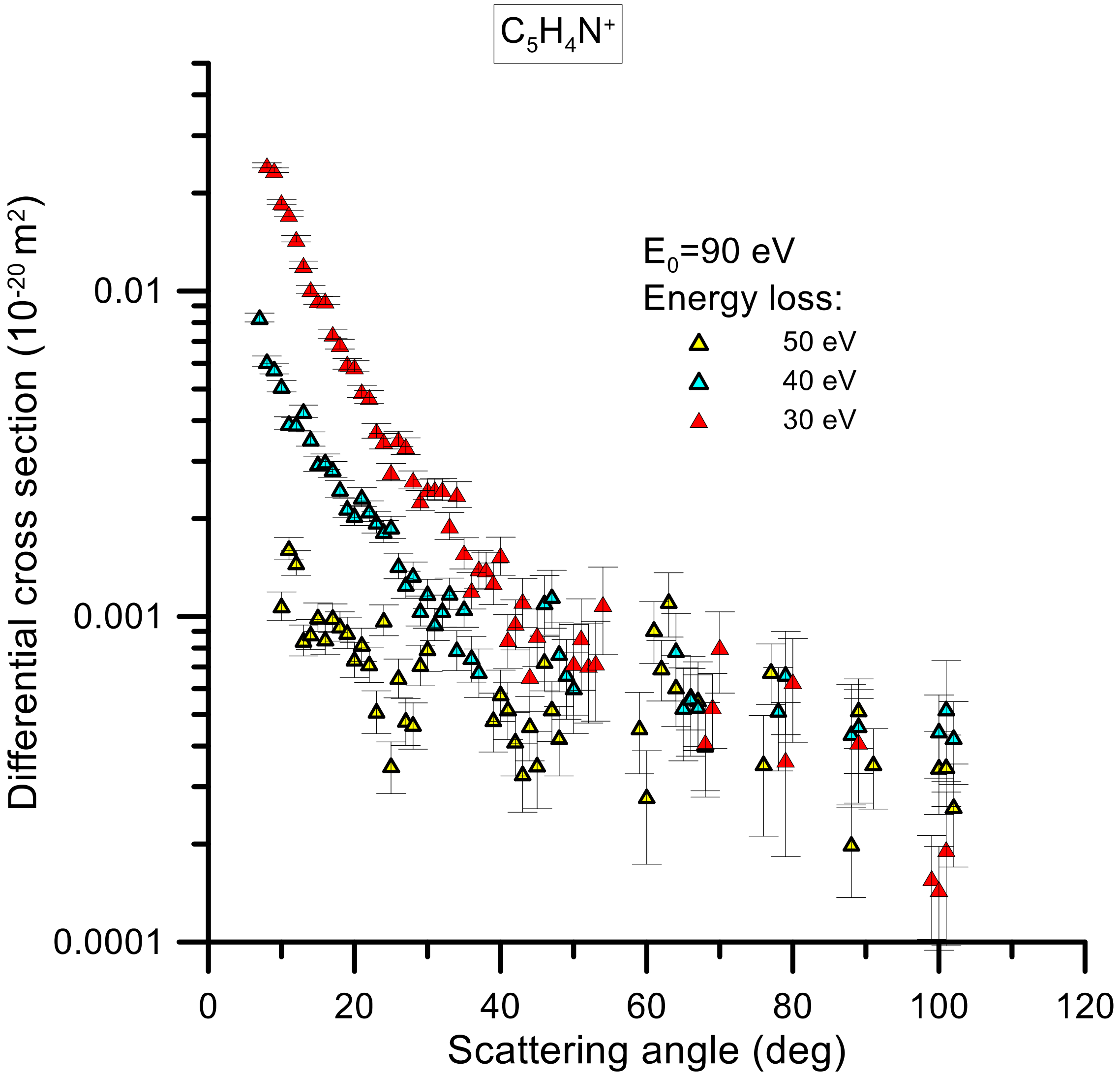

Figure 3.15. Double differential cross section for the production of the pyridine H-loss ion ($C_5H_4N^+$), under 90 eV electron impact ionization where the scattered electron has different energy loss values (30, 40 and 50 eV).

As can be seen in Figures 3.14 and 3.15, the DCS as a function of the scattering angle for the ion species considered here, are very similar in shape regardless of the energy loss probed, although the cross sections for producing the parent ion are higher in magnitude than those for the H-loss ion fragment by a factor of ~5. For both ions, the angular distributions tend to be flat for scattering angles above 40° and for increasing energy loss values. Below 40°, however, the differential cross sections increase exponentially when the scattering angle tends to zero degrees, also showing an increment in this slope as the energy loss decreases.

3.4. Triple differential cross sections

3.4.1. Benzene

In TDCS, both the scattered and the ejected electrons have been analysed. θ_1 and E_1 are the angle and the energy of the scattered electron, and θ_2 and E_2 are the angle and the energy of the ejected electron, respectively. In Figure 3.16 it is showed the obtained relative results for E_0 = 90 eV with four different conditions. Despite looking at relative results, different features can be observed, which can be correlated with structures related to molecular orbitals, where is more probable to extract the electron.

As observed in Figure 3.16, the maximums values are situated for both lower and higher angles, and a broad structure centred around 180° can be found. One possible explanation for this to happen is that the ejected electron has a higher probability to move along the direction of the incident beam and is less probable to move on the opposite direction of the beam. In addition, comparing the intensity as a function of the scattered electron angle (θ_1), it can be observed that as θ_1 increases, the intensity is reduced in more than half. As mentioned above, some structures can be observed, for E_2=5 eV, two peaks around to θ_2=25° and θ_2=75° are distinguishable both for θ_1=-10° and θ_1=-20°. As for for E_2=10 eV, a peak is observed close to θ_2=50° for both scattered electron angles presented. Several structures can be observed in every plot for angles above 180°, but unfortunately, they are not clearly distinguishable, particularly in the case of E_2=5 eV. Important to note that there is a small peak close to θ_2=135°, which is common for every case presented.

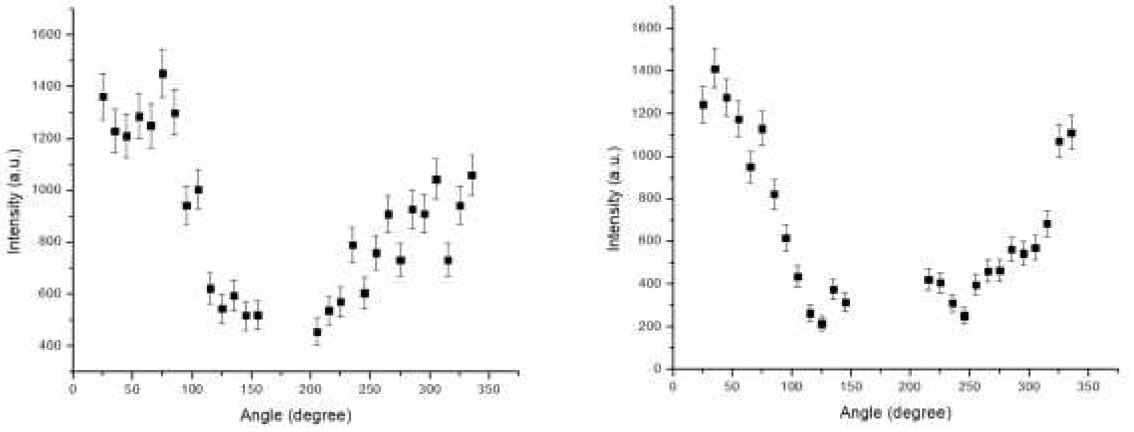

(a) θ_1=-10°, E_2=5 eV

(b) θ_1=-10°, E_2=10 eV

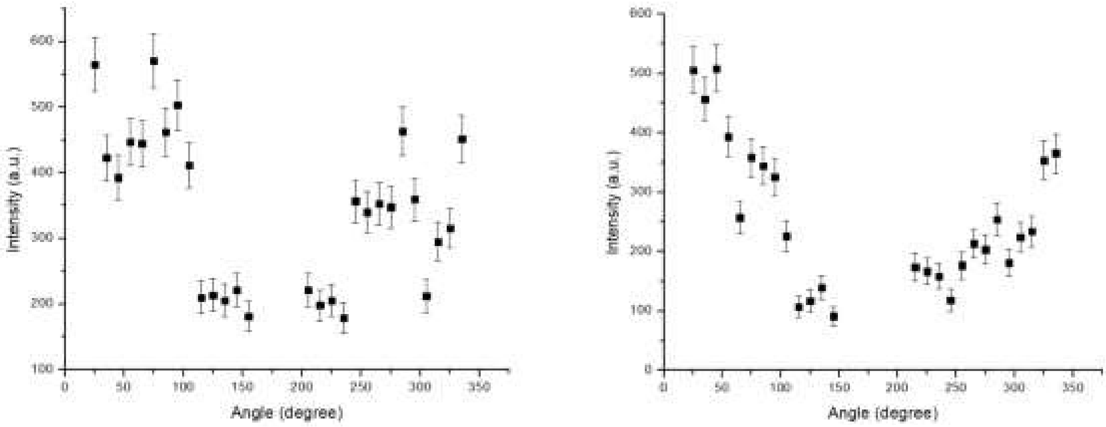

(c) θ₁=-20°, E2=5 eV

(d) θ₁=-20°, E₂=10 eV

Figure 3.16. Relative TDCS for elastic electron scattering with benzene at impact energy of 90 eV as a function of the ejected electron emission angle θ_2 and the ejected electron energy E_2.

3.5. Integral elastic scattering cross sections

3.5.1. Pyridine

A detailed analysis of the elastic electron scattering cross sections for pyridine can be found in Ref. [8]. Briefly, above 10 eV the IAM-SCAR calculation provides accurate integral elastic cross section (IECS) values to within 10 %. Below this energy the two available “ab initio” calculations, using the R-matrix [8] and the Schwinger multichannel (SMC) with pseudopotentials [119] methods, respectively, are plotted in Figure 3.12. As can be seen in this figure they agree reasonably from 5 to 10 eV and overlap well with the IAM-SCAR calculation at 10 eV. However, below 5 eV, they diverge for decreasing energies reaching a maximum discrepancy of about 50% around 1 eV. The origin of this discrepancy may be in a poor description of the background scattering in the SMC calculations, since the main goal of that study was to describe the three π* resonances. However, note that the SMC calculation at around 1.5 eV gives IECS values much lower (about 40%) than the corrected TCS. This is in contradiction with the fact that at these energies the IECS equals the TCS, as the electron attachment and vibrational excitation channels are not significant at such an energy. The elastic R-matrix calculation gives values that are slightly higher in magnitude than the corrected TCS (12-17 %), but in quite good agreement considering the uncertainty limits (about 15%) for these impact energies. Therefore, it is considered the R-matrix calculation as the most reliable option for energies below 5 eV, as far as the IECS values are concerned. The most suitable IECS, for the whole energy range considered here (0.1-100 eV), are shown in Table 3.8 and plotted in Figure 3.17. Note that the R-matrix data published in Ref. [8] has been now recalculated using the UKRmol + suite [120], both at the DCS and ICS level, including more incident energy values as required for application of the electron transport models. The IECS from Ref. [119], shown in Figure 3.12, were calculated with the aforementioned SMC method with pseudopotentials, and at the static-exchange-polarisation (SEP) level (see Ref. [119] for details). As noted above, the origin of its discrepancy with the R-matrix and the experimental TCS data is due a poor description of the background scattering, but for completeness the SMC data was recalculated by extending the impact energy range up to 20 eV. These new results are shown in Table 3.9, and they will be also used in the electron transport simulation to investigate the influence of elastic scattering in the simulated output.

Table 3.8. Complete set of integral electron scattering cross sections for pyridine, in the energy range (0.1-100 eV), in SI units (10^{-20} m^2).

E(eV)	TCS [24] $+\Delta\sigma_{el}$	IECS R-matrix [8]	Electron attachment	Electronic excitation	Vibrational excitation	Ionization	Rotational excitation
0.110		423.0					1374
0.135		340.0					1145
0.160		284.1					984.4
0.185		244.1					864.9
0.210		214.1					772.5
0.235		190.8					698.8
0.260		172.3					638.6
0.285		157.2					588.5
0.310		144.8					546.0
0.335		134.3					509.5
0.360		125.3					477.8
0.385		117.6					450.1
0.410		110.9					425.6
0.435		105.1					403.7
0.460		99.89					384.1
0.485		95.27					366.4
0.510		91.14					350.3
0.535		87.42					335.7
0.560		84.05					322.3
0.585		80.99					310.0
0.610		78.18					298.7
0.635		75.61					288.2
0.660		73.23					278.4
0.685		71.06					269.3
0.710		69.23	< 0.1				260.9
0.735		68.64	0.1459				252.9
0.760		67.39	18.25				245.5
0.785		66.19	29.47				238.5
0.810		65.01	7.442				232.0
0.835		63.87	3.107				225.8
0.860		62.77	1.479				219.9

E(eV)	TCS [24] +$\Delta\sigma_{el}$	IECS R-matrix [8]	Electron attachment	Electronic excitation	Vibrational excitation	Ionization	Rotational excitation
0.885		61.70	0.6735				214.4
0.910		60.67	0.2315				209.1
0.935		59.66	< 0.1				204.1
0.960		58.61					199.4
0.985		57.72					194.9
1.00	46.54	57.21					192.2
1.01		56.88	0.1512				190.6
1.03		56.02	0.6431				186.4
1.06		55.20	1.899				182.5
1.08		54.40	6.533				178.8
1.11		53.65	36.67				175.2
1.13		52.93	9.549				171.7
1.16		52.25	1.578				168.4
1.18		51.59	0.184				165.3
1.20	47.55	51.09	< 0.1				163.4
1.50	42.26	45.51					133.9
1.70	37.66	43.42					119.8
2.00	35.8	41.37			< 0.1		103.6
2.30	39.44	40.23			1.73		91.51
2.60	41.37	39.64			3.26		82.04
2.80	42.7	39.44			4.71		76.80
3.00	44.04	39.33			2.05		72.22
3.20	41.36	39.31			< 0.1		68.18
3.50	37.89	39.34		< 0.1			62.95
3.70	41.8	39.40		2.4			59.91
4.00	47.04	39.51		7.53			55.89
4.20	51.92	39.60		12.32			53.51
4.40	54	39.73		14.27			51.33
4.60	56.2	39.90		16.3			49.34
4.80	54.21	40.18		14.03			47.50
5.00	52.02	40.77		11.25			45.81
5.20	47.54	42.28		5.26			44.23
5.50	50.04	48.05		1.99			42.08
5.80	52.33	44.20		8.13			40.13
6.00	52.17	42.52		9.65			38.94
6.50	55.63	41.80		13.83			36.26
7.00	59.61	42.21		17.4			33.94
7.50	56.8	41.79		15.01			31.91
8.00	57.31	45.49		11.82			30.13
8.50	61.93	47.75		14.18			28.55
9.00	60.15	47.94		12.21			27.13
9.50	60.19	51.54		8.65			25.85
10.0	61.63	49.32		12.27		< 0.1	24.70
12.0	57.8	45.19		12.43		0.18	20.99
15.0	56.76	40.60		14.83		1.329	17.21

E(eV)	TCS [24] +$\Delta\sigma_{el}$	IECS R-matrix [8]	Electron attachment	Electronic excitation	Vibrational excitation	Ionization	Rotational excitation
20.0	53.84	42.28		7.548		4.012	13.32
30.0	50.73	35.56		6.392		8.778	9.277
40.0	47.74	31.64		5.130		10.97	7.179
50.0	46.36	28.84		5.710		11.81	5.884
70.0	41.15	24.92				12.27	4.360
90.0	39.09	22.40				12.59	3.485
100	37.64	21.42				12.26	3.173

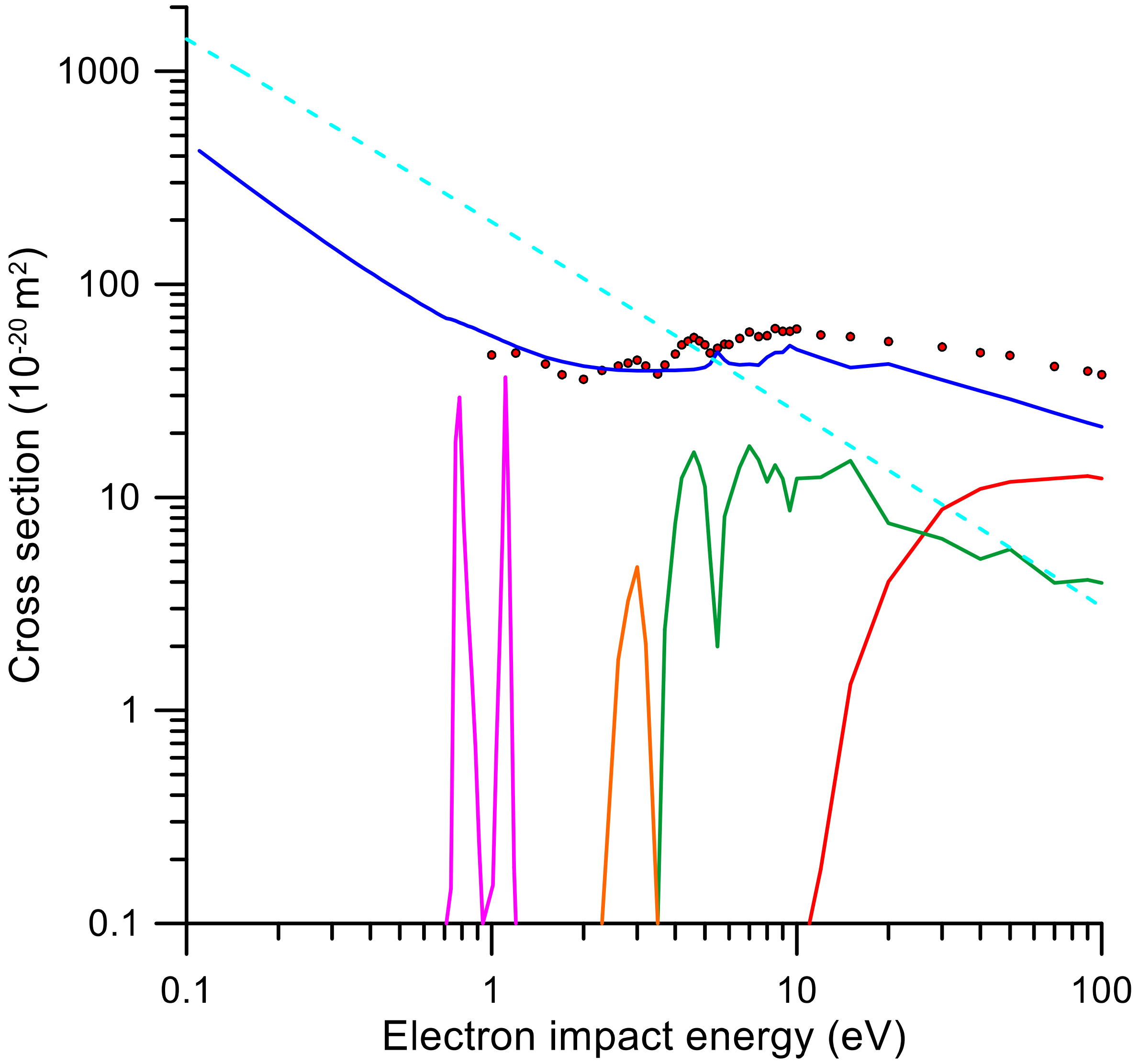

Figure 3.17. Complete set of integral electron scattering cross sections for modelling electron transport in pyridine in the energy range (0-100 eV): ●, experimental data [10] including electrons elastically scattered into the “missing” angles (see text for details); ▬, IECS based on the present R-matrix and IAM-SCAR calculations; ▬, ionization; ▬ , electronic excitation; ▬, vibrational excitation; ▬, electron attachment; ---, dipole-Born rotational excitation.

Table 3.9. Integral elastic electron scattering cross sections for pyridine in the energy range 0.1-20 eV, in SI units (10^{-20} m^2), as calculated with the SMC method.

E (eV)	IECS (10^{-20} m^2)	E (eV)	IECS (10^{-20} m^2)
0.1	172.4	4.1	35.58
0.2	97.4	4.2	35.86
0.3	65.32	4.3	36.14
0.4	50.62	4.4	36.62
0.5	42.81	4.5	36.73
0.6	37.78	4.6	37.05
0.7	34.31	4.7	37.58
0.8	32.47	4.8	37.96
0.9	81.96	4.9	38.38
1	34.43	5	38.87
1.1	30.87	5.1	39.47
1.2	30.44	5.2	40.20
1.3	44.29	5.3	41.04
1.33	64.70	5.4	42.30
1.4	34.02	5.5	43.94
1.5	29.95	5.6	45.72
1.6	29.33	5.7	47.19
1.7	29.17	5.8	47.82
1.8	29.14	5.9	47.98
1.9	29.20	6	47.16
2	29.31	6.1	46.48
2.1	29.49	6.2	45.63
2.2	29.72	6.3	45.94
2.3	29.98	6.4	45.94
2.4	30.29	6.5	45.76
2.5	30.62	6.6	47.07
2.6	30.97	6.7	47.49
2.7	31.34	6.8	48.26
2.8	31.71	6.9	49.14
2.9	32.08	7	49.62
3	32.46	7.5	49.71
3.1	32.83	8	48.35
3.2	33.19	9	53.61
3.3	33.54	9.5	53.28
3.4	33.89	10	54.85
3.5	34.19	11	56.67
3.6	34.39	12	52.58
3.7	34.64	15	43.31
3.8	34.92	16	46.12
3.9	35.20	18	39.85
4	35.74	20	36.35

3.6. Integral inelastic scattering cross sections

3.6.1. Pyridine

The present recommended inelastic electron scattering integral cross sections for pyridine are shown in Table 3.8 and plotted in Figure 3.17. The rotational excitation cross sections have been calculated with the Born-based procedure described in Ref. [8]. The electron attachment cross sections have been identified with and derived from the shape resonances predicted by our R-matrix calculation. Concerning the ionizing processes, the most recent total electron impact ionization cross sections (TICS) for pyridine have been measured by Jiao et al. [121] and Bull et al. [122] and show an excellent agreement between them. Therefore, it was selected for the present ionization cross sections an average of both those sets of data, with an uncertainty limit of ~10%. TICSs calculated by applying the energy dependent inelastic threshold procedure [123] to our IAM-SCAR calculation, are in good agreement with this experimental average to within the uncertainty limits. The ratio between the ionization and the electronic excitation cross sections, given by our IAM-SCAR calculation, provided the coefficient used to derive the latter from the total inelastic cross sections, which in turn is derived from the reference TCS values minus the integral elastic cross sections. The remaining cross sections, required to obtain the TCS values as the sum of all the considered elastic and inelastic channels, is then attributed to the vibrational excitation cross section. This procedure ensures that a self-consistent set of integral electron scattering cross section, as shown in Figure 3.17, is obtained.

3.7. Angular distribution functions

3.7.1. Pyridine

After any scattering event, either elastic or inelastic, for transport simulation programs, based on event-by-event Monte Carlo procedures [11], the angular distribution of the scattered electrons has to be sampled. For this purpose, in the case of the elastic processes, it is simply used as the angular distribution functions our normalized elastic differential cross sections, as a function of the scattering angle, calculated with our R-matrix (for 0-10 eV) and IAM-SCAR (from 10 to 100 eV) methods. These calculated DCS, for representative impact energies, are shown in Figure 3.18 (a). Similarly, the present dipole-Born DCS calculation is used to determine the angular distribution function for the rotational excitation processes (see Figure 3.18 (b)).

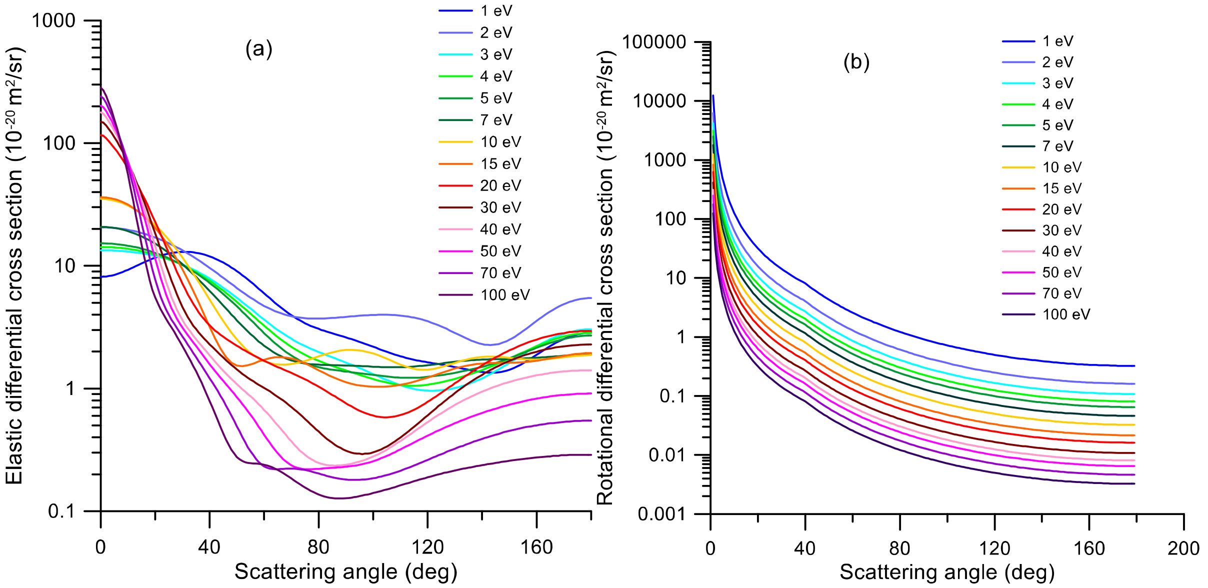

Figure 3.18. (a) Elastic differential cross sections, calculated with our R-matrix (1-15 eV) and IAM-SCAR (20-100 eV) methods, which are used to derive the normalized angular distribution functions for the elastic scattering processes. (b) Calculated dipole-Born differential cross sections used to derive the corresponding angular distribution functions for rotational excitation processes.

For the other inelastic processes it is generally employed the following semi-empirical formula, which provides the inelastic angular distribution as a function of the corresponding elastic DCS and the energy transferred in the scattering event (see Ref. [116] for details):

$$\frac{d^2\sigma(E)}{d\Omega\Delta E} \propto \left(\frac{d\sigma(E)}{d\Omega}\right)_{el}^{1-\Delta\mathrm{E}/\mathrm{E}} \qquad (7)$$

However, from the present measured double differential ionization cross sections, for 90 eV impact energies, this formula is found to be not very accurate for relatively high values of the energy transferred in the collision process. By correlating the observed angular distribution with the calculated elastic DCS, the following semi-empirical formula is obtained:

$$\frac{d^2\sigma(E)}{d\Omega\Delta E} \propto \left(\frac{d\sigma(E)}{d\Omega}\right)_{el}^{\left(1-\frac{\Delta\mathrm{E}}{\mathrm{E}}\right)^k} \qquad (8)$$

where the best fit to the experimental data has been found for k = 1.3. As shown in Figure 3.19, this new formula reproduces the results from the previous one for low energy transfer values and fits reasonably well the observed angular distribution for the relatively high values of the incident electron energy loss. Therefore, it was adopted this new semi-empirical formula for our modelling purposes.

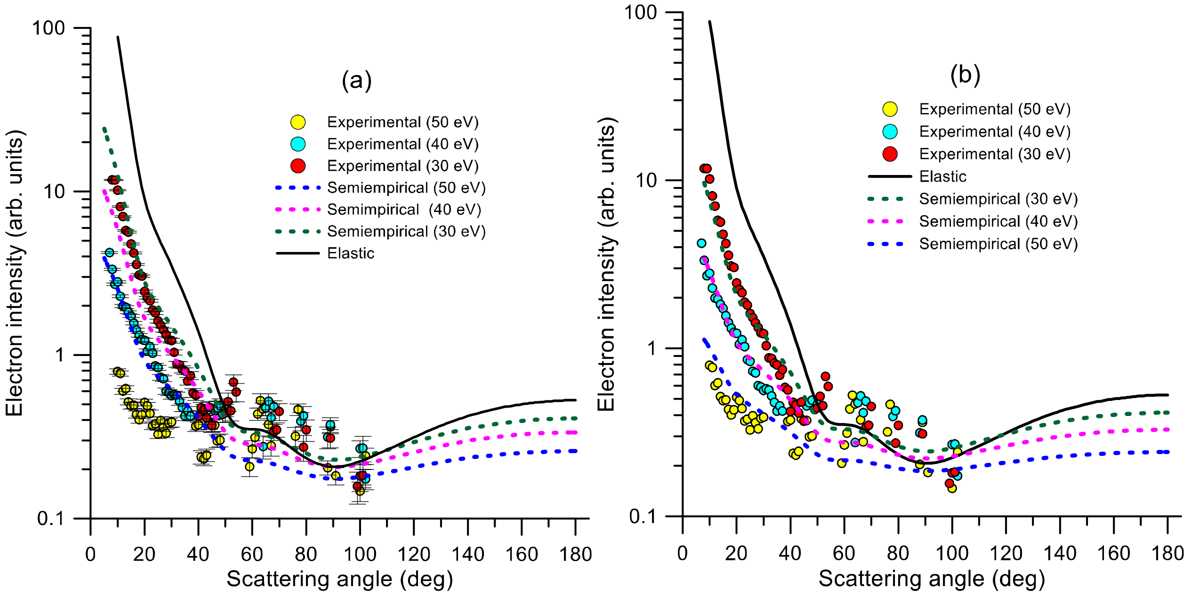

Figure 3.19. Comparison between the angular distributions given by the semi-empirical formulae (Eq. 7 or Eq. 8) for energy losses of 0 (elastic + rotational), 30, 40 and 50 eV, and those measured with the present reaction microscope for a 90 eV electron incident energy. (a) Using our previous semi-empirical formula (Eq. (1)), (b) using the present improved formula (Eq. (2)).

3.8. Energy loss distribution functions

3.8.1. Pyridine

The energy loss distribution functions used for the present simulation have been derived from angular averaged experimental energy loss spectra. Figure 3.20 shows the energy loss distribution functions used for (a) 15 eV and (b) 90 eV incident electron energies, showing the partial distributions for three of the different inelastic channels considered in our simulation, i.e. vibrational excitation, electronic-state excitation and ionization. For the rotational excitations a fixed energy loss of 0.00109 eV (averaged rotational excitation energy at 300 K) has been assumed. For the DEA processes, the incident electrons disappear from the simulation transferring all their kinetic energy to the medium. On the other hand, for elastic processes, only kinetic energy is transferred from the incident electron to the target molecule, with its magnitude being determined by their relative mass ratio. Below 0.1 eV, electrons are culled from the simulation.

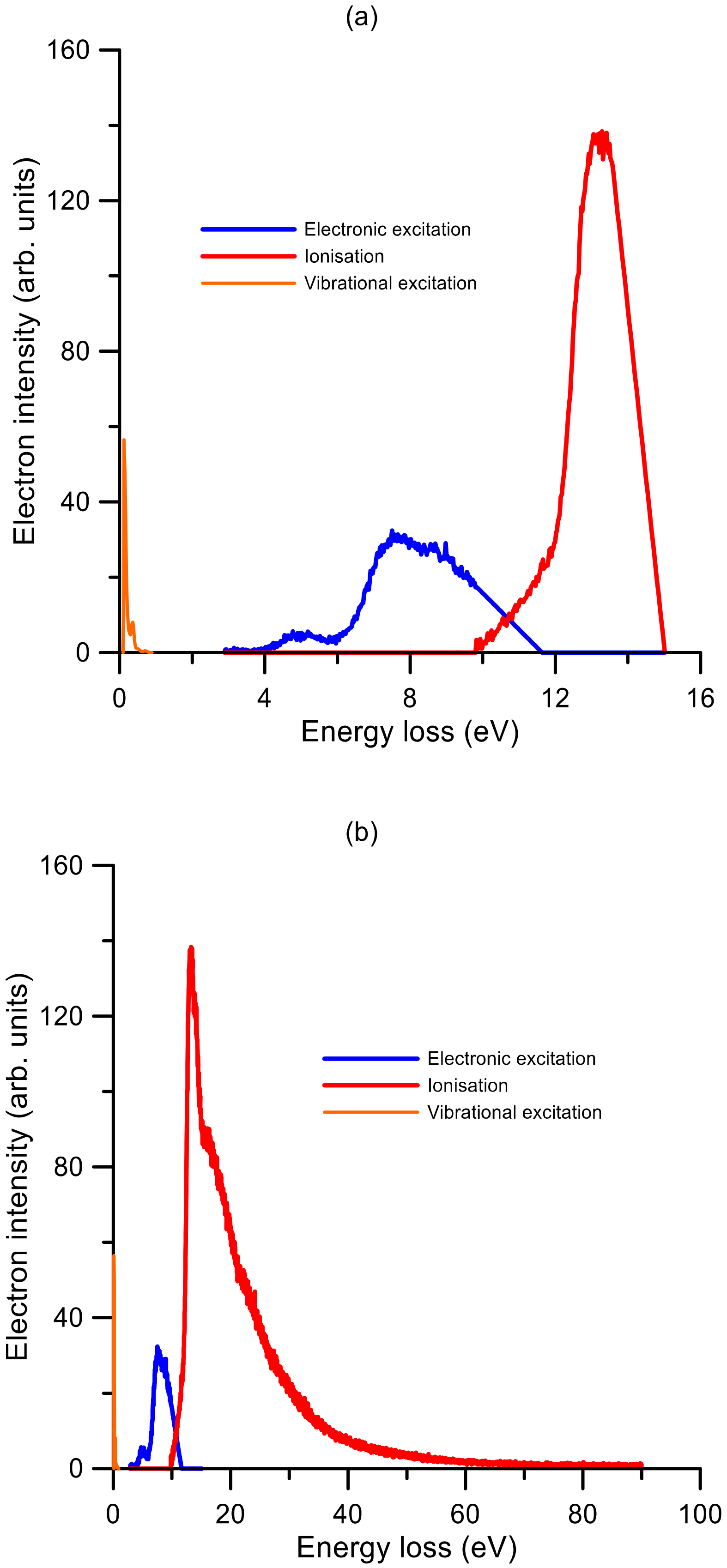

Figure 3.20. Averaged energy loss distribution functions for (a) 15 eV and (b) 90 eV incident electron energies, as used in the present simulations. See also legend in the figure to define the various open scattering processes.

Chapter 4. Discussion

4.1. The role of the dipole moment in electron scattering from molecules

In polar molecules, such as nitrobenzene, special attention to the dipole interactions must be paid both from the theoretical and experimental points of view [29]. As noted above, electron scattering experiments do not generally have a good enough energy resolution to discriminate against rotational excitations. For this reason, electron transmission measurements tend to give lower TCSs than the "true" values, due to the electronically elastic and rotationally inelastic scattered electrons into the detection or acceptance angle (the so called "missing angles"), with the magnitude of this effect dependent on the particular angular resolution in question. In addition rotationally scattered electrons, for energies outside of the "missing angles", effect the measured TCS, as you'd expect in a normal attenuation experiment, so that in those cases where this effect is relevant (e.g. for magnetically confined electron scattering experiments with polar molecules), according to the second alternative proposed in Ref. [29] the magnitude of those contributions should be evaluated before comparing theoretical and experimental cross section data, particularly when the theory does not account for the nuclear degrees of freedom (i.e. rotations and vibrations).

As discussed previously, there is an excellent agreement found between the present TCS measurements and the results of our IAM-SCAR+I calculation without rotational excitation (i.e. the elastic + summed electronic excitation + ionisation integral cross sections). However, from the above discussion, it must be assumed that these data are not completely equivalent. Using our calculated elastic DCSs and integrating these values over the "missing" angular ranges, the contribution of the elastic scattering to this systematic error can be calculated [124]. Therefore, adding this contribution to the measured TCS, it is obtained the corrected values for elastic scattering into the "missing angles" which are shown in Figure 3.11 as the short dashed red line. As may be seen in this figure these "corrected values" are somewhat higher in magnitude than the calculated IAM-SCAR+I TCS for energies above about 200 eV. The reason for this discrepancy is again linked to the "missing" angles. While for the theoretical TCS the rotational excitations are not considered, the experimental values do include for the effect of rotational excitations scattered outside of the "missing angle" ranges. Although these processes are strongly peaked in the forward direction, their contribution is not negligible below 200 eV. This effect can be estimated by now integrating the dipole-Born rotational excitation DCS over the angular range which is complementary to the experimental acceptance angles (i.e. from $\Delta\theta^{\circ}$ to $180^{\circ} - \Delta\theta^{\circ}$). By subtracting that contribution to the former “corrected values” (the short dashed line in Figure 3.11), experimental data corrected for the “missing angle” elastic contribution can be obtained but now not including rotational excitation. These data are also plotted in Figure 3.11 as a dashed-dot line. Although the latter should be equivalent to the calculated IAM-SCAR+I TCS without rotations, in Figure 3.11 it can be observed that below 40 eV it tends to be lower than the calculated values. A possible explanation for this discrepancy is that our Dipole-Born calculation is overestimating the rotational excitation cross section at the lower energies, which is consistent with the well-known nature and limitations of the first Born approximation [79].

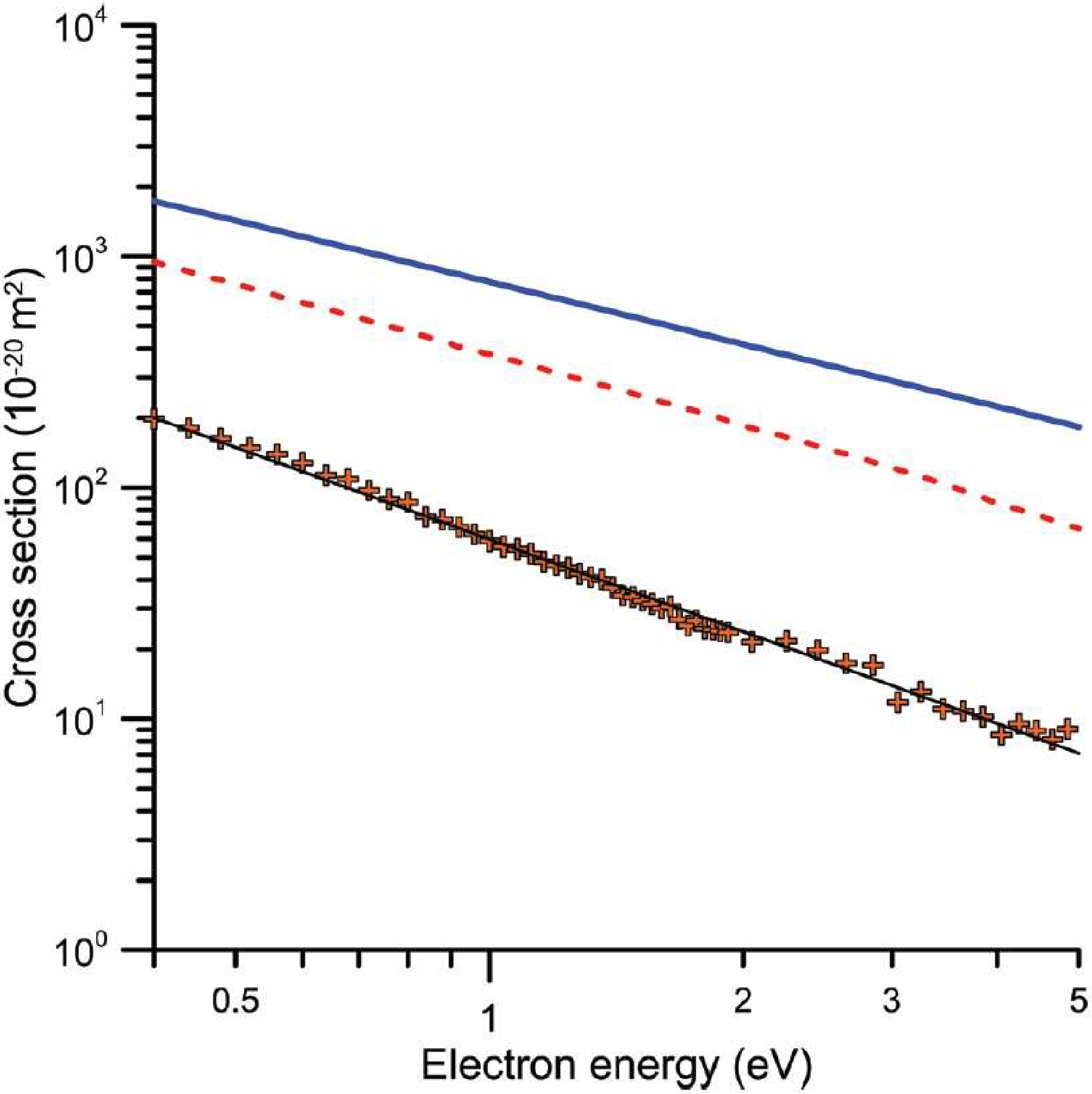

Figure 4.1. Energy dependence of the integral rotational excitation cross sections from 0.4 to 5 eV : —, present dipole-Born calculation; dipole-Born correction from Ref. [106] (---); experimental TCS from Ref. [81] and [82] (+).

Figure 4.1 represents a double logarithmic plot of the integral rotational excitation cross section calculated in this study, within the framework of the Born approximation, together with the Dipole-Born correction to the IECS calculated in Ref. [98] and the low-energy experimental TCS from Refs. [81][82]. The latter includes the elastic scattering processes, but considering the very good energy resolution used in Ref. [81] (better than 8 meV) and the relevance of the rotational excitations in the scattering from highly polar molecules, it can be expected that they dominate the low energy dependence of the TCS. As may be seen in this figure, all of them can be fitted to straight lines with similar slopes. Both calculations give slopes around -1.0, while that for the experimental data is about -1.3. As mentioned above, the latter includes elastic processes but it gives an indication of the energy dependence it would be expected for the rotational excitations which, in the case of such strongly polar molecules as nitrobenzene, are dominant at these low energies. Concerning the absolute values of the rotational integral cross sections, it is clear than the magnitude for those of the present calculation is much higher than that of the others, by a factor 2 when comparing with those from Ref. [98]. Therefore, it can be concluded that even if our Born calculation gives a reasonable energy dependence of the rotational cross sections, it probably overestimates their absolute values.

4.2. Comparison between benzene and nitrobenzene

The main structural difference between benzene and nitrobenzene is caused by the substitution of one of the H atoms of the benzene ring with the NO_2 group, which confers a significant dipole moment to the nitrobenzene molecule. The MCEB experimental TCSs, in the energy range 0.4-300 eV, for both molecules are plotted together in Figure 4.2. If it is assumed that our experimental arrangement is not able to energetically resolve rotational excitations, from pure geometrical considerations the TCSs for both molecules should present a similar structure. As can be seen in this figure, from 10 to 300 eV, the TCSs for both molecules have a similar energy dependence, within the combined uncertainty limits, but in terms of the magnitude those for nitrobenzene are around 40% higher, on average, than those for benzene. This clearly highlights the important role of the molecular polarizability in determining the scattering behaviour [125]. From purely empirical considerations, based on the number of electrons (Z) and the molecular polarizability (α), Garcia and Manero [126] provided an asymptotic formula for the TCS of some molecules. The number of electrons for nitrobenzene and benzene are 64 and 42, respectively, while α is 87.19 a.u. [114] and 70.83 a.u. [114], respectively. According to this empirical formula [126], the TCS of nitrobenzene should be 42.5% higher than that of benzene which is in good agreement with our observation. However, for lower energies (<10 eV) the TCS ratio (nitrobenzene/benzene) is much higher than that expected from the empirical considerations, being about a factor 2 larger at around 2.5 eV. The low energies now under consideration are below the electronic excitation threshold, and therefore this difference might be attributed to differing scattering behaviour in the elastic channel. Nonetheless there is no theoretical reason to justify such different behaviour in the IECS for these two molecules, so it must be considered that rotational excitations in nitrobenzene are leading to the deviation from the empirical behaviour of nitrobenzene versus benzene. As just discussed, this contribution in nitrobenzene can be evaluated by integrating the calculated rotational excitation DCS out of the effective detection angle range. Following the procedure described in the previous section, the TCS-Nitrobenzene (no rota.) data, also plotted in Figure 4.2, represents the experimental TCS cross section plus the elastic contribution to the "missing angles" and minus the rotational excitation contribution from out of the acceptance angle range. This correction mainly affects the lower energies, below 20 eV, and gives nitrobenzene TCS values which are closer to those of benzene, being even lower than benzene below 4 eV. This comparison again indicates, in concordance with the previous discussion, that our Dipole-Born rotational excitation calculation significantly overestimates the magnitude of this contribution.

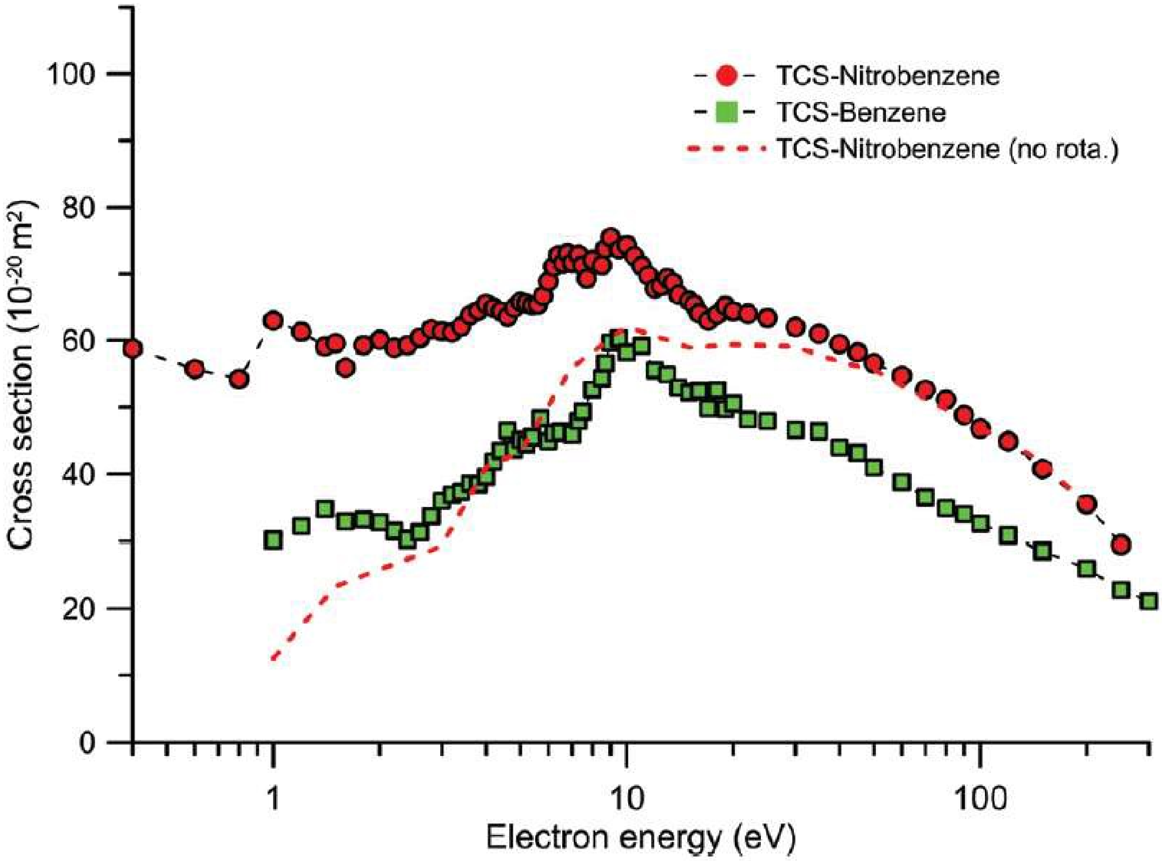

Figure 4.2. Total electron scattering cross sections (10^{-20} m^2) for benzene (🟩) and nitrobenzene (●) as measured with our MCEB apparatus.

4.3. Simulation with pyridine

The complete set of consistent cross section data is now used to simulate the electron transport through a gas cell containing pyridine, under intense magnetic field confinement conditions. Basically, however, a linear electron beam, generated by an emitting filament, is accelerated along the axis of a cylindrical chamber where it is guided by a uniform axial magnetic field and into that chamber a constant well-defined pressure of gaseous pyridine is introduced through a leak valve. The applied magnetic field is intense enough (around 0.1 T) to confine the gyro-motion of the electron beam into a gyro-radius of a few microns, which is therefore negligible in comparison with the electron beam radius that is defined by the entrance and exit apertures of the chamber (each being 1.5 mm in diameter). Under these conditions, in any collision event the scattering angle is converted into a decrement of the parallel (axial) component of the velocity, which in turn represents a kinetic energy loss in the parallel direction, that can be measured with a potential barrier applied in front of an electron multiplier detector, i.e. with a retarding potential analyser (RPA). The measured electron intensity distribution of the parallel kinetic energy, for a 15 eV electron beam generated in these experimental conditions, is plotted in Figure 4.3 together with the corresponding intensity distribution when a gas pressure of 2 mTorr of pyridine is introduced into the scattering chamber. The corresponding electron intensity distributions simulated with our Low Energy Particle Track Simulation (LEPTS) procedure [11][116] are also plotted in Figure 4.3. LEPTS is an event by event Monte Carlo simulation code which, according to the above integral cross section data set and the angular and energy-loss distribution functions, is sampling when a collision event is taking place and the type of interaction corresponding to this event as well as the energy transferred to the molecular target, the secondary particles generated and the scattering angle corresponding to both the primary and secondary electrons. Under the magnetic confinement conditions used in this experiment, the scattering angle distribution function is crucial to define the energy distribution along the magnetic axis. This particular configuration is especially suitable to evaluate the efficacy of the input DCS data used in the simulation.

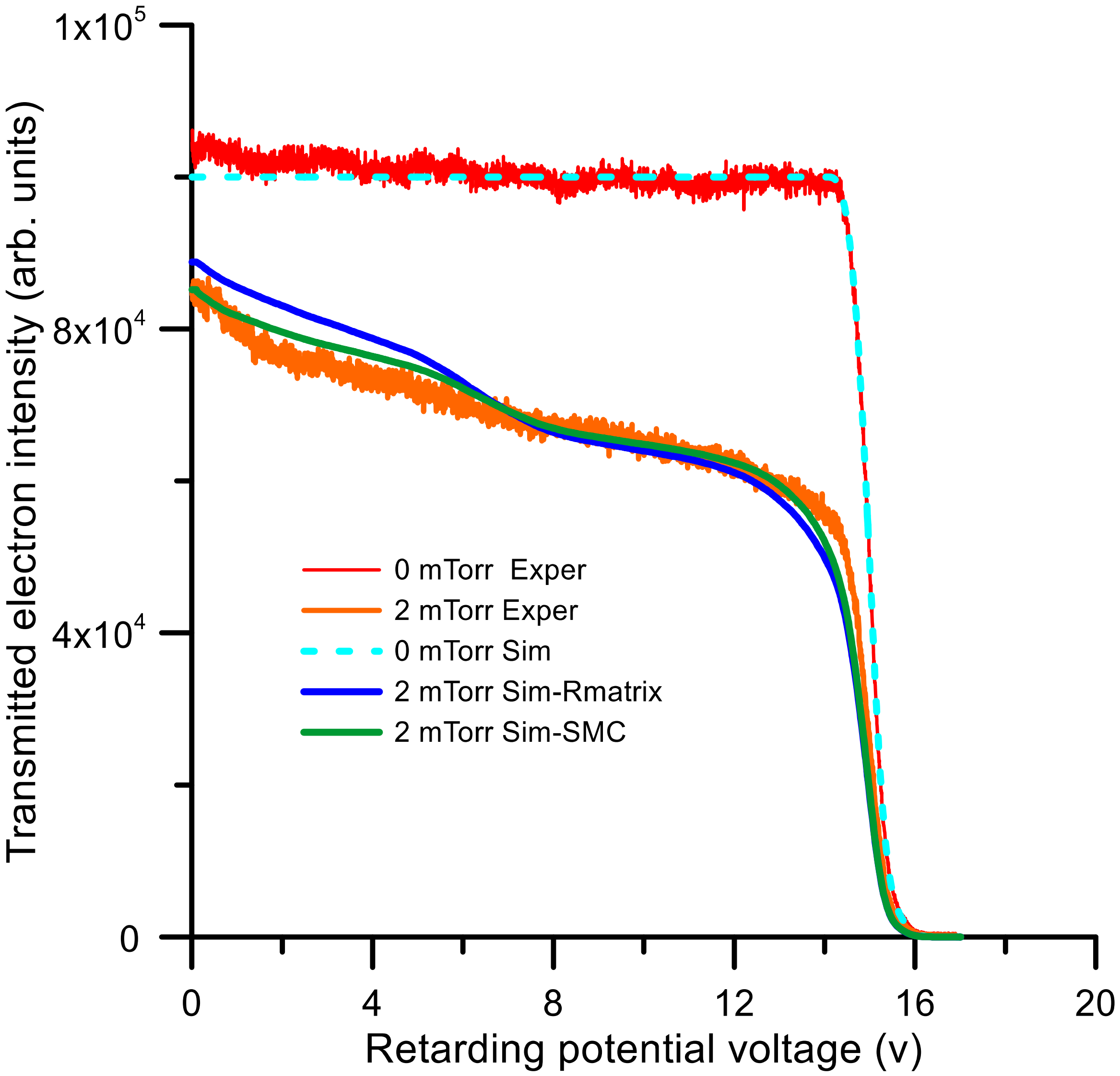

Figure 4.3. Transmitted electron intensity distribution (i.e. the intensity of the electrons with axial kinetic energy above the retarding potential barrier) through 0 and 2 mTorr of pyridine, respectively, for a 15 eV incident electron energy beam.

As shown in Figure 4.3 for a 15 eV incident electron energy, considering the strong dependence of the simulated electron intensity distribution on the elastic and inelastic DCS values used as the input information, the agreement between the experiment and the simulation is fairly good, but not perfect. In the case of para-Benzoquinone [60], our group recently obtained an excellent agreement between the simulated and experimental electron intensity distribution under similar conditions to the present. Both molecules have a similar molecular structure, but the main difference is that pyridine has an important permanent dipole moment while p-Benzoquinone is non-polar. The limitations of the Born-type procedures used to account for the dipole interactions in our electron scattering cross section calculations have been pointed out in Refs. [29][14], and could justify, at least in part, these observed discrepancies. Note that the simulation is overestimating the effect of the angular dependence in the scattering, so producing an increment in the electron energy loss which in turn increments the intensity of the low energy electrons, in comparison with the experimental result. From a closer inspection of Figure 4.3 it can be observed that the intensity distribution given by the simulation based on the SMC calculation fits better the experimental result than that based on the R-matrix data. This is an apparent contradiction with the fact that the IECS derived from the SMC calculation does not match very well the experimental TCS, when the "missing angle" limitation is considered. However, as already mentioned, the magnetically confined conditions of this experiment cause the simulated transmitted intensity to be very sensitive to the input DCS values. Although the IECSs for 10–15 eV given by the SMC method are higher in magnitude than those of the R-matrix, their corresponding DCSs are more peaked in the forward direction, thus producing less important energy loss than that derived by the R-matrix method. Because of this, the SMC calculation gives a transmitted electron intensity distribution closer to the experimental one.

It is also interesting to see what happens at higher impact energies, where the ideal magnetic confinement conditions assumed in the simulation might not apply. These results are shown in Figure 4.4, where the experimental electron intensity transmitted through the gas cell containing 0 and 2.5 mTorr of pyridine, respectively, together with the corresponding simulation for an incident electron energy of 90 eV are plotted. As shown in this figure, there is a clear disagreement between the observed and simulated transmitted electron intensity distributions in this case. The SMC and R-matrix results do agree well with each other, but this is normal since for 90 eV the scattering data used for the LEPTS program are largely those calculated with the IAM-SCAR procedure which is common for both sets of data for incident electron energies above 20 eV.

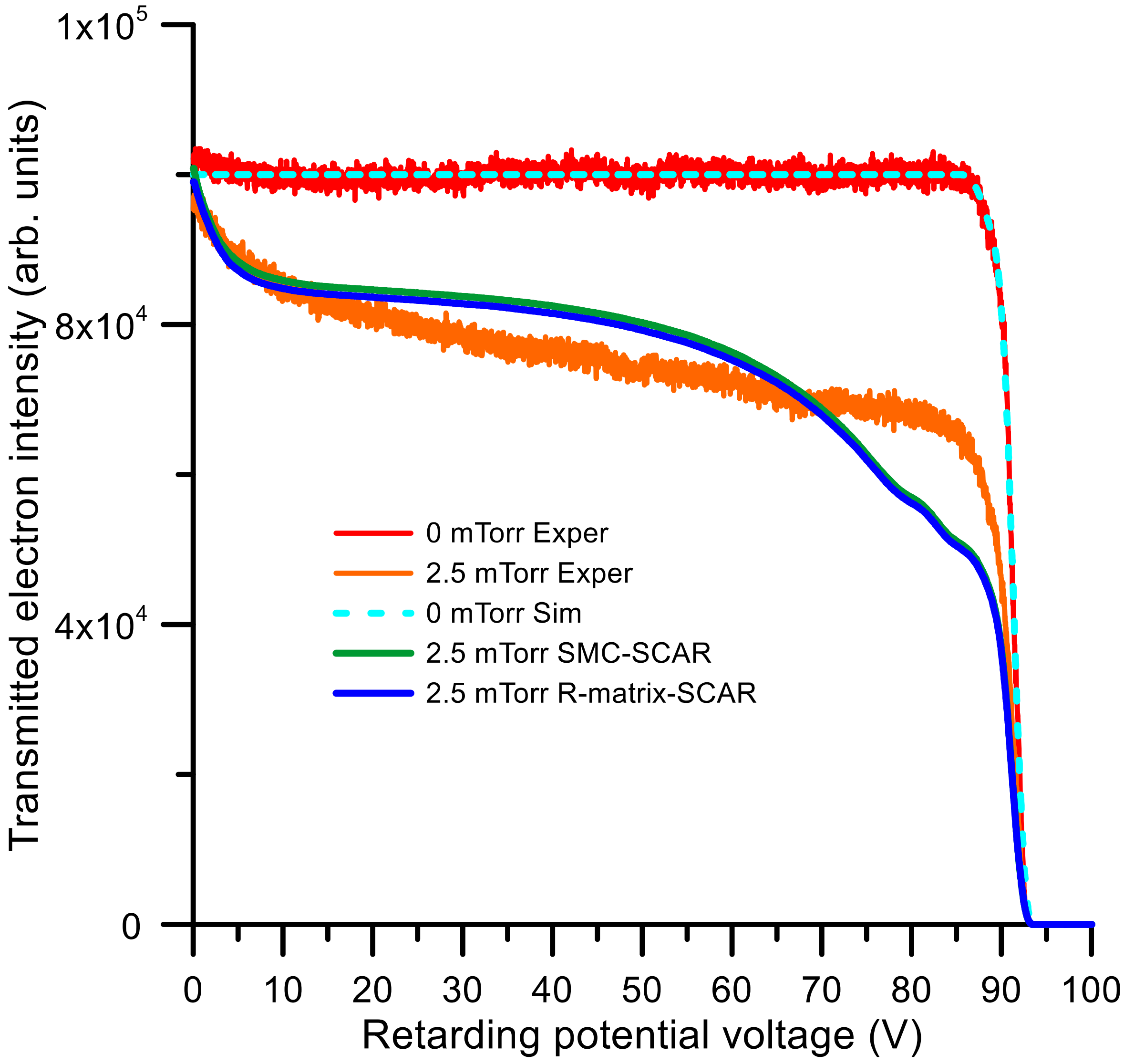

Figure 4.4. Transmitted electron intensity distribution (i.e. the intensity of the electrons with axial kinetic energy above the retarding potential barrier) through 0 and 2.5 mTorr of pyridine, respectively, but now for a 90 eV incident electron energy beam.

The observed differences between the measurement and simulation in Figure 4.4, seem to indicate that the angular distribution function derived from the calculated elastic DCS, as used in the simulation, tends to favour the larger scattering angles more than what the measured transmitted intensity distribution suggests is actually the case. The IAM-SCAR elastic DCS at 90 eV is supposed to be accurate to within 10%, as deduced from comparisons with accurate DCS measurements for different aromatic molecules and other halogenated compounds [127][128]. It was not found any experimental DCS data for pyridine at around 100 eV but the recent calculation from Gholami et al. [129] shows a reasonable agreement with the present calculation at 100 eV. Assuming that the calculated IAM-SCAR DCS at 90 eV are correct, a possible reason for the discrepancy between the experimental and simulated electron transport results in Figure 4.4 may be lack of effectiveness of the magnetic field to confine the electron beam at that relatively high energy. Increasing the magnetic field intensity along the scattering chamber, to explicitly test that hypothesis, would require some technical modifications in the current experimental setup, which will be the subject for further investigations. Candidates for future transmission studies are the molecules benzene and nitrobenzene, which are prototype cyclic molecules without and with a permanent dipole moment, respectively.

As mentioned in the introduction of this thesis, a further application of the present modelling procedure would be the evaluation of radiation-induced molecular damage in biological media. Since early experiments showing that low energy electrons can efficiently damage DNA [130], a great effort has been made to obtain electron interaction data for DNA bases in the condensed phase [131]. In these conditions, below 20 eV, electron scattering data for single molecules are affected by the structural arrangement of the condensed medium. We have introduced a geometrical procedure to partially account for this effect, which is able to provide results on the energy deposition and stopping power in good agreement with the experiment [132]. However, a detailed description of the induced molecular damage would require accurate experimental fragmentation patterns for condensed molecules [133]. This is one of our current lines of research [133], which may lead to a realistic comparison between the simulated radiation-induced damage to DNA and the experimental results with condensed molecules.

Chapter 5. Conclusions

5.1. Concluding remarks

The focus of this thesis was the study of electron scattering collisions with biologically relevant molecules. With this objective, the molecules of benzene, nitrobenzene and pyridine were carefully studied using different techniques and over a broad range of energy. These molecules are very valuable because they act as precursors or belong to the basic structures of some of the most important molecules related with human life, such as the DNA. Despite mentioning different apparatus, the emphasis of this thesis dropped on the LTB system for medium to high energies, which suffered small but necessary changes which resulted in measurement improvements. The scattering chamber was slightly modified, and the electron gun was brought closer to the collision chamber, which improved the current obtained, and the detection became consequently better.

In the chapter Results, experimental results for the total electron scattering cross sections of benzene in the energy range 1-1000 eV, as well as first-time results regarding the molecule of nitrobenzene in the energy range 100-1000 eV were presented. Certainly, the current TCS measurements represent an important step towards the availability of an electron-benzene and electron-nitrobenzene interaction data set for simulation with LEPTS or other purposes. Noteworthy, all the local maxima found in the low-energy dependence of the obtained TCS have been identified as either shape or Feshbach resonances. The IAM-SCAR method was used as a valuable complement to experimental studies, especially due to the wide energy (and angular, in the case of DCSs) range and sometimes incomplete experimental data coverage. The results for nitrobenzene have been compared with those obtained for benzene, and as a result of this comparison, there is a need for a careful evaluation of the rotational excitation contribution to the experimental TCS measurements before comparing TCS results from different targets. Nonetheless, the TCS comparison between nitrobenzene and benzene clearly illustrated the very important role played by the target polarizability in the scattering dynamics. In addition, it was shown that the Born approximation tends to overestimate the rotational excitation cross section for the lower electron impact energies. Therefore, it can be concluded that a more sophisticated theoretical electron-molecule scattering analysis, including nuclear motion, is needed to properly quantify the contribution of the rotational excitation to the total cross section. Importantly, due to the significant dipole moment of the nitrobenzene molecule, the rotational excitation contribution to this effect is quite considerable for both experimental configurations and therefore needs to be taken into account before any comparison with either theoretical or other experimental data is attempted.

For the case of the molecule of pyridine, a self-consistent and complete set of differential and integral electron scattering cross sections is presented for the electron impact energies 0.1-100 eV, together with double differential ionization cross sections for 90 eV electron incident energy. As a result, our previous semi-empirical formula could be improved to account for higher energy-loss values. The energy distributions of electron transmitted through pyridine for 15 eV and 90 eV incident electron energies, respectively, were simulated and for 15 eV and found a reasonable level of agreement between the experimental and simulated spectra, confirming the reliability of the present cross section data set. At 90 eV the observed disagreement between the simulated and measured transmitted experiments indicated some failure of the magnetic confinement conditions, for the higher energies, suggesting an upgrade of the present experimental configuration to allow for more intense magnetic fields.

5.2. Future work

Through the period spent doing this thesis, many ideas for future investigations have appeared, whether they are improvements to the current experimental system or studies with other molecular targets. Regarding the improvements, one can assume that the LTB system should return to its initial configuration using two hemispherical analysers instead of just one. These improvements would not require a significant change in the system. Another possible improvement would be to add the study of ionization to this system, through measuring ionisation cross sections, which was not something that was possible to fulfil during this work. This would require implementation of new components in order to allow for additional information to be obtained. One of these components would be a time-of-flight (TOF), positioned right above the collision chamber, which would allow the system to make these types of new measurements. All of this would increase the value of the obtained data, as well as increase the scientific contribution that this technique can provide mostly to the field of interaction of radiation with matter.

The values of the total cross section can be extremely important because they can also be used as input data in radiotherapy simulation and are able to take into consideration many of the nanoscopic processes that take place all the time. Knowing this, it would be very important to keep working on the current lack of data, regarding for example, information about ionisation cross sections or total cross sections for every possible incident energy. Using different molecules is also something that is needed to be taken into consideration, besides water and DNA, molecules such as amino acids, vitamins, and different types of sugars are all quite important and should be studied. There is also the possibility to further study smaller molecular targets, such as elementary atoms which may still not be fully studied but are present in all life forms in small quantities. This latest approach brings up several advantages, since smaller molecules imply that the available energy will be smaller and therefore it would be easier to perform measurements, at lower collision energies.

While performing future experiments using the reaction microscope, it is mandatory to record as many different conditions as possible. This will allow to cover a wide range of angular distribution and transferred energy, with the aim of obtaining a more complete set of data. The reaction microscope is a unique apparatus capable of colleting important collisional information that the scientific community is needing. Thus, it is important to measure new molecules and molecules similar to the ones already studied, to complement theoretical data and establish data-comparison analysis with the existent data.

Bibliography

[1] P. Swiderek, “Fundamental processes in radiation damage of DNA,” *Angew. Chemie - Int. Ed.*, vol. 45, no. 25, pp. 4056–4059, 2006.

[2] S. Uehara, H. Nikjoo, and D. T. Goodhead, “Comparison and Assessment of Electron Cross Sections for Monte Carlo Track Structure Codes,” *Radiat. Res.*, vol. 152, no. 2, p. 202, Aug. 1999.

[3] V. Cobut, Y. Frongillo, J. P. Patau, T. Goulet, M. J. Fraser, and J. P. Jay-Gerin, “Monte Carlo simulation of fast electron and proton tracks in liquid water - I. Physical and physicochemical aspects,” *Radiation Physics and Chemistry*, vol. 51, no. 3. Elsevier Sci Ltd, pp. 229–243, 01-Mar-1998.

[4] E. Alizadeh and L. Sanche, “Precursors of solvated electrons in radiobiological physics and chemistry,” *Chemical Reviews*, vol. 112, no. 11. American Chemical Society, pp. 5578–5602, 14-Nov-2012.

[5] F. Costa *et al.*, “Experimental and theoretical analysis for total electron scattering cross sections of benzene,” *J. Chem. Phys.*, vol. 151, no. 8, 2019.

[6] F. Blanco *et al.*, “Modelling low energy electron and positron tracks in biologically relevant media,” *Eur. Phys. J. D*, vol. 67, no. 9, pp. 1–18, 2013.

[7] B. D. Michael and P. O. Neill, “Electron Tracks,” vol. 287, no. March, 2000.

[8] A. Sieradzka, F. Blanco, M. C. Fuss, Z. Mašín, J. D. Gorfinkiel, and G. García, “Electron scattering from pyridine,” *J. Phys. Chem. A*, vol. 118, no. 33, pp. 6657–6663, 2014.

[9] A. T. Dubuis *et al.*, “Total electron scattering cross section from pyridine molecules in the energy range 10–1000 eV,” *Chem. Phys. Lett.*, vol. 699, pp. 182–187, 2018.

[10] A. I. Lozano, J. Jiménez, F. Blanco, and G. García, “Total electron-scattering cross sections from pyridine molecules in the energy range 1-200 eV,” *Phys. Rev. A*, vol. 98, no. 1, p. 012709, Jul. 2018.

[11] G. G. Gómez-Tejedor and M. C. Fuss, Eds., *Radiation Damage in Biomolecular Systems*. Springer, Dordrecht, 2012.

[12] H. Tanaka, M. J. Brunger, L. Campbell, H. Kato, M. Hoshino, and A. R. P. Rau, “Scaled plane-wave Born cross sections for atoms and molecules,” *Rev. Mod. Phys.*, vol. 88, no. 2, May 2016.

[13] W. Chen, S. Chen, Y. Dong, P. Cloutier, Y. Zheng, and L. Sanche, “Absolute cross-sections for DNA strand breaks and crosslinks induced by low energy electrons,” *Phys. Chem. Chem. Phys.*, vol. 18, no. 48, pp. 32762–32771, Dec. 2016.

[14] L. Álvarez *et al.*, “Electron scattering cross sections from nitrobenzene in the energy range 0.4–1000 eV: the role of dipole interactions in measurements and calculations,” *Phys. Chem. Chem. Phys.*, vol. 22, no. 24, pp. 13505–13515, Jun. 2020.

[15] F. Costa *et al.*, “A Complete Cross Section Data Set for Electron Scattering by Pyridine : Modelling Electron Transport in the Energy Range 0 – 100 eV,” 2020.

[16] A. Traoré Dubuis *et al.*, “Total cross section of furfural by electron impact: Experiment and theory,” *J. Chem. Phys.*, vol. 147, no. 5, 2017.

[17] Y. Itikawa, “Cross sections for electron collisions with nitrogen molecules,” *J. Phys. Chem. Ref. Data*, vol. 35, no. 1, pp. 31–53, 2006.

[18] A. I. Lozano *et al.*, “Magnetically confined electron beam system for high resolution electron transmission-beam experiments,” *Rev. Sci. Instrum.*, vol. 89, no. 6, pp. 1–8, 2018.

[19] J. Ullrich, R. Moshammer, A. N. Perumal, and R. Moshammer, “Reports on Progress in Physics Related content Recoil-ion and electron momentum spectroscopy : Recoil-ion and electron momentum spectroscopy :,” *Rep. Prog. Phys*, vol. 66, no. 9, p. 1463, 2003.

[20] A. Dorn *et al.*, “Double ionization of helium by electron-impact: Complete pictures of the four-body breakup dynamics,” *Phys. Rev. Lett.*, vol. 86, no. 17, pp. 3755–3758, 2001.

[21] E. Wang, X. Ren, W. Y. Baek, H. Rabus, T. Pfeifer, and A. Dorn, “Water acting as a catalyst for electron-driven molecular break-up of tetrahydrofuran,” *Nat. Commun.*, vol. 11, no. 1, pp.

1–7, 2020.
[22] A. S. Barbosa and M. H. F. Bettega, “Elastic scattering of low-energy electrons by tetrahydropyran,” *J. Phys. Conf. Ser.*, vol. 635, no. 1, 2015.
[23] R. F. Da Costa, M. T. D. N. Varella, M. H. F. Bettega, and M. A. P. Lima, “Recent advances in the application of the Schwinger multichannel method with pseudopotentials to electron-molecule collisions,” *Eur. Phys. J. D*, vol. 69, no. 6, 2015.
[24] J. D. Gorfinkiel, A. Faure, S. Taioli, C. Piccarreta, G. Halmová, and J. Tennyson, “Electron-molecule collisions at low and intermediate energies using the R-matrix method,” *Eur. Phys. J. D*, vol. 35, no. 2, pp. 231–237, 2005.
[25] F. Blanco and G. García, “Improvements on the quasifree absorption model for electron scattering,” *Phys. Rev. A - At. Mol. Opt. Phys.*, vol. 67, no. 2, p. 9, Feb. 2003.
[26] A. S. Barbosa and M. H. F. Bettega, “Shape resonances, virtual state, and Ramsauer-Townsend minimum in the low-energy electron collisions with benzene,” *J. Chem. Phys.*, vol. 146, no. 15, p. 154302, Apr. 2017.
[27] F. Blanco and G. García, “Screening corrections for calculation of electron scattering from polyatomic molecules,” *Phys. Lett. Sect. A Gen. At. Solid State Phys.*, vol. 317, no. 5–6, pp. 458–462, Oct. 2003.
[28] F. Blanco, L. Ellis-Gibbings, and G. García, “Screening corrections for the interference contributions to the electron and positron scattering cross sections from polyatomic molecules,” *Chem. Phys. Lett.*, vol. 645, pp. 71–75, Feb. 2016.
[29] I. I. Fabrikant, “Long-range effects in electron scattering by polar molecules,” *J. Phys. B At. Mol. Opt. Phys.*, vol. 49, no. 22, p. 222005, Nov. 2016.
[30] H. Kato *et al.*, “A study of electron scattering from benzene: Excitation of the1B1u,3E2g, and1E1uelectronic states,” *J. Chem. Phys.*, vol. 134, no. 13, 2011.
[31] “Benzene | C6H6 - PubChem.” [Online]. Available: https://pubchem.ncbi.nlm.nih.gov/compound/Benzene. [Accessed: 22-Apr-2020].
[32] “Benzene.” [Online]. Available: https://webbook.nist.gov/cgi/cbook.cgi?ID=C71432&Mask=20#Ion-Energetics. [Accessed: 24-Sep-2020].
[33] J. A. Raleigh, J. D. Chapman, J. Borsa, W. Kremers, and A. P. Reuvers, “Radiosensitization of mammalian cells by p-nitroacetophenone: III. Effectiveness of nitrobenzene analogues,” *Int. J. Radiat. Biol.*, vol. 23, no. 4, pp. 377–387, Apr. 1973.
[34] J. E. Biaglow and R. E. Durand, “The effects of nitrobenzene derivatives on oxygen utilization and radiation response of an in vitro tumor model.,” *Radiat. Res.*, vol. 65, no. 3, pp. 529–39, Mar. 1976.
[35] “Nitrobenzene | C6H5NO2 - PubChem.” [Online]. Available: https://pubchem.ncbi.nlm.nih.gov/compound/Nitrobenzene. [Accessed: 22-Apr-2020].
[36] R. N. Compton, R. H. Huebner, P. W. Reinhardt, and L. G. Christophorou, “Threshold Electron Impact Excitation of Atoms and Molecules: Detection of Triplet and Temporary Negative Ion States,” *J. Chem. Phys.*, vol. 48, no. 2, pp. 901–909, Jan. 1968.
[37] L. G. Christophorou, R. N. Compton, G. S. Hurst, and P. W. Reinhardt, “Dissociative electron capture by benzene derivatives,” *J. Chem. Phys.*, vol. 45, no. 2, pp. 598–600, Jul. 1966.
[38] K. Jager and A. Z. Henglein, “Z. Naturforsch,” in *22a*, 1967, p. 700.
[39] A. Modellia and M. Venuti, “Empty level structure and dissociative electron attachment in gas-phase nitro derivatives,” *Int. J. Mass Spectrom.*, vol. 205, no. 1–3, pp. 7–16, Feb. 2001.
[40] N. L. Asfandiarov, E. P. Nafikova, and S. A. Pshenichnyuk, “Interpreting electron transmission spectroscopy and negative ion mass spectrometry data using a spherical potential well model,” *J. Exp. Theor. Phys.*, vol. 104, no. 3, pp. 357–362, Mar. 2007.
[41] A. Pelc, P. Scheier, and T. D. Märk, “Low-energy electron interaction with nitrobenzene: C6H5NO2,” *Vacuum*, vol. 81, no. 10, pp. 1180–1183, Jun. 2007.
[42] “Benzene, nitro-.” [Online]. Available: https://webbook.nist.gov/cgi/cbook.cgi?ID=C98953&Mask=20#Ion-Energetics. [Accessed: 24-Sep-2020].
[43] “Pyridine | C5H5N - PubChem.” [Online]. Available: https://pubchem.ncbi.nlm.nih.gov/compound/Pyridine. [Accessed: 22-Apr-2020].

[44] D. Stevens *et al.*, “Positron scattering from pyridine,” *J. Chem. Phys.*, vol. 148, no. 14, 2018.
[45] W. Holst and J. Holtsmark, “No Title,” *Det. Kgl. Nor. Videndskab. Selsk.*, vol. 4, no. 89, 1931.
[46] O. Sueoka, “Total cross section measurements for positron and electron scattering on benzene molecules,” *J. Phys. B At. Mol. Opt. Phys.*, vol. 21, no. 20, p. L631, 1988.
[47] P. Mozejko, G. Kasperski, C. Szmytkowski, G. P. Karwasz, R. S. Brusa, and A. Zecca, “Absolute total cross section measurements for electron scattering on benzene molecules,” *Chem. Phys. Lett.*, vol. 257, no. 3–4, pp. 309–313, Jul. 1996.
[48] R. J. Gulley, S. L. Lunt, J.-P. Ziesel, and D. Field, “Very low energy electron scattering from benzene and deuterated benzenes,” *J. Phys. B At. Mol. Opt. Phys.*, vol. 31, no. 12, p. 2735, 1998.
[49] G. P. Karwasz, R. S. Brusa, and A. Zecca, “No Title,” *Rev. Nuovo Cim.*, vol. 24, 2001.
[50] C. Makochekanwa, O. Sueoka, and M. Kimura, “Comparative study of electron and positron scattering from benzene [Formula Presented] and hexafluorobenzene [Formula Presented] molecules,” *Phys. Rev. A - At. Mol. Opt. Phys.*, vol. 68, no. 3, p. 8, Sep. 2003.
[51] M. Kimura, C. Makochekanwa, and O. Sueoka, “Contrasting low-energy behaviour in total cross sections for electron and positron scattering from benzene molecules,” *J. Phys. B At. Mol. Opt. Phys.*, vol. 37, no. 7, p. 1461, Mar. 2004.
[52] F. A. Gianturco and R. R. Lucchese, “One-electron resonances and computed cross sections in electron scattering from the benzene molecule,” *J. Chem. Phys.*, vol. 108, no. 15, pp. 6144–6159, Apr. 1998.
[53] M. H. F. Bettega, C. Winstead, and V. McKoy, “Elastic scattering of low-energy electrons by benzene,” *J. Chem. Phys.*, vol. 112, no. 20, pp. 8806–8812, May 2000.
[54] Y. Jiang, J. Sun, and L. Wan, “Additivity rule for the calculation of electron scattering from polyatomic molecules,” *Phys. Rev. A - At. Mol. Opt. Phys.*, vol. 62, no. 6, pp. 062712–062711, Dec. 2000.
[55] J. Sun, C. Du, and Y. Liu, “Total cross sections for electron scattering on polyatomic molecules - Considering two different shielding effects,” *Phys. Lett. Sect. A Gen. At. Solid State Phys.*, vol. 314, no. 1–2, pp. 150–155, Jul. 2003.
[56] S. Singh, R. Naghma, J. Kaur, and B. Antony, “Calculation of total and ionization cross sections for electron scattering by primary benzene compounds,” *J. Chem. Phys.*, vol. 145, no. 3, p. 034309, Jul. 2016.
[57] D. Prajapati, H. Yadav, P. C. Vinodkumar, C. Limbachiya, A. Dora, and M. Vinodkumar, “Computation of electron impact scattering studies on benzene,” *Eur. Phys. J. D*, vol. 72, no. 12, 2018.
[58] H. Kato *et al.*, “Electron and positron scattering from the benzene derivative benzotrifluoride: Total and vibrational excitation cross sections,” *Phys. Rev. A - At. Mol. Opt. Phys.*, vol. 79, no. 6, p. 062702, Jun. 2009.
[59] A. T. Dubuis *et al.*, “Total electron scattering cross section from pyridine molecules in the energy range 10–1000 eV,” *Chem. Phys. Lett.*, vol. 699, pp. 182–187, May 2018.
[60] A. I. Lozano *et al.*, “Total electron scattering cross sections from: Para -benzoquinone in the energy range 1-200 eV,” *Phys. Chem. Chem. Phys.*, vol. 20, no. 34, pp. 22368–22378, Aug. 2018.
[61] J. Tennyson, “Electron-molecule collision calculations using the R-matrix method,” *Physics Reports*, vol. 491, no. 2–3. North-Holland, pp. 29–76, 01-Jun-2010.
[62] “Quantemol.” [Online]. Available: http://www.quantemol.com/. [Accessed: 08-May-2020].
[63] G. García, J. L. de Pablos, F. Blanco, and A. Williart, “Total and elastic electron scattering cross sections from Xe at intermediate and high energies,” *J. Phys. B At. Mol. Opt. Phys.*, vol. 35, no. 22, p. 4657, Nov. 2002.
[64] M. Allan, “Study of triplet states and short-lived negative ions by means of electron impact spectroscopy,” *Journal of Electron Spectroscopy and Related Phenomena*, vol. 48, no. 2. Elsevier, pp. 219–351, 01-Jan-1989.
[65] P. D. Burrow, J. A. Michejda, and K. D. Jordan, “Electron transmission study of the temporary negative ion states of selected benzenoid and conjugated aromatic hydrocarbons,” *J. Chem. Phys.*, vol. 86, no. 1, pp. 9–24, Jan. 1987.
[66] L. Sanche and G. J. Schulz, “Electron transmission spectroscopy: Resonances in triatomic

molecules and hydrocarbons," *J. Chem. Phys.*, vol. 58, no. 2, pp. 479–493, Jan. 1973.

[67] I. Nenner and G. J. Schulz, "Temporary negative ions and electron affinities of benzene and N-heterocyclic molecules: Pyridine, pyridazine, pyrimidine, pyrazine, and s-triazine," *J. Chem. Phys.*, vol. 62, no. 5, pp. 1747–1758, Mar. 1975.

[68] P. D. Burrow, A. Modelli, and K. D. Jordan, "Temporary anion states of the chlorobenzenes," *Chem. Phys. Lett.*, vol. 132, no. 4–5, pp. 441–447, Dec. 1986.

[69] C. Winstead and V. McKoy, "Low-energy electron scattering by pyrazine," *Phys. Rev. A - At. Mol. Opt. Phys.*, vol. 76, no. 1, pp. 1–6, 2007.

[70] Y. Li, J. Wan, and X. Xu, "Theoretical study of the vertical excited states of benzene, pyrimidine, and pyrazine by the symmetry adapted cluster—Configuration interaction method," *J. Comput. Chem.*, vol. 28, no. 10, pp. 1658–1667, Jul. 2007.

[71] J. P. Doering, "Low-energy electron-impact study of the first, second, and third triplet states of benzene," *J. Chem. Phys.*, vol. 51, no. 7, pp. 2866–2870, Oct. 1969.

[72] R. Azria and G. J. Schulz, "Vibrational and triplet excitation by electron impact in benzene," *J. Chem. Phys.*, vol. 62, no. 2, pp. 573–575, Sep. 1975.

[73] M. Allan, "Forward Electron Scattering in Benzene; Forbidden Transitions and Excitation Functions," *Helv. Chim. Acta*, vol. 65, no. 7, pp. 2008–2023, Nov. 1982.

[74] E. E. Koch and A. Otto, "Optical absorption of benzene vapour for photon energies from 6 eV to 35 eV," *Chem. Phys. Lett.*, vol. 12, no. 3, pp. 476–480, Jan. 1972.

[75] A. Muñoz *et al.*, "Single electron tracks in water vapour for energies below 100 eV," *Int. J. Mass Spectrom.*, vol. 277, no. 1–3, pp. 175–179, Nov. 2008.

[76] D. E. Cullen, J. H. Hubbell, and L. Kissel, "EPDL97: The Evaluated Photon Data Library '97 Version," *Lawrence Natl. Lab.*, vol. 6, 1997.

[77] M. Inokuti and M. R. C. McDowell, "Elastic scattering of fast electrons by atoms. I. Helium to neon," *J. Phys. B At. Mol. Phys.*, vol. 7, no. 17, p. 2382, 1974.

[78] M. Inokuti, "Inelastic collisions of fast charged particles with atoms and molecules-The bethe theory revisited," *Rev. Mod. Phys.*, vol. 43, no. 3, pp. 297–347, Jul. 1971.

[79] H. Tanaka, M. J. Brunger, L. Campbell, H. Kato, M. Hoshino, and A. R. P. Rau, "Scaled plane-wave Born cross sections for atoms and molecules," *Rev. Mod. Phys.*, vol. 88, no. 2, p. 025004, May 2016.

[80] D. Commerce, U.S. Department of Washington, "NIST Chemistry WebBook," *NIST Chemistry WebBook*, 2017. [Online]. Available: https://webbook.nist.gov/chemistry.

[81] S. L. Lunt, D. Field, J. P. Ziesel, N. C. Jones, and R. J. Gulleyel, "Very low energy electron scattering in nitromethane, nitroethane, and nitrobenzene," *Int. J. Mass Spectrom.*, vol. 205, no. 1–3, pp. 197–208, Feb. 2001.

[82] N. C. Jones, "private communication."

[83] D. Field, S. L. Lunt, and J. P. Ziesel, "The quantum world of cold electron collisions," *Acc. Chem. Res.*, vol. 34, no. 4, pp. 291–298, 2001.

[84] S. Nagakura, M. Kojima, and Y. Maruyama, "Electronic spectra and electronic structures of nitrobenzene and nitromesitylene," *J. Mol. Spectrosc.*, vol. 13, no. 1–4, pp. 174–192, 1964.

[85] H. K. Sinha and K. Yates, "Ground-and excited-state dipole moments of some nitroaromatics: Evidence for extensive charge transfer in twisted nitrobenzene systems," *J. Chem. Phys.*, vol. 93, no. 10, pp. 7085–7093, 1990.

[86] T. E. Peacock, "No T," *Proc. Phys. Soc., London*, vol. 78, no. 460, 1961.

[87] O. Matsuoka and Y. I'Haya, "The electronic structure and spectrum of nitrobenzene," *Mol. Phys.*, vol. 8, no. 5, pp. 455–465, 1964.

[88] C. Sieiro and J. I. Fernández-Alonso, "Theoretical interpretation of the electronic spectra of nitrobenzene and benzoic acid," *Chem. Phys. Lett.*, vol. 18, no. 4, pp. 557–560, Feb. 1973.

[89] J. W. Rabalais, "Photoelectron spectroscopic investigation of the electronic structure of nitromethane and nitrobenzene," *J. Chem. Phys.*, vol. 57, no. 2, pp. 967–972, 1972.

[90] F. Zuccarello, S. Millefiori, and G. Buemi, "Electronic spectra of nitrobenzene derivatives," *Spectrochim. Acta Part A Mol. Spectrosc.*, vol. 35, no. 3, pp. 223–227, 1979.

[91] J. D. Steill and J. Oomens, "Spectroscopically resolved competition between dissociation and detachment from nitrobenzene radical anion," *Int. J. Mass Spectrom.*, vol. 308, no. 2–3, pp. 239–252, Dec. 2011.

[92] A. P. Hitchcock, “Inner shell excitation spectroscopy of molecules using inelastic electron scattering,” *J. Electron Spectros. Relat. Phenomena*, vol. 112, no. 1–3, pp. 9–29, 2000.

[93] C. C. Turci, S. G. Urquhart, and A. P. Hitchcock, “Inner-shell excitation spectroscopy of aniline, nitrobenzene, and nitroanilines,” *Can. J. Chem.*, vol. 74, no. 6, pp. 851–869, 1996.

[94] D. Mathur and J. B. Hasted, “Resonant scattering of slow electrons from benzene and substituted benzene molecules,” *J. Phys. B At. Mol. Phys.*, vol. 9, no. 3, p. L31, 1976.

[95] S. Krishnakumar, A. K. Das, P. J. Singh, A. Shastri, and B. N. Rajasekhar, “Experimental and computational studies on the electronic excited states of nitrobenzene,” *J. Quant. Spectrosc. Radiat. Transf.*, vol. 184, pp. 89–99, Nov. 2016.

[96] R. S. Mock and E. P. Grimsrud, “Gas-Phase Electron Photodetachment Spectroscopy of the Molecular Anions of Nitroaromatic Hydrocarbons at Atmospheric Pressure,” *J. Am. Chem. Soc.*, vol. 111, no. 8, pp. 2861–2870, 1989.

[97] S. Katsumata, H. Shiromaru, K. Mitani, S. Iwata, and K. Kimura, “Photoelectron angular distribution and assignments of photoelectron spectra of nitrogen dioxide, nitromethane and nitrobenzene,” *Chem. Phys.*, vol. 69, no. 3, pp. 423–431, Aug. 1982.

[98] L. S. Maioli and M. H. F. Bettega, “Elastic electron scattering from nitrobenzene,” *J. Chem. Phys.*, vol. 147, no. 16, p. 164305, Oct. 2017.

[99] A. I. Lozano *et al.*, “Low energy electron transport in furfural,” *Eur. Phys. J. D*, vol. 71, no. 9, 2017.

[100] A. I. Lozano, F. F. da Silva, F. Blanco, P. Limão-Vieira, and G. García, “Total electron scattering cross section from sevoflurane by 1–300 eV energy electron impact,” *Chem. Phys. Lett.*, vol. 706, pp. 533–537, Aug. 2018.

[101] A. I. Lozano, A. Loupas, F. Blanco, J. D. Gorfinkiel, and G. García, “Total electron scattering cross sections from thiophene for the (1-300 eV) impact energy range,” *J. Chem. Phys.*, vol. 149, no. 13, p. 134303, Oct. 2018.

[102] W. A. D. Pires *et al.*, “Electron impact ionization of 1-propanol,” *Int. J. Mass Spectrom.*, vol. 422, pp. 32–41, Nov. 2017.

[103] S. Ghosh *et al.*, “Electron impact ionization of 1-butanol: II. Total ionization cross sections and appearance energies,” *Int. J. Mass Spectrom.*, vol. 430, pp. 44–51, Jul. 2018.

[104] A. G. Sanz, M. C. Fuss, F. Blanco, F. Sebastianelli, F. A. Gianturco, and G. García, “Electron scattering cross sections from HCN over a broad energy range (0.1-10 000 eV): Influence of the permanent dipole moment on the scattering process,” *J. Chem. Phys.*, vol. 137, no. 12, Sep. 2012.

[105] M. J. Brunger, S. J. Buckman, and K. Ratnavelu, “Positron scattering from molecules: An experimental cross section compilation for positron transport studies and benchmarking theory,” *J. Phys. Chem. Ref. Data*, vol. 46, no. 2, Jun. 2017.

[106] L. S. Maioli and M. H. F. Bettega, “Elastic electron scattering from nitrobenzene,” *J. Chem. Phys.*, vol. 147, no. 16, Oct. 2017.

[107] K. R. Lykke, R. D. Mead, and W. C. Lineberger, “Observation of Dipole-Bound States of Negative Ions,” *Phys. Rev. Lett.*, vol. 52, no. 25, pp. 2221–2224, 1984.

[108] C. L. Adams, H. Schneider, K. M. Ervin, and J. M. Weber, “Low-energy photoelectron imaging spectroscopy of nitromethane anions: Electron affinity, vibrational features, anisotropies, and the dipole-bound state,” *J. Chem. Phys.*, vol. 130, no. 7, 2009.

[109] S. Gulania, T. C. Jagau, A. Sanov, and A. I. Krylov, “The quest to uncover the nature of benzonitrile anion,” *Phys. Chem. Chem. Phys.*, vol. 22, no. 9, pp. 5002–5010, Mar. 2020.

[110] J. N. Bull, C. S. Anstöter, and J. R. R. Verlet, “Ultrafast valence to non-valence excited state dynamics in a common anionic chromophore,” *Nat. Commun.*, vol. 10, no. 1, Dec. 2019.

[111] M. E. Castellani, C. S. Anstöter, and J. R. R. Verlet, “On the stability of a dipole-bound state in the presence of a molecule,” *Phys. Chem. Chem. Phys.*, vol. 21, no. 44, pp. 24286–24290, Nov. 2019.

[112] C. S. Anstöter *et al.*, “Mode-Specific Vibrational Autodetachment following Excitation of Electronic Resonances by Electrons and Photons,” *Phys. Rev. Lett.*, vol. 124, no. 20, May 2020.

[113] C. Szmytkowski, S. Stefanowska, N. Tańska, B. Żywicka, E. Ptasińska-Denga, and P. Możejko, “Cross sections for electron collision with pyridine [C5H5N] molecule,” *Mol. Phys.*,

vol. 117, no. 4, pp. 395–403, Feb. 2019.

[114] "Computational Chemistry Comparison and Benchmark DataBase." [Online]. Available: https://cccbdb.nist.gov/pollistx.asp.

[115] A. I. Lozano *et al.*, "Magnetically confined electron beam system for high resolution electron transmission-beam experiments," *Rev. Sci. Instrum.*, vol. 89, no. 6, p. 063105, Jun. 2018.

[116] F. Blanco *et al.*, "Modelling low energy electron and positron tracks in biologically relevant media," *Eur. Phys. J. D*, vol. 67, no. 9, pp. 1–18, 2013.

[117] U.S. Department of Commerce, "NIST Chemistry WebBook," *Washington, DC*, 2017. [Online]. Available: https://webbook.nist.gov/chemistry/.

[118] X. Ren *et al.*, "Electron-impact ionization of helium: A comprehensive experiment benchmarks theory," *Phys. Rev. A - At. Mol. Opt. Phys.*, vol. 83, no. 5, pp. 1–6, 2011.

[119] A. S. Barbosa, D. F. Pastega, and M. H. F. Bettega, "Shape resonances in the elastic scattering of slow electrons by pyridine," *Phys. Rev. A - At. Mol. Opt. Phys.*, vol. 88, no. 2, pp. 1–6, 2013.

[120] Z. Mašín, J. Benda, J. D. Gorfinkiel, A. G. Harvey, and J. Tennyson, "UKRmol+: A suite for modelling electronic processes in molecules interacting with electrons, positrons and photons using the R-matrix method," *Comput. Phys. Commun.*, vol. 249, Apr. 2020.

[121] C. Q. Jiao, C. A. DeJoseph, R. Lee, and A. Garscadden, "Kinetics of electron impact ionization and ion-molecule reactions of pyridine," *Int. J. Mass Spectrom.*, vol. 257, no. 1–3, pp. 34–40, 2006.

[122] J. N. Bull, J. W. L. Lee, and C. Vallance, "Absolute electron total ionization cross-sections: Molecular analogues of DNA and RNA nucleobase and sugar constituents," *Phys. Chem. Chem. Phys.*, vol. 16, no. 22, pp. 10743–10752, 2014.

[123] T. Yamamoto, M. Miyake, and M. Miura-Mattausch, "Compact modeling of floating-base effect in injection-enhanced insulated-gate bipolar transistor based on potential modification by accumulated charge," *Jpn. J. Appl. Phys.*, vol. 52, no. 4 PART 2, 2013.

[124] F. Blanco, F. F. da Silva, P. Limão-Vieira, and G. García, "Electron scattering cross section data for tungsten and beryllium atoms from 0.1 to 5000 eV," *Plasma Sources Sci. Technol.*, vol. 26, no. 8, p. 085004, Jul. 2017.

[125] M. J. Brunger, "Electron scattering and transport in biofuels, biomolecules and biomass fragments," *Int. Rev. Phys. Chem.*, vol. 36, no. 2, pp. 333–376, Apr. 2017.

[126] G. García, M. Roteta, and F. Manero, "Electron scattering by N2 and CO at intermediate energies: 1-10 keV," *Chem. Phys. Lett.*, vol. 264, no. 6, pp. 589–595, Jan. 1997.

[127] D. B. Jones *et al.*, "Elastic scattering and vibrational excitation for electron impact on para - benzoquinone," *J. Chem. Phys.*, vol. 147, no. 24, 2017.

[128] L. S. Maioli *et al.*, "Theoretical and experimental cross sections for electron scattering from halothane," *Eur. Phys. J. D*, vol. 73, no. 8, 2019.

[129] N. Gholami, M. Hajivaliei, and M. E. Samei, "Calculation of electron scattering cross sections for Anthracene, Pyridine and Warfarin molecules over energy range 10–30000 eV," *Appl. Radiat. Isot.*, vol. 150, pp. 79–86, 2019.

[130] B. Boudaïffa *et al.*, "Resonant Formation of DNA Strand Breaks by Low-Energy," *Scinece*, vol. 287, no. 5458, pp. 1658–1660, 2000.

[131] V. Lemelin and L. Sanche, "High-Resolution Electron Energy Loss Spectroscopy: Absolute Cross Section Measurements for Low Energy Electron Scattering from Biomolecules," Springer, Cham, 2019, pp. 3–42.

[132] F. Blanco, A. Muñoz, D. Almeida, F. F. Da Silva, P. Limão-Vieira, and G. García, "Clustering and condensation effects in the electron scattering cross sections from water molecules," *Int. J. Mass Spectrom.*, vol. 365–366, pp. 287–294, May 2014.

[133] L. Ellis-Gibbings, A. D. Bass, P. Cloutier, G. García, and L. Sanche, "Electron stimulated desorption from condensed pyrimidine and pyridazine," *Phys. Chem. Chem. Phys.*, vol. 19, no. 20, pp. 13038–13048, May 2017.